LUND UNIVERSITY

Integrated optical read-out for polymeric cantilever-based sensors

Tenje, Maria

2007

Link to publication

Citation for published version (APA):
Tenje, M. (2007). *Integrated optical read-out for polymeric cantilever-based sensors*. MIC - Department of Micro and Nanotechnology, Technical University of Denmark.

Total number of authors:
1

General rights
Unless other specific re-use rights are stated the following general rights apply:
Copyright and moral rights for the publications made accessible in the public portal are retained by the authors and/or other copyright owners and it is a condition of accessing publications that users recognise and abide by the legal requirements associated with these rights.
• Users may download and print one copy of any publication from the public portal for the purpose of private study or research.
• You may not further distribute the material or use it for any profit-making activity or commercial gain
• You may freely distribute the URL identifying the publication in the public portal

Read more about Creative commons licenses: https://creativecommons.org/licenses/

Take down policy
If you believe that this document breaches copyright please contact us providing details, and we will remove access to the work immediately and investigate your claim.

LUND UNIVERSITY

PO Box 117
221 00 Lund
+46 46-222 00 00

Integrated optical read-out for polymeric cantilever-based sensors

Maria Nordström
PhD Thesis

February 14th 2007

MIC - Department of Micro and Nanotechnology
Technical University of Denmark
Building 345 east
2800 Kgs. Lyngby
DENMARK

Thesis Defence

May 16th 2007; 13:00
Building 341, auditorium 23
Technical University of Denmark

Evaluation Committee

Prof. Jörg Kutter (Chair)
MIC - Department of Micro and Nanotechnology
Technical University of Denmark, Denmark

Prof. Gregory P. Nordin
Electrical & Computer Engineering Department
Brigham Young University, USA

Dr.Ing. Jesús Ruano-López
Microsystems Area
IKERLAN, Spain

Abstract

This thesis presents a novel read-out method developed for cantilever-based sensors. Cantilevers are thin beams clamped at one end and during the last 10 years they have emerged as an interesting new type of bio/chemical sensor. The specific recognition of a chemical manifests itself as a bending of the cantilever from the generated surface stress. Conventionally the read-out used for this type of sensors is external and thereby very bulky. It is beneficial to fabricate a miniaturised system. Moreover, improved sensitivity is obtained by fabricating the cantilever in a polymeric material that has a low Young's modulus instead of the conventional materials Si and Si_3N_4.

Here, a novel read-out method is presented where optical waveguides are used to integrate the light into the cantilever. It is an all-polymer device where both the cantilever and the waveguides are fabricated in the negative resist SU-8. Waveguides are structured on either side of the cantilever that is free-hanging in a microfluidic channel. Light is guided into the system and is either *transmitted through* the cantilever or *reflected off* the cantilever front-end, depending on the mode of operation. This work shows that waveguides, only supporting the fundamental mode at 1 310 nm and with a propagation loss of only 1.2 dB/cm can be fabricated and integrated with free-hanging cantilevers. A theoretical model is developed to analyse the read-out sensitivity of the two different read-out modes. From calibration experiments the minimum detectable cantilever deflection in the transmission mode is measured as 45 nm, which compares well with the calculated value of 30 nm. Proof-of-principle is shown for the reflection mode as well but no conclusive value can be determined for the read-out sensitivity.

It is believed both these novel principles present interesting alternatives for integrated read-out for cantilever based sensors to enable to fabrication of point-of-care analysis systems.

Dansk Resumé

Denne afhandling præsenterer en ny udlæsnings metode udviklet til cantilever-baserede sensorer. Cantilevere er tynde vipper, der er fastgjorte i den ene ende, og som igennem de seneste ti år har vist sig at være en interessant ny type bio/kemisk sensor. Den specifikke genkendelse af et kemikalie viser sig ved at cantileveren bøjer som følge af det skabte overfladestress. Traditionelt bliver denne krumning kontrolleret af den eksterne optiske udlæsnings metode kendt fra atomic force mikroskopet (AFM). Et sådant set-up er dog meget stort. Det er derfor gavnligt at fremstille et formindsket system. Desuden opnås forøget følsomhed ved at fremstille cantileveren af et plastiskt materiale med et lavt Youngs modulus i stedet for af de traditionelle materialer Si og Si_3N_4.

En ny udlæsning metode præsenteres her, hvor optiske bølgeledere bruges til at integrere lys i cantileveren. Det er et af plast fremstillet apparat, hvor både cantilevere og bølgeledere er fremstillet i det negative resist SU-8. Bølgeledere er strukturer på begge sider af en cantilever, der hænger frit i en mikrofluid kanal. Lys ledes ind i systemet og bliver enten overført gennem cantileveren eller kastet tilbage fra frontdelen af cantileveren, afhængig af fremgangsmåden. Denne afhandling viser at bølgeledere som kun understøtter den fundamentale mode ved 1 310 nm og med et udbredelsestab på kun 1.2 dB/cm kan fremstilles og integreres med frit-hængende cantilevere. En teoretisk model er blevet udviklet til at analysere følsomheden ved de to forskellige udlæsningsmetoder. Baseret på kalibrerings-eksperimenter bliver det mindst sporbare cantilever-udslag i transmissions-måden målt til 45 nm, hvilket passer fint med den beregnede værdi på 30 nm. Proof-of-principle vises også for refleksionsmetoden men ingen endegyldig værdi kan bestemmes for udlæsningsfølsomheden.

Preface

This thesis is written as a partial fulfillment of the requirements to obtain the PhD degree at the Technical University of Denmark (DTU). The PhD project was carried out at the Department of Micro and Nanotechnology (MIC) at DTU in the period from the 15th of February 2004 to the 14th of February 2007.

The PhD project was financed by a DTU PhD stipend and it was part of the Nanoprobes group in the Nanoscience Engineering division at MIC. The supervisors for the project were:

Professor Anja Boisen, MIC DTU
Main supervisor

Associate Professor Jörg Hübner, MIC DTU
Co-supervisor

Dr. Montserrat Calleja, IMM-CSIC, Madrid (Spain)
Co-supervisor

My first thank you goes to the Nanoprobe group that I have been a member of during my PhD time. Here, the atmosphere is always positive and supportive and even though I have many times felt very alone with my project, there has always been someone interested in listening to the latest progress with the waveguides - thank you!

Especially, I thank Alicia Johansson for her friendship and for always having time to discuss matters with me, both of academic and personal character. I would not look back on my PhD time with a smile would it not have been for you and I sincerely hope we will remain as close friends in the future. Secondly, I thank Daniel Haefliger; both for being a fantastic office mate during the months before we qualified for the Nanoprobes floor and for the very interesting discussions we have had on research in general and especially on the commercial aspects necessary. But most I thank you for what you have taught me on project management, presentation skills and leadership - I think mostly without even knowing. I hope we will have

the chance to work together again in the future - be it within research or business. During the last year I have also had the chance to get to know Gabriela Blagoi and I thank you for greatly supporting me during the last months of my PhD. I am very excited we will now start a closer collaboration in our next project. Finally from the group I would like to specifically thank Søren Dohn for programming LabView for me so I finally could get some measurements done - thanks a lot!

Since I joined MIC the group has almost doubled in size and the changes in group dynamics has added vitality to the working environment. Most of all it is impressive to see that the atmosphere can remain grounded on support and trust even under such drastically changing conditions. For this I thank our fantastic group leader Anja Boisen. It is impressive to see how you always manage to make time and room for every single person and always keep the group close to you despite all your other engagements. Moreover, I thank you for being an excellent supervisor, always supporting my ideas and initiatives and being readily available for help when this was needed. I feel very privileged to continue working with you.

I would like to thank my co-supervisor Jörg Hübner for providing a challenging leadership which has taught me to be well-prepared for meetings and thorough in my data analyses. In fact, I would like to thank the whole InSERS group who have always supported me like a real group member. Especially, I thank Dan Zauner for all the help with the optical simulations, preparing the experimental set-up and discussing results. It was a true loss to my project to see you go to Ignis.

I would also like to thank my second co-supervisor Montserrat Calleja at IMM-CSIC in Madrid, Spain. Even though we never got the chance to do any experimental work together I am grateful for the support I have obtained, especially with writing assignments such as different articles and reports. I wish you all the best for the future and maybe we will get to work together again?

I thank all the people at MIC for the good working environment. Especially, I thank Peter Rasmussen for the administrative support and especially help with the "Selvangivelse" without whom I would have had a huge tax debt by now. Naturally, I also send acknowledgement to the staff at Danchip and especially Conny Hougaard and Helle Vendelbom Jensen for helping with SU-8 processing and sawing of wafers, usually on a very short notice. You two are stars!

I would also like to thank the students who have helped my project forward by doing some excellent work; Encarnación Sánchez-Noguerón investigating the bond strength between SU-8 and Au. Christian Kallesøe, Thomas Pedersen and Christian Møller Pedersen for laying the initial grounds to the theoretical work on the read-out sensitivity. Andreas Højsgaard Olsen and Jin Ulrik Louw Andersen who persistently measured on the SU-8 waveguides. Naveen Vemula and Xiaoyong Yang who tried the novel structuring technique of SU-8 which resulted in some excellent results and quiet a few good laughs in the cleanroom and Katrin Sidler for doing a really good MSc project on a very tight time schedule. I hope you all did learn something and that you will remember me.

During my PhD time I also took the opportunity to participate in Venture Cup 2005/2006 and I would like to thank my team members in PolyCan; Julie Heyde, Simon Enghoff and Christian Carstensen Hindrichsen for that rewarding experience. We all put a lot of work into the project and it was a very exciting time for me. However, without our coaches: Carsten Schou at SeeD Capital Denmark, John Heebøll at Væksthus+ and Michael Christiansen at Qvist Executive Search I doubt we would have grabbed that 3rd place - Thank you!

Finally, I thank my parents, Britt-Mari and Bengt Nordström for raising me to be the person I am. My mother for giving me inner peace and confidence in my abilities and my father for making me love challenges and changes. Maybe you should also have taught me that patience is bliss and that sometimes even I can be wrong - but I don't mind living in ignorance...

Lastly, I thank God for giving me a positive mind, endless belief in my ideas and a stubborn soul. However, most of all I thank Niklas for all the love you give without which I could never have come through this.

Maria Nordström
February 14th 2007
Kgs. Lyngby

Contents

1 Introduction **1**

1.1 Sensors and biosensing 1
1.2 Cantilever based biosensors 2
1.3 Novelty and aim of this project 6
1.4 Outline of thesis 8

2 System design **9**

2.1 Design considerations 9
2.2 Basic waveguide theory 10
2.3 Read-out requirements 14
2.4 Basic cantilever theory 16
2.5 Design 17
2.5.1 Material choice 17
2.5.2 Fabrication method 17
2.5.3 Waveguide and cantilever dimensions 18
2.6 Summary 24

3 Materials **27**

3.1 ORMOCERs 27
3.2 SU-8 29
3.2.1 Processing 30
3.2.2 Refractive index variations 31
3.2.3 Stress-optical co-efficient 38
3.2.4 Spectral absorption 40
3.2.5 Birefringence 41
3.3 Summary 42

4 System fabrication **43**

4.1 Negative resists and free-hanging structures 43
4.2 Novel fabrication method 45
4.3 Further process investigations 52
4.4 Release layer investigation 54
4.5 Summary 57

5 Read-out theory **59**
5.1 Overlap integrals 59
5.2 System layout 60
5.3 Reflection mode 62
5.4 Transmission mode 63
5.5 Theoretical output 63
5.6 Summary 69

6 Waveguide characterisation **71**
6.1 Set-up 71
6.2 Propagation loss 72
6.3 Mode profiles 76
6.4 Summary 81

7 Cantilever characterisation **83**
7.1 Cantilever fabrication 83
7.2 Resonance frequency and spring constant 84
7.3 Cantilever sensitivity 85
7.4 Summary 87

8 System characterisation **89**
8.1 Set-up 89
8.2 Light propagation 92
8.3 Transmission mode 94
8.4 Reflection mode 96
8.5 Comparison with theoretical calculations 98
8.6 Summary 102

9 Concluding Remarks **103**
9.1 Alternative read-out method 103
9.2 Conclusions 104

Bibliography **107**

A Facet inclinations **119**

B System processing **123**

C Gaussian mode profiles **127**

D Coupling efficiencies **129**

E Cantilever processing **135**

F List of publications **137**

List of Figures

1.1 Different types of sensors in the human body 1
1.2 Operation principle of cantilevers for static mode detection . 3
1.3 External and integrated optical read-out systems 5
1.4 The integration of a waveguide into the cantilever 6
1.5 Novel read-out method for cantilever based sensors 7

2.1 Different waveguide types used in this work 11
2.2 Gaussian distribution 13
2.3 Schematic drawing of importance of single-mode 14
2.4 Schematic drawing of importance of mode position 15
2.5 Waveguide dimensions for single-mode propagation 18
2.6 V-parameter, cantilever deflection and beam divergence . . . 19
2.7 SEM images of systems with different cantilever dimensions . 20
2.8 Microscope image of the chip layout 21
2.9 Microscope image of a 1st generation chip 22
2.10 Propagation loss of s-bends 23
2.11 Microscope image of a 2nd generation chip 23
2.12 Schematic drawing of reflected light 24

3.1 Refractive index of Ormocore and Ormoclad 28
3.2 Bubbles formed in the Ormocore 29
3.3 Schematic process of SU-8 30
3.4 Refractive index of SU-8 and mr-L from process conditions . 32
3.5 Refractive index variation after hard bake 33
3.6 Refractive index variation after UV exposure 34
3.7 Correlation between refractive index and stress in SU-8 . . . 36
3.8 Relation between processing temperature and refractive index 37
3.9 Stress optical co-efficient of the waveguide materials 39
3.10 Chemical structure of the SU-8 monomer 40
3.11 Spectral absorption of SU-8 41

4.1 Schematic drawing of possible and not possible structures . . 43
4.2 Microscope image of cantilever and waveguides 45
4.3 Schematic drawing of system fabrication 47

4.4 Log from bonding process 48
4.5 Microscope images of non-aligned and aligned structures . . . 49
4.6 SEM images of cantilever and waveguide lens 50
4.7 Insufficient and sufficient bonding layers 50
4.8 SEM image of final bonded chip 51
4.9 Alternative process sequences 52
4.10 Comparison between exposure modes 54
4.11 Remains of SU-8 or fluorocarbon after chip release 55
4.12 AFM topography scan from SU-8 side of cantilever 55
4.13 AFM topography scan from fluorocarbon side of cantilever . . 56

5.1 Schematic drawing of the principle of overlap integrals 59
5.2 Schematic drawing of the different regions of the system. . . . 60
5.3 Normalised horizontal wavefunctions of the different regions . 61
5.4 Normalised vertical wavefunctions of the different regions . . 62
5.5 Comparison between α_{trans} and α_{ref} 64
5.6 Comparison between P_{out} in air and water 66
5.7 Comparison between P_{out} in the two modes 68
5.8 Theoretical calculation on the read-out sensitivities 69

6.1 Set-up used for the optical characterisation 72
6.2 Cut-back results at 635 nm and 1 535 nm 73
6.3 Propagation loss of SU-8 in the spectral range 800 - 1 700 nm 74
6.4 Coupling loss of SU-8 in the spectral range 800 - 1 700 nm . . 75
6.5 SEM image comparing a cleaved and sawn facet 76
6.6 Coupling loss from a cleaved and sawn facet 77
6.7 Mode profile of 10 µm embedded SU-8 waveguide 78
6.8 Mode profile of 5 µm embedded SU-8 waveguide 78
6.9 Simulation output of asymmetric waveguide 79
6.10 Mode size for embedded waveguides 80
6.11 Mode profile of 10 µm rib SU-8 waveguide 81

7.1 SEM images of released cantilever chips 83
7.2 SEM images of released cantilever chips 84
7.3 Resonance frequency of the cantilevers in air and liquid . . . 85
7.4 Comparison between SU-8 and Si_3N_4 cantilever 86

8.1 Schematic image of the set-up for the calibration of the system 89
8.2 Picture of set-up used for calibration 90
8.3 Position on chip for mode profiles 92
8.4 CCD images of light exiting input and output waveguides . . 92
8.5 Mode profiles of input and output waveguides 93
8.6 Transmission mode read-out measurement 94
8.7 Calibration curve for transmission mode read-out 95
8.8 Reflection mode read-out measurement 96

8.9 Schematic of the probe position along the cantilever 97
8.10 Effects of probe position in reflection mode read-out 98
8.11 Expected optical output for P_{in} of 20 μW 99
8.12 Extra loss sources in the transmission mode 100
8.13 Comparison between theoretical and experimental results . . 101

9.1 Schematic drawing of the 'Step-and-Flash' method 103
9.2 SEM images of Si stamp and resulting SU-8 structures. . . . 104

A.1 Light paths for the situation of inclined interfaces 120

D.1 Schematic drawing of the light path in the reflection mode . . 129
D.2 Schematic drawing of the light path in the transmission mode 132

Chapter 1

Introduction

1.1 Sensors and biosensing

A sensor is a device that detects the presence of a specific stimuli and translates it into a measurable output signal [1]. Chemical sensors respond to such stimuli through a chemical reaction between a capture probe and the analyte [2]. This PhD thesis is focused on *biosensors* that are a subset to chemical sensors with the specificity that the capture probe is of biological nature, such as antibodies or enzymes [3]. Here, the capture probes constitute the sensitive layer on the sensor and the analytes are the biomolecules to be detected. This nomenclature is used throughout the thesis.

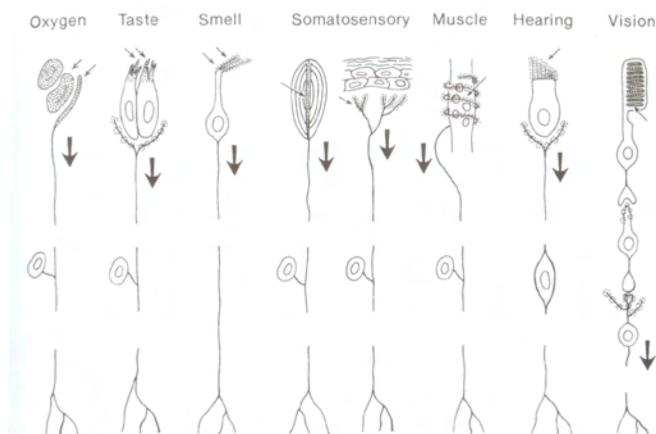

Figure 1.1: Different types of sensors in the human body. The tongue and the nose are biosensors. The presence of an analyte is recorded by the sensitive capture probes and is converted into an measurable output by a transducer [4].

Biosensors are commonly used within medical analysis (e.g. HIV tests) and pharmaceutical research to give two example areas. The traditional and most commonly used biosensor, developed in 1971, is the Enzyme-Linked ImmunoSorbent Assay (ELISA) [5]. Here, the fluorescently labelled analyte is captured by the probe layer and its presence is read-out optically by observing the density of the fluorescent probes. This is proven a very efficient biosensor but it is a rather time consuming and complex process including many steps. Another disadvantage is the necessary labelling of the analyte. The labelling increases the costs considerably both with respect to reagents needed and work time. Furthermore, labelling of molecules is extremely difficult and it often modifies the properties of the molecule in question, which in turn might lead to errors in the final data interpretation. Therefore, label-free biosensors are preferred. With the development of micro technology and the area of micro-electro-mechanical systems (MEMS) and micro-opto-electro-mechanical systems (MOEMS) novel and more efficient types of biosensors have been presented. Today there exist several types of label-free biosensors on the market, such as; Quartz Crystal Microbalance (QCM) (Q-Sense, Sweden) [6], Surface Plasmon Resonance (SPR) (BiaCore, Sweden) [7], Diffractive Optics Technology (DOT) (Axela, Canada) [8] and Resonant Waveguide Grating (RWG) (Corning, USA) [9].

All these biosensors provide a platform for the detection of different analytes, either in gas phase or in liquid phase. However, an ideal biosensor is portable, can perform multiple measurements simultaneously and allows for cost-efficient single use system, which these sensors do not.

1.2 Cantilever based biosensors

Micrometer sized cantilevers were initially developed for the technologies scanning force microscopy (SFM) and atomic force microscopy (AFM), which were invented in the 1980's [10, 11] and are today two of the most important tools within the research area of micro fabrication and nanotechnology. In the 1990's it was realised that such cantilevers can also be used as environmental and chemical sensors [12, 13]. The first application of a microcantilever as a biosensor was presented in 1996 by Baselt *et al.* [14] and the research field has expanded fast since then [15].

To detect molecules the cantilever can be operated either in *dynamic* or *static* mode. In the dynamic mode, the resonance frequency of the cantilever is monitored as the analyte binds to the probe layer [16]. The probe molecules are distributed over the whole cantilever and the decrease in resonance frequency as a result of the added mass from the analyte is read as the output signal.

Chemicals binding onto the cantilever surface not only add a mass but also generate surface stress changes. Due to the large surface-area-to-volume-ratio ($\sim$ 1,000,000) of the cantilever, such surface stress changes affect the cantilever greatly. By carefully ensuring the probe molecules only bind to one of the cantilever surfaces, a *differential* surface stress is generated, which bends the cantilever [17]. This is the principle of operation of the static mode, shown schematically in figure 1.2. This thesis work is completely focused on cantilevers applied in the static mode of detection.

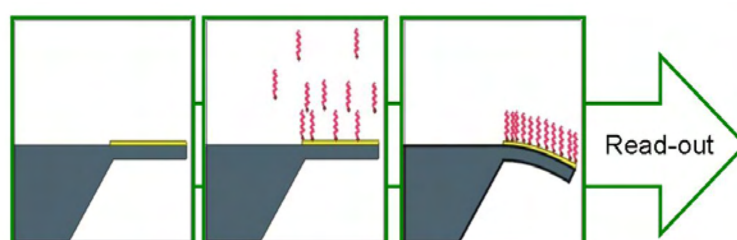

Figure 1.2: Operation principle of cantilevers for static mode detection. As the analyte reacts with the probe molecule on one side of the cantilever a differential surface stress is generated that bends the cantilever. This bending is read as the output signal of the sensor. Image courtesy to Rodolphe Marie.

Since the research area on cantilever-based biosensing was born several applications such as the detection of cancer markers [18, 19], pesticides and heavy metal ions [20, 21] and the discrimination of single base-pair mismatches in DNA [22] have been presented to name but a few. A typical surface stress change generated from the immobilisation of DNA is 4 mN/m [23–25]. The fundamental theory of the interactions resulting in the surface stress has been studied and several propositions have been given [24, 26–29]. It has also been shown that a greater cantilever bending is generated if the probe molecule and analyte are maintained as close to the cantilever surface as possible [30, 31]. The use of a reference cantilever for measurements has also been established as a standard operating procedure to obtain reliable data [32]. The need for this is because the cantilever reacts with most changes in its environment and not only those associated with the chemical bindings. This means that temperature variations, pressure changes and pH alterations also result in a read-out signal generated by the cantilever. By using a reference cantilever subjected to the same conditions but with a coating that is inert to the analyte, the signal caused by the artifacts can be subtracted. The reference cantilever shall be structured on the same chip as the sensing cantilever to ensure that the external conditions are identical.

Structuring many cantilevers in an array on a single chip also opens up for the possibility to perform multiple detections simultaneously and thereby greatly increase throughput.

The most commonly used material to fabricate cantilevers in is Si [33] and Si_3N_4 [34] and cantilevers in these materials are commercially available from a series of vendors [35–37]. However, fabricating the cantilevers in polymeric material opens up for an increase in sensitivity since the softer polymeric material bends more for the same applied surface stress. The Nanoprobes research group has previously shown both the fabrication of simple SU-8 cantilevers and cantilevers with integrated read-out [38–40]. During recent years cantilevers fabricated in other types of polymers have also been presented such as; Polystyrene [41], Polyethylene terephthalate (PET) [42] and epoxies such as UVO-114 [43]. The response of the cantilever is usually read-out by the optical leverage principle known from AFM [44, 45] but different integrated read-out methods have also been developed [46, 47].

The main advantages of cantilever-based detection system are (i) it is a label-free detection process (ii) real-time read-out is given (iii) small amounts of reagents are needed (iv) the small size also allows for miniaturisation, making a portable detection system possible and (v) the cantilevers can easily be structured into an array, allowing for simultaneous multiple detections. However, for the cantilever-based biosensor to reveal its true and full potential as a miniaturised biosensor an integrated and stable read-out is required as this will open up for the possibility to fabricate point-of-care devices. The aim of this PhD project is to fabricate a polymeric cantilever-based biosensor with integrated optical read-out. By structuring the cantilevers in a polymer an increase in sensitivity can be expected. The read-out facilitates the fabrication of a portable device for point-of-care diagnostics as no large external detection equipment is needed. The aim is also to provide a read-out with a possibly higher sensitivity compared to existing integrated read-out schemes. A further advantage of this read-out method is that it might create a more robust system where the read-out scheme is not sensitive to the presence of conductive liquids or the disturbance of external electromagnetic fields. The focus of this PhD work is purely on the technical side of the system; to design, fabricate and characterise a novel integrated read-out method. This means that no bio/chemical measurements are performed with the complete system.

Previous work within the field

The most common read-out method for cantilever sensors, as mentioned above, is the optical lever method know from AFM [44]. Figure 1.3(A) shows an image where this principle is presented. Light from the light source (LS)

is directed towards the cantilever and reflected onto a photo-detector (PD). As seen in the figure all the components of the set-up are placed outside the cantilever sensing system. This means that the set-up is rather large and bulky. Moreover, since the light is reflected off the top-side of the cantilever there might be artifacts in the read-out from the binding of the analyte onto the cantilever because the chemical reaction occurs at the same position as where the light is reflected. Moreover, the alignment procedure of the laser light can be both complex and time-consuming.

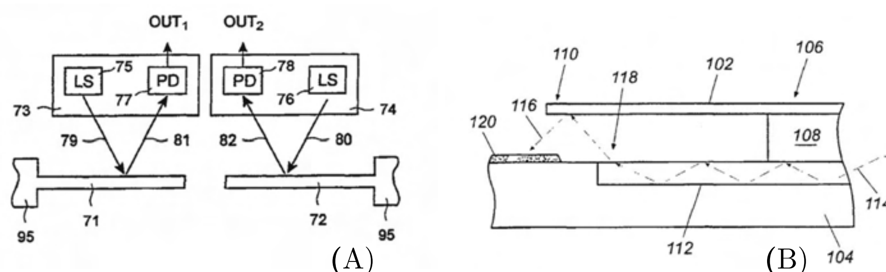

Figure 1.3: Side view of two systems comparing external and integrated optical read-out schemes. (A) Principle of the optical lever detection read-out known from AFM. As the cantilever deflects the position of the reflected laser light at the position-sensitive photo-diode is altered [48]. (B) Here, both the light sources and the photo-detector are brought closer to the cantilever by using integrated optics to make a more compact biosensor [50].

In the Derwent patent database [49] there exists a variety of interesting solutions where integrated optics is applied to reduce the size of the detection set-up. B.M. Evans *et al.* present a system where the cantilever is structured over a waveguide that directs the light towards the cantilever, figure 1.3(B) [50]. The advantage of this system is that the alignment step is greatly simplified. Moreover, the system can be made more compact since the distance of the light path is greatly shortened. However, the light is still reflected off the back-side of the cantilever, which might introduce large levels of noise in the detections caused by the scattering of the probe molecules.

Lucent Technologies Inc. and researches at the University of Huntsville-Alabama have independently solved this problem by not reflecting the light off the cantilever but integrating a waveguide into the cantilever structure [51, 52]. The light exiting the waveguide is detected on the opposite side via coupling into an output waveguide. As the cantilever deflects less light can couple across the gap and the decrease in the throughput intensity is simply translated into a measure of the cantilever deflection. Figure 1.4 shows the working principle of these two systems. In figure 1.4(A) the cantilever waveguide is marked with the number 250 and the input and output waveguides are marked with the number 400. In figure 1.4(B) number 22 is

the input waveguide, number 30 is the cantilever waveguide and number 34 is the output waveguide. Similar systems are also presented in the literature by Zinoviev *et al.* [53] and Xu *et al.* [54].

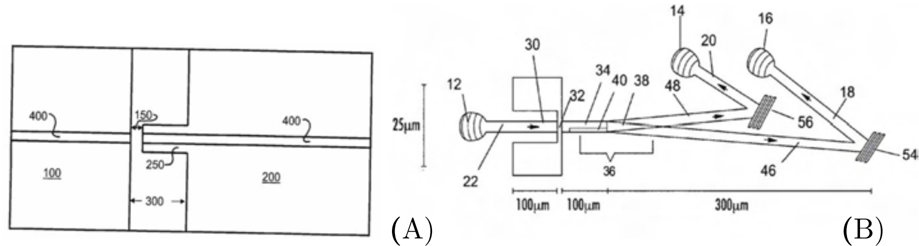

Figure 1.4: Top view of two systems where a waveguide is integrated into the cantilever. Both these systems are operated in transmission mode where light travels through the cantilever. This means that the cantilever waveguides is very sensitive to any variations in the surrounding medium [51, 52].

These systems show an interesting read-out principle but still there are many sources of read-out artifacts present. Since the cantilever itself acts as a waveguide the system becomes very sensitive to changes in the refractive index of the surrounding medium. In a typical bio/chemical measurement the cantilever is flushed in buffer after the probe molecules are bound onto the cantilever to remove any non-specifically bound molecules [55]. The refractive index of this solution will not be identical to the measurement solute, which will change the coupling efficiency across the gap. Moreover, the induced surface stress in the cantilever generated by the analytes binding might affect the refractive index of the waveguide core itself and alter the read-out signal.

1.3 Novelty and aim of this project

The system presented in this PhD thesis comprises a polymeric cantilever with an integrated optical read-out scheme. Two modes of operation are investigated, the *transmission mode* and the *reflection mode*.

The transmission mode read-out is the same as described in figure 1.4 with the exception that the system fabricated here is an all-polymer device. For the reflection mode a waveguide is structured on the opposite side of the micro-channel to the cantilever. This waveguide acts as input waveguide and the exiting light is reflected off the cantilever front-end. As the cantilever deflects due to reaction with the analyte, less light is back-reflected into the input waveguide. The working principle of the system in both modes is shown schematically in figure 1.5.

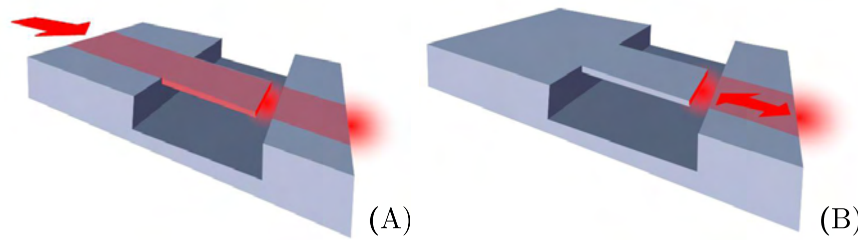

Figure 1.5: Novel read-out method for polymeric cantilever based sensors. (A) The cantilever acts as a waveguide and the intensity of the throughput light is measured in the transmission mode of operation. (B) In the reflection mode light from an integrated waveguide is reflected off the cantilever front-end. As the cantilever deflects, less light is back-reflected into the input waveguide. Images courtesy to Daniel Haefliger.

Both read-out modes are investigated as a comparison to find the best suited detection scheme, both with respect to sensitivity and user-friendliness but also with respect to noise levels and stability of operation. It shall be noted that neither of these integrated read-out modes have been presented before in an all-polymer device. By reflecting the light off the front-end of the cantilever instead of the top surface, disturbance in the read-out signal from structural and chemical changes occurring on the cantilever surface due to the molecular bindings is avoided. This detection method also makes the device more stable since the cantilever is not used as a waveguide but purely as a mechanical structure which the light is reflected off. With respect to miniaturisation both detection modes are equally and highly suited since the use of bulky detection equipment is avoided and only a simple light emitting diode and a photo-diode are required. Moreover, these read-out methods make it possible to place all optical equipment in the packaging of the device. This drastically reduces the costs involved in fabricating a single-use system since the sensing cantilever is the only part that needs to be replaced. Both read-out modes are compatible with an array of cantilevers, which means that a high throughput of analysis samples can be obtained. It is believed that both these integrated read-out methods can offer hand-held devices with a potentially higher sensitivity and more stable read-out than existing hand-held biosensors.

The aim of this project is to show that polymeric cantilevers structured in an array can be fabricated with a novel integrated optical read-out method. To achieve these aims, a new fabrication method is developed to fabricate the free-hanging cantilever structures. Moreover, a theoretical model for the read-out sensitivity is developed and applied to quantify the read-out sensitivity. The cantilevers and waveguides fabricated are characterised indi-

vidually. Lastly, the system is characterised where both read-out modes are monitored as the cantilever is mechanically deflected a known distance. No real-life applications are shown with this system since that is outside the scope of this PhD work but the commercial interest for this type of product was investigated by the participation in the business plan competition Venture Cup 2005/2006.

1.4 Outline of thesis

Chapter 2 discusses the aspects considered for the development of the system. It gives an introduction to the important parameters of both waveguide and cantilever design. The design of the final system is presented.

Chapter 3 presents experimental results from the four different polymers investigated during this PhD project. It shows the effects of process variations on the optical properties of the waveguide materials.

Chapter 4 describes the fabrication process of the complete system and addresses some specific considerations that need to be made.

Chapter 5 shows the theoretical calculations on the sensitivity of the read-out of this system.

Chapter 6 contains the work on the optical characterisation of the waveguide structures in the system. Studies are performed to ensure the waveguides are single-mode and to find the most suitable wavelength of operation of the final system.

Chapter 7 shows work done with the polymeric cantilevers separate from the detection system. This work is performed by Montserrat Calleja in the Nanomechanics laboratory at CNM-CSIC, Madrid, Spain.

Chapter 8 gives details on the mechanical characterisation of the read-out methods. Proof-of-principle is shown for both the reflection and the transmission mode.

Chapter 9 concludes on the work and the achieved results and gives an outlook onto an alternative read-out method.

Appendix A derives the requirement for increasing the signal-to-noise ratio in the reflection mode read-out.

Appendix B gives the fabrication sequence of the system where all process parameters are listed.

Appendix C shows how the mode profile of the waveguides are calculated using the Gaussian approximation.

Appendix D describes the theoretical model and gives details on the calculation of the coupling efficiencies of the two different read-out modes.

Appendix E contains the fabrication sequence for the chips comprising cantilevers alone.

Finally, Appendix F includes a list of publications generated from this PhD project.

Chapter 2

System design

This chapter discusses the design considerations of the system both with respect to the optical waveguides and the cantilevers. To provide a solid understanding of the aspects that are of importance, some basic waveguide and cantilever theory is first presented. This thesis bears no intentions of giving a thorough introduction to the theory of either structure but rather to present the necessary tools for the development and fabrication of this system. In the last two sections the final design of the system is presented with respect to material choice, fabrication method and chip layout.

2.1 Design considerations

The long-term aim of use of the sensor system developed here is point-of-care diagnostics, which means that the sensor should be able to perform bio/chemical analyses outside a laboratory. The work presented here is the first step of the product development and for this project the aim is rather proof-of-principle. However, it is still important to keep the long-term perspective in mind already from the start. Therefore, before deciding on the sensor design and material choices the different requirements imposed need to be considered:

Since the system is intended to be operated outside a laboratory:

- it must be a stable and robust system
- the signal read-out must be straight-forward to interpret
- only small amounts of liquids and reagents should be required
- false-positive and false-negative signals must be kept to a minimum
- no pre-treatments should be necessary before the system can be used

To make it a profitable venture case:

- the processing should be fast and simple
- the full-scale production, including all process steps such as chemical activation and packaging, must be economically profitable
- transportation and storage costs must be kept to a minimum
- all parts of the system should preferably be fabricated with the same technique
- the product must have many applications to attract a large group of possible customers

To ensure that the system delivers the mentioned requirements, the design must be such that:

- the waveguides are single-mode in the vertical direction
- the optical losses in the waveguides are low, not exceeding 3 dB/cm
- the refractive index step is tuned to ensure a good coupling efficiency between the input fiber and the waveguide structures
- the waveguide is in-homogenous, i.e. that there is a small difference in the refractive index between the top and bottom claddings so the mode profile is not perfectly centered in the waveguide
- the material choice ensures high sensitivity of the cantilever, capable to detect surface stress changes in the order of mN/m, which is a typical value for a DNA immobilisation [23–25]
- the optical properties of the materials are known and possible to control

As will be seen at the end of this chapter, most of these requirements are fulfilled but before going into details on the design, a few subsections with general waveguide and cantilever theory are presented for background knowledge.

2.2 Basic waveguide theory

A waveguide is a structure consisting of a guiding material, the *core* and a surrounding material, the *cladding*. The light travels inside the core by *total internal reflection* [56]. Figure 2.1 shows the different waveguide types used in this work.

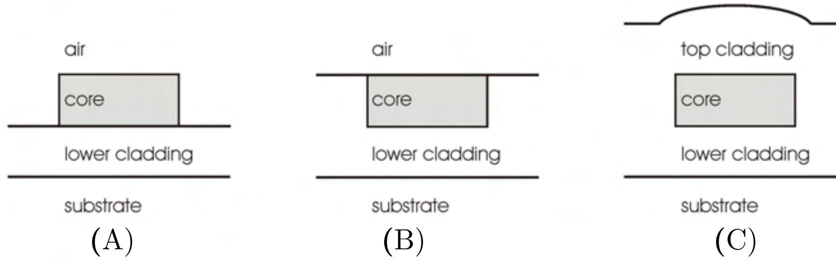

Figure 2.1: The different waveguide types used in this work. (A) Rib waveguide where air acts as cladding on the top and sides of the waveguide core. (B) Channel waveguide with air as top cladding and the lower cladding surrounds the sides of the waveguide core. (C) Embedded waveguide with the same material as top and bottom cladding covering the whole waveguide core. The top cladding of the embedded waveguide will normally show a slight protrusion from the core layer as indicated in (C). The refractive index of the core must be higher than the refractive index of the surrounding cladding for waveguiding to occur.

For waveguiding to occur, the refractive index of the core (n_{co}) must be larger than the refractive index of the cladding (n_{cl}). A large index step ensures a good confinement of the light to the core whereas a smaller step allows for a greater spread of the light into the cladding layer. The light travels in two polarised modes, the **TE** mode (transverse electric) and the **TM** mode (transverse magnetic). Throughout this thesis only the **TE** polarisation is considered because the optical detectors used are not polarisation sensitive. Moreover, only a minor birefringence is expected in these waveguide structures, which is discussed further in Chapter 3.

Number of modes: V-parameter

The number of modes in a waveguide depends on the wavelength of operation, the size of the waveguide and the refractive index step between the two materials. For material combinations with a very small index step ($n_{co} \simeq n_{cl}$) the *weak-guidance approximation* applies [57]. In this regime the normalised frequency, V, is a measure of the number of guided modes. The constrain for single-mode propagation is V $\leq$ 2.136.

$$V = \frac{2\pi}{\lambda_0}\rho(n_{co}^2 - n_{cl}^2)^{1/2} \qquad (2.1)$$

where λ_0 is the free-space wavelength, n_{co} is the refractive index of the core, n_{cl} is the refractive index of the cladding and ρ is the half height or width of the waveguide structure.

From equation (2.1) it can be seen that with a small index step, the dimensions of the waveguide are allowed to be in the order of 10 μm and still the waveguide only supports the fundamental mode at wavelengths in the near-infra red region.

Numerical aperture

The numerical aperture (NA) is a measure of the acceptance angle of the waveguide [58]. The light is butt-coupled into the waveguide from an optical fibre and to obtain a high coupling efficiency, the NA of the fiber and the waveguide should be matched. The NA of the fibres used in this work is 0.13 [59].

$$\text{Numerical Aperture} = (n_{co}^2 - n_{cl}^2)^{1/2} \tag{2.2}$$

where n_{co} is the refractive index of the core and n_{cl} is the refractive index of the cladding material.

Fresnel reflections

When light crosses different material borders, not all the power is transmitted but some is back-reflected due to Fresnel reflections [56]. The expression for rays of perpendicular impact is

$$R_{Fres} = \left(\frac{n_1 - n_2}{n_1 + n_2}\right)^2 \tag{2.3}$$

where n_1 is the refractive index of the material the light exits from and n_2 is the refractive index of the medium the light enters into.

For the situation where the light exits the input waveguide ($n_{co} = 1.5725$ at 1 310 nm) and enters into air ($n_{air} = 1.00$), equation (2.3) shows that approximately 4.5 % of the light is reflected back into the waveguide. If the gap is filled with water instead ($n_{water} = 1.33$), only 0.7 % is reflected back. This phenomenon is highly important both when coupling light in and out of the chip but also when considering the sensitivity of the two read-out modes.

Gaussian approximation

The waveguides developed in this work are aimed for single-mode excitation. The intensity profile of the light can therefore be approximated with a Gaussian wavefunction. Figure 2.2 plots the intensity profile of the fundamental mode. The width of the mode depends on the dimensions of the waveguide and the index step between the core and the cladding materials [57]. Inside

a waveguide the light is confined, which means that the width of the mode is constant. The width of the mode is denoted by the *mode field diameter* (MFD) which is measured as the full width of the intensity profile at an intensity $I = I_0/e^2$.

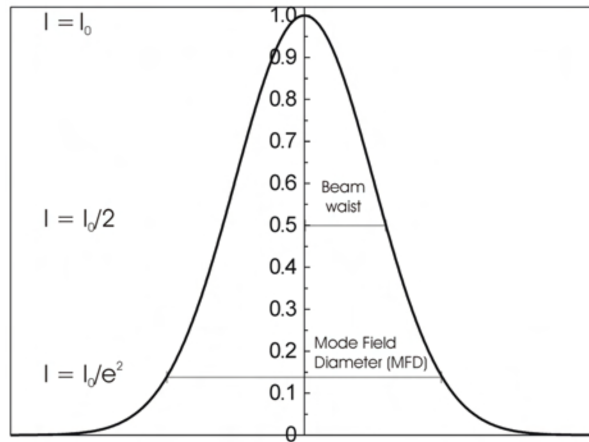

Figure 2.2: The light intensity follows the Gaussian distribution inside the waveguides. The width of the mode is defined by its mode field diameter (MFD) which is marked in the figure. For clarity, the definition of the beam waist which determines the development of the intensity profile when the light exits the waveguide is also marked.

Beam divergence

When the light exits the waveguide its width is no longer constrained and after traveling a distance l its beam waist, $w(l)$, increases as

$$w(l) = w_0 \left[1 + \left(\frac{\lambda_0 l}{\pi w_0^2} \right)^2 \right]^{1/2} \tag{2.4}$$

where w_0 is the beam waist when the light exits the waveguide, λ_0 is the free-space wavelength and l is the distance travelled [58]. w_0 is marked in figure 2.2.

The equation shows that a beam with an initially small beam waist will spread more quickly in a shorter distance travelled than a beam with an initial larger waist. This is an important phenomenon to consider when deciding on the height of the waveguides in the system.

2.3 Read-out requirements

The cantilever bending is determined by monitoring the intensity of the light either reflected off the cantilever (reflection mode) or transmitted through the cantilever (transmission mode). It shall be possible to operate the system simultaneously in both modes to compare the two.

Single-mode

It is crucial that the waveguide is single-mode in the vertical direction for a straight-forward read-out, since it is in this plane the cantilever moves. This is shown schematically in figure 2.3. If the waveguide were multi mode, the intensity profile would show several peaks as the cantilever deflects and it would not be easy to determine the position of the cantilever.

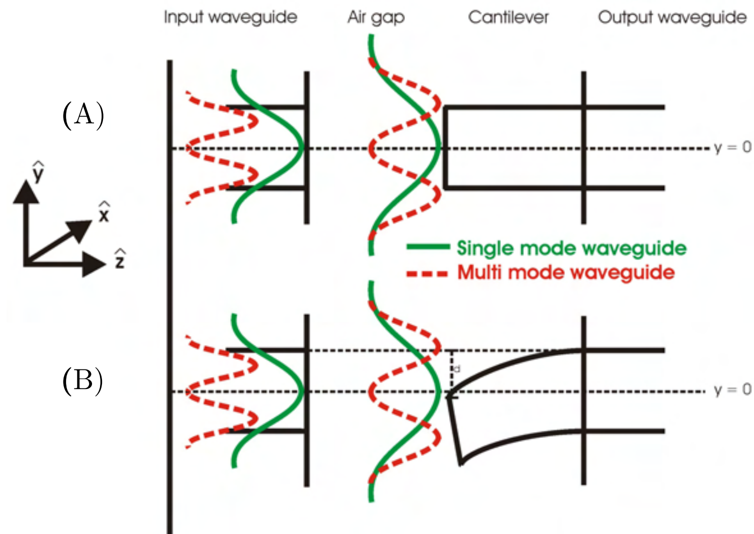

Figure 2.3: Side view of the input waveguide and the cantilever. The waveguide needs to be single-mode in the plane of movement of the cantilever to ensure that the intensity of the output light can be directly related to the bending of the cantilever. Here, a comparison is shown between a single-mode (green solid line) and a multi mode (red broken line) waveguide.

Mode centering

A perfectly centered waveguide mode results in a low sensitivity at small cantilever deflections since the Gaussian profile is almost constant at the center position, as seen in figure 2.2. A waveguide mode that is slightly off-centered shows a higher sensitivity since the cantilever movement is in the

region of the steepest slope of the intensity profile. This is shown schematically in figure 2.4. It is therefore preferential to structure an in-homogeneous waveguide.

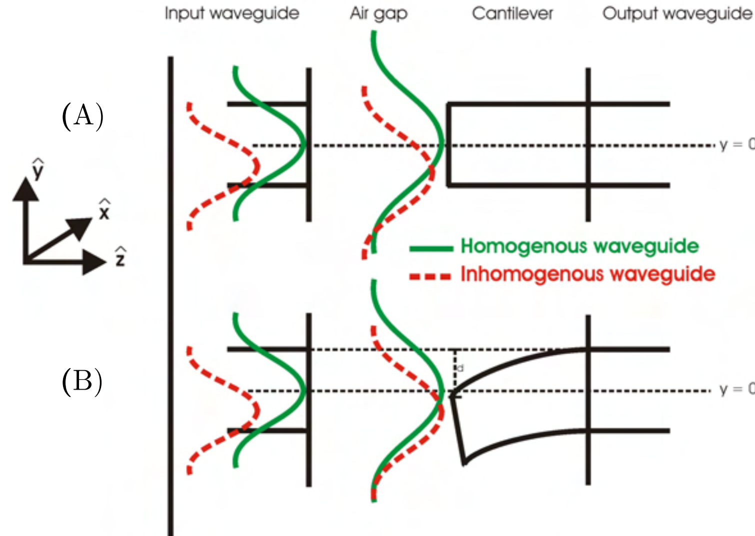

Figure 2.4: Side view of the input waveguide and the cantilever. It is preferable that the mode of the input waveguide is no perfectly centered. Here, a comparison is shown between a perfectly centered mode (green solid line) and a waveguide mode that is slightly off-centered (red broken line).

Waveguide propagation loss

It is important that the waveguide material does not absorb at the wavelength of operation as this will significantly reduce the signal-to-noise ratio. A maximum waveguide propagation loss of 3 dB/cm is acceptable since the length of the waveguide typically is only 1 - 2 cm.

Detection system

The light intensity is detected with a photo-detector. The sensitivity of this detector is limited by the shot noise and the thermal noise caused by the inherent randomness in the photon stream [58]. The noise level of the photodetectors used in this set-up is approximately 5 nW as determined experimentally.

Chip layout

The layout of the chip shall ensure that it is possible to operate the chip both in reflection and transmission mode simultaneously. There must also

be at least two cantilevers so that one can act as measurement cantilever and the other as reference cantilever. Furthermore, there must be a reference light path from where the propagation and coupling losses of the system can be determined and from where it can be confirmed that the light propagates through the system.

2.4 Basic cantilever theory

The cantilevers are operated in static mode where it is the bending generated from molecular bindings on the cantilever that is monitored. However, there are also other effects that will bend the cantilever and cause artifacts in the read-out of the measurement.

Surface stress sensitivity

From Stoney's equation of stresses in thin films, the resulting cantilever deflection, Δd, generated by a differential surface stress is calculated as

$$\Delta d = \frac{3(1-\nu)\ l^2}{Et^2}\Delta\sigma \tag{2.5}$$

where ν and E is the Poisson's ratio and Young's modulus of the cantilever material respectively, l and t is the length and the thickness of the cantilever respectively and $\Delta\sigma$ is the differential surface stress [60].

It is seen that the sensitivity of the cantilever increases with the square of the length and that it is beneficial to use a material with a low Young's modulus. However, increased length and a softer material also mean that the cantilever will have difficulties to support itself, which needs to be compensated for in the design.

Molecular recognition

The upper and lower surfaces of the cantilever need to have different surfaces since no bending will be generated of the cantilever if equal amount of molecules can attach on either side. To selectively bind the analyte onto only one surface of the cantilever, the cantilever can be fabricated in two different materials or the chemical composition of one of the surfaces can be modified.

Temperature dependence

During the operation of the sensor small temperature fluctuations are likely to occur as a result of buffer changes or from changes in the temperature of the surrounding. If the cantilever is fabricated in two different materials,

these temperature fluctuations result in cantilever bendings from the bimorph effect calculated as

$$\Delta d = \frac{3l^2(\alpha_1 - \alpha_2)\Delta T}{t_1 + t_2} \left[\frac{\left(1 + \frac{t_1}{t_2}\right)^2}{3\left(1 + \frac{t_1}{t_2}\right)^2 + \left(1 + \frac{t_1}{t_2}\frac{E_1}{E_2}\right)\left(\frac{t_1^2}{t_2^2} + \frac{t_2}{t_1}\frac{E_2}{E_1}\right)} \right] \quad (2.6)$$

where l is the length of the cantilever, ΔT is the temperature variation, t_1 and t_2 are the thicknesses, α_1 and α_2 are the thermal expansion coefficients and E_1 and E_2 are the Young's modulus of the two materials respectively [61].

From the equation it is seen that it is an advantage to use two materials that have as similar material properties as possible to reduce artificial deflections of the cantilever from temperature fluctuations.

2.5 Design

Considering the requirements listed above on the waveguide properties and cantilever behaviour the following decisions were made on the design of the system and its fabrication process.

2.5.1 Material choice

To ensure a high sensitivity of the cantilever and to obtain a fast and simple processing, the chip is fabricated completely in polymeric materials. The waveguide and cantilever are structured in the same layer in one polymer. The micro fluidic system as well as the chip body, that also makes up the cladding of the waveguides, are structured in a different polymer. It is preferable to make the waveguide as large as possible to make alignment and coupling of light into the waveguide as easy as possible. The index step between the core and the cladding should be accordingly small to ensure the waveguide still only supports the fundamental mode. Figure 2.5 shows the maximum thickness of the waveguide core fabricated in the polymer SU-8 using a variety of possible cladding materials and maintaining the single-mode constrain defined in section 2.2. From these considerations, the polymer mr-L is chosen as the cladding material of the final system. Its material properties are discussed in Chapter 3.

2.5.2 Fabrication method

The fabrication method of the system is UV-lithography since this enables a straight-forward processing with a line resolution down to 1 µm. Alternative

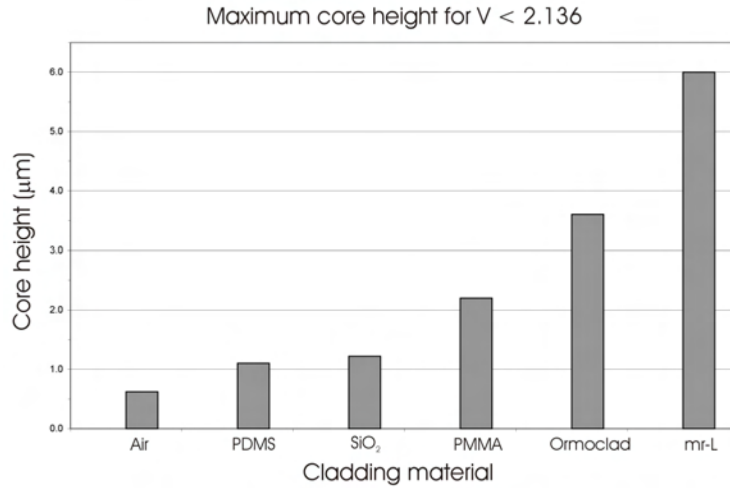

Figure 2.5: The maximum height of the waveguide is calculated from equation (2.1) to ensure single-mode propagation with different cladding materials at 1 310 nm. The waveguide core is fabricated in SU-8.

fabrication methods for polymers are nanoimprint lithography (NIL) [62], hot embossing [63], injection moulding [64] or patterning by other types of radiation such as X-ray or electron-beam [65, 66]. However, for the fabrication of this system none of these methods are appropriate as they are more complicated and costly than UV-lithography and do not provide any crucial advantages. As will be seen in Chapter 9 UV-lithography does have some limitations and to compensate for these the technology of 'Step-and-Flash' is also investigated.

2.5.3 Waveguide and cantilever dimensions

The waveguides and the cantilevers are fabricated from the same layer and will therefore have the same thickness whereas the widths may differ. The thickness of this layer is determined from an interplay of the four important aspects (i) the cantilever shall be as thin as possible for increased sensitivity, equation (2.5) (ii) the cantilever cannot be too thin as it will not be able to support its own weight (iii) the waveguide cannot be too thin since this will not result in a Gaussian intensity profile of the light as it reaches the cantilever, equation (5.2) and (iv) the waveguide shall be as thick as possible for improved coupling efficiency between the fibers but remain single-mode, equation (2.1).

Figure 2.6 shows the V-parameter, cantilever deflection and beam divergence as a function of the half height, ρ, of the input waveguide and can-

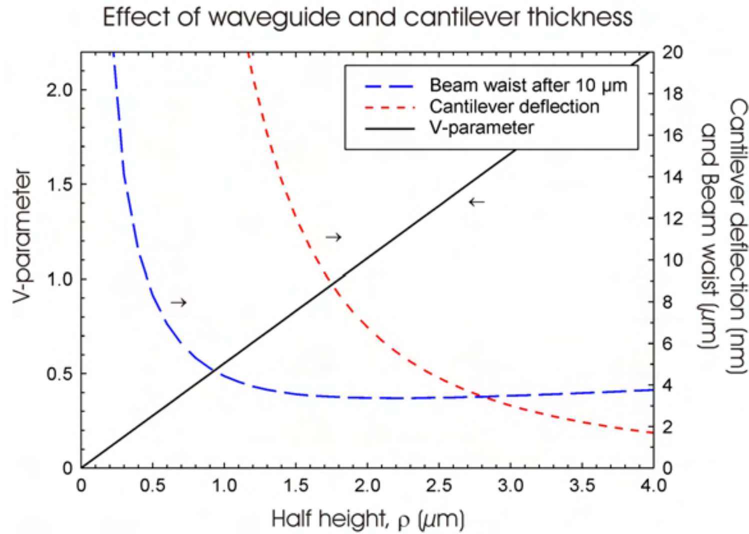

Figure 2.6: Interplay between the three important parameters of the cantilever waveguide as its thickness varies.

tilever. For the calculations the cantilever length is taken to be 200 μm, the distance between the input waveguide and the cantilever is taken as 10 μm and a differential surface stress of 4 mN/m is assumed. This is a typical value of a surface stress change generated by the immobilisation of DNA [23–25].

Previous experience from cantilever fabrication shows that a thickness of 5 μm for a 200 μm long cantilever is a good compromise between mechanical stability during processing and sensitivity for bio/chemical applications [39, 67]. Especially, it is important that the cantilevers will not collapse when submerged in liquid, as for example during development of the polymer. The layer is therefore structured with 4.5 μm thickness. This results in a V-parameter of 1.28 in the vertical direction for the waveguide, which is well below the threshold value of 2.136. The final beam waist when the light reaches the cantilever at this thickness is 3.36 μm. This value is also acceptable since the spread of the beam is not significant. The resulting cantilever bending for a surface stress change of 4 mN/m is 5.6 nm. This is a very small deflection which might be difficult to monitor both in reflection mode as well as in transmission mode. However, other types of molecular recognitions will generate larger cantilever deflections since the surface stress generated is highly dependent on the binding mechanism of the probe molecule and analyte [31, 68]. Moreover, it shall be kept in mind that the aim of this work is to show proof-of-principle of these novel readout mechanisms and for that mechanical stability is more important than

ultimate sensitivity. Figure 2.7 clearly presents the issue where two SEM images of cantilevers fabricated with a thickness of 4.5 µm are compared. The shorter cantilevers are free-hanging whereas the longer cantilevers stick to the bottom of the channel due to non-sufficient mechanical stability.

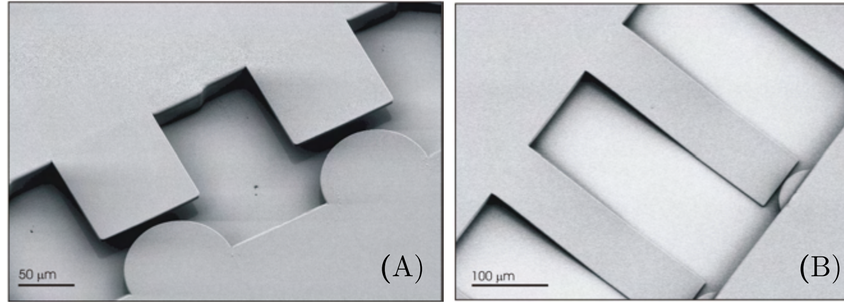

Figure 2.7: SEM images comparing cantilevers that can and cannot support their own weight. (A) These cantilevers are 100 µm long and 75 µm wide. (B) These cantilevers have the same width but are 300 µm long and are seen to collapse during the processing. The input waveguides on these two chips are structured with lenses.

The cantilevers are structured with different widths and lengths to compare the stability and to monitor the effect of process optimisations on a variety of structures. The different cantilever dimensions are listed in table (2.1).

Cantilever	**Width (µm)**	**Length (µm)**
1	50	100
2	50	200
3	75	100
4	75	200
5	75	300
6	100	200
7	100	300

Table 2.1: Dimensions of the cantilevers fabricated in this project. The wider and shorter cantilevers are more stable, which is also seen in figure 2.7. The calibration experiment in Chapter 8 are performed on type 3 cantilevers.

In some systems the end facet of the input waveguide is structured as a lens for improved focusing of the light onto the cantilevers. Unfortunately, this feature was never studied in the project due to lack of time.

Optical circuit

All systems fabricated have four free-hanging cantilevers protruding across a microchannel. The cantilevers also act as output waveguides and there are input waveguides on the opposite side of the microchannel. The gap between the cantilever and the input waveguide is either 5 μm or 10 μm. In the reflection mode the light exits the input waveguide and travels across the gap where the light that hits the cantilever is reflected back towards the input waveguide. Once the light reaches the input waveguide it will couple back and exit the system. For the reflection mode it is therefore only necessary to structure waveguides one side of the channel, directly opposite the cantilever. In the transmission mode the light couples into the cantilever after it has crossed the gap and propagates through this structure and the connected output waveguide out of the chip. This means that there must be two waveguides on opposite sides of the gap and that the cantilever serves as the first part of the output waveguide. Figure 2.8 shows an optical image of a chip with the two light paths schematically drawn.

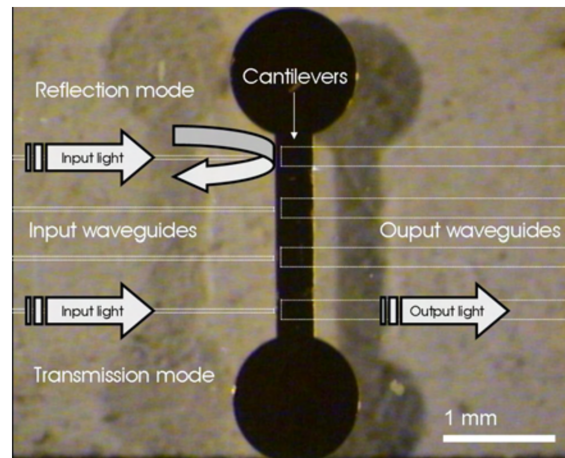

Figure 2.8: Microscope image of the chip layout with the two different read-out modes schematically shown. In the reflection mode (top) the light reflects off the cantilever front-end and couples back into the input waveguide. In the transmission mode (bottom) the light couples through the cantilever and out of the system via the output waveguide. The dark region is the microchannel the cantilevers are situated in.

It was initially believed that it was crucial for the input waveguide and the cantilever to have the same width to ensure a sufficiently good coupling efficiency for the transmission mode. Moreover, it was believed to be crucial that the input and output waveguides should contain s-bends to reduce the amount of stray light collected by the output fiber. Therefore, the

"1st generation" layout was structured with tapers on both the input and output waveguides (tapered down to 10 µm from initial cantilever width) and with s-bends on both sides of the cantilever in opposite directions, figure 2.9.

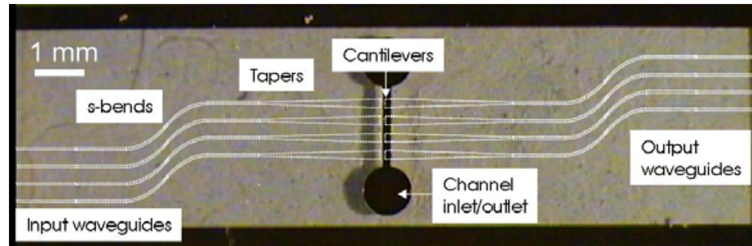

Figure 2.9: Chip layout for the "1st generation" chip structure. The waveguides and the different regions have been marked for clarity. The dark areas at the channel region and outside the chip is the Cr/Au integrated mask, discussed in Chapter 4.

From a design viewpoint the radius of curvature of the s-bends shall be as small as possible to be able to fabricate a smaller system. However, an s-bend with a smaller radius of curvature results in a greater optical loss. The minimum radius ensuring an acceptable loss is determined by the refractive index step and the width of the waveguide [69]. The values are plotted in figure 2.10 for a 3 µm, 5 µm and 10 µm wide waveguide. All waveguides are 4.5 µm high. The optical circuit is based on 10 µm wide waveguides so the radius of curvature needs to be greater than 3 mm. For the design of the 1st generation, the s-bends included have a radius of 5 mm. However, it was later realised that the structures could not guide any light at all. This might be due to a smaller index step than assumed in the calculations. Moreover, it was seen that the extra losses introduced by the tapers exceeded what was gained in increased coupling efficiency. Therefore, the design of the optical circuit is greatly simplified for the "2nd generation" of the system.

For the 2nd generation the input waveguides are 10 µm wide and the output waveguides are tapered down from the cantilever width to 10 µm. This tapering is designed to ensure a good coupling efficiency between the waveguide and the input and output fibers. For reference light paths, four extra 10 µm wide straight waveguides are included in each chip. These waveguides are situated at the edges of the chip and do not interfere with the light guiding at the cantilever area. Figure 2.11 shows an optical image of a 2nd generation chip with the different regions marked.

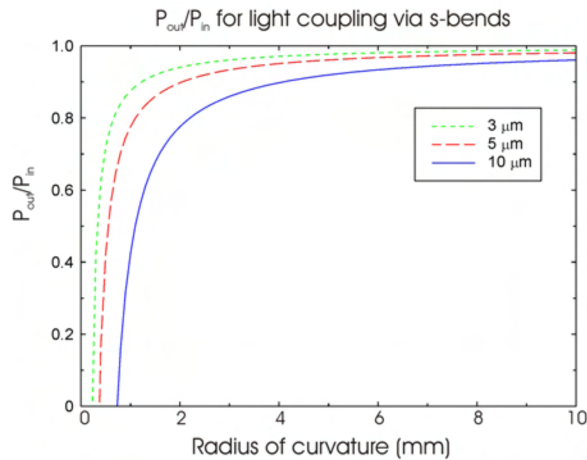

Figure 2.10: With decreasing radius of curvature more light is lost from the waveguide. A 10 µm wide waveguide can have a minimum radius of curvature of 3 mm and still ensure an acceptable propagation loss. The values are calculated for an index step of 0.004.

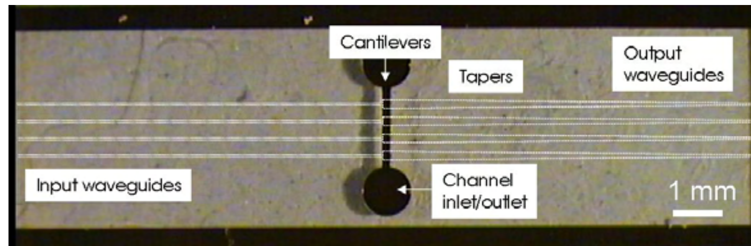

Figure 2.11: Chip layout for the "2nd generation" chip structure. The waveguides and the different regions have been marked for clarity. The dark area at the channel region and outside the chip is the Cr/Au integrated mask used for the fabrication.

Inclined waveguide facets

As previously discussed in the chapter some of the light crossing between different material regions is back-reflected due to Fresnel reflections, equation (2.3). Figure 2.12 shows the situation schematically. When the light exits the input waveguide 4.5 % is back-reflected immediately if the gap is assumed to be filled with air. This light intensity is of the same order as the amount of light coupled back into the waveguide after being reflected off the cantilever front-end. It is the light reflected off the cantilever that is used for the read-out so it is clearly understood that the 4.5 % light directly back-

reflected into the input waveguide significantly reduces the signal-to-noise ratio since the photo-detector cannot differ between the two light sources.

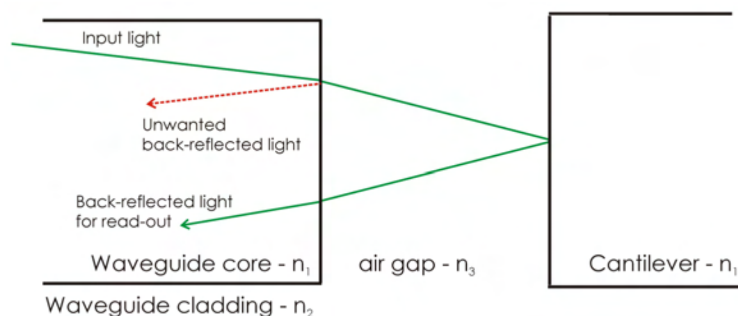

Figure 2.12: Light is reflected both off the input waveguide/air interface as well as off the cantilever front-end. The detector cannot differ these two sources of light so the signal-to-noise level of the read-out mode is low.

To reduce this noise input, the waveguide facets can be structured at an angle to the normal so the back-reflected light from the waveguide facet is not guided by the waveguide. At the same time it must be ensured that the light reflected off the cantilever front-end *is guided*. To ensure this, both the input waveguide facet and the cantilever front-end need to be structured at an angle to the normal. Appendix A shows the full derivation of the possible angles and the limits. Unfortunately, no structures with this feature were studied during the project time, simply due to lack of time.

2.6 Summary

In this Chapter the design aspects and considerations of the system have been discussed. As a summary the different initial requirements stated are listed again to show that most requirements are fulfilled.

- it must be a stable and robust system - *different cantilever dimensions are investigated and the type 3 cantilever is found to be the most suitable one*
- the signal read-out must be straight-forward - *the cantilever deflection is simply read out by an intensity measurement*
- only small amounts of liquids and reagents should be required - *a micro-fluidic system is structured around the cantilevers to ensure that the introduced reagents are directly transported to the cantilevers*

- false-positive and false-negative signals must be kept to a minimum - *multiple cantilevers are structured in every system so that at least one cantilever can be used as a reference cantilever*
- no pre-treatments should be necessary before the system can be used - *this has not been studied during this project but it is anticipated that activation of the cantilevers can be performed before the system is supplied to the customer*
- the processing should be fast and simple - *UV-lithography is a very simple fabrication method with a processing time of approximately three days for a complete batch of chips*
- the full-scale production must be economically profitable - *UV-lithography is available in most production plants and this process can easily be upscaled*
- transportation and storage costs must be minimised - *the final chip has dimensions of only 4 mm × 1.65 cm × 45 μm and the material is very light*
- all parts of the system should preferably be fabricated with the same technique - *all layers are structured with UV-lithography to ensure processing compatibility*
- the product must have many applications to attract a large group of possible customers - *the application of this system is not determined by the fabrication but will be the choice of each end-user*
- the waveguides must be single-mode in the vertical direction - *care is taken to find a material combination and to use the maximum allowed dimensions of the waveguide to ensures this*
- the optical losses in the waveguides should be low - *spectral scans are performed to find the most suitable wavelength of operation*
- the refractive index step is tuned to ensure a good coupling efficiency between the input fiber and the waveguide structures - *the material combination chosen has a NA of 0.14 which compares well with the fiber NA of 0.13*
- the waveguide is in-homogenous, i.e. that there is a small difference in the refractive index of the top and bottom claddings so the mode profile is not perfectly centered in the waveguide - *the effect of variations of process parameters on the resulting refractive index is studied to ensure this even though the same material is used for top and bottom cladding*

- the material choice should ensure high sensitivity of the cantilever - *using a polymeric material with a low Young's modulus ensures a greater deflection for a specific surface stress applied*

- the optical properties of the materials should be known and possible to control - *careful investigations are performed on the effect of processing conditions on the optical properties of the waveguide materials*

Chapter 3

Materials

Based on the requirements for the system as discussed in the previous chapter an all-polymer device is fabricated. The advantages are that polymers as device material result in a softer and more sensitive cantilever and the processing is very cost-efficient. Moreover, during the last couple of years it has been shown that single-mode waveguides with low propagation losses can be fabricated in polymers [70]. During this project, four different polymers are investigated. This chapter discusses each polymer with respect to processing and material properties. This chapter also shows that the optical properties are significantly affected by the processing conditions of the polymers.

3.1 ORMOCERs

The first material combination used belongs to a new polymer range, ORMOCERs, developed by MicroResist GmbH, Germany [71]. These polymers have been developed especially for the MOEMS community by combining good mechanical stability with low optical losses. Several research groups have previously presented work with the polymers where both mechanical structures and waveguides are fabricated [72–75]. The material is made of a hybrid chemical structure with an inorganic backbone (-Si-O-Si-) and organic side chains that ensure a high cross-linking density. The polymer is a negative resist which can be structured with conventional UV-lithography. There are several polymers in the material range and the ones used in this project are *Ormocore* and *Ormoclad*, for defining the core and the cladding of the waveguides respectively. The refractive index difference between the two materials is 0.015 and one of the features of this material combination is that the refractive index can be tuned by mixing the polymers together in different ratios, as shown in figure 3.1. At 1 310 nm the refractive index of pure Ormocore is 1.5400 and the value is 1.5245 for pure Ormoclad [71].

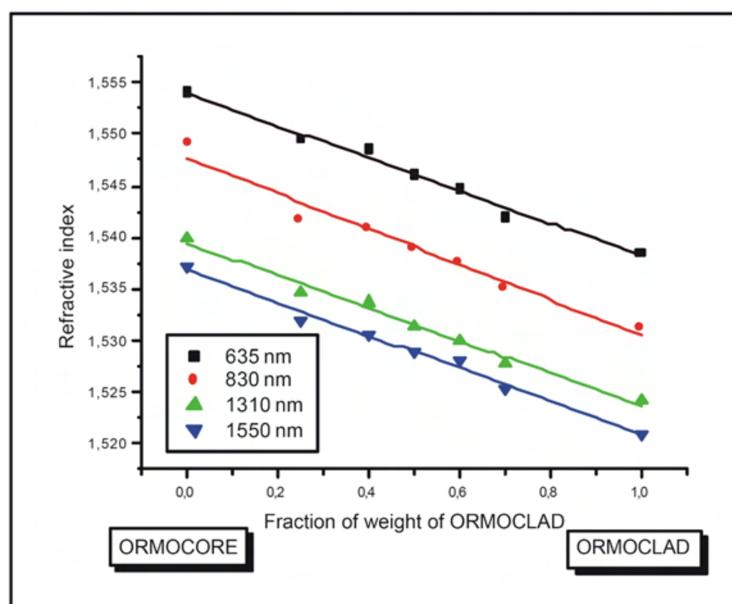

Figure 3.1: The refractive index of the two materials Ormocore and Ormoclad can be tailored by adjusting the ratio of each polymer in the mixture. Reproduced from [71].

The background information provided made the ORMOCERs seem ideal for this project, however once the cleanroom processing started several problems were encountered:

1. The refractive index is tailored by mixing Ormocore and Ormoclad together in different ratios, figure 3.1. This is a rather inaccurate method to control the refractive index of the waveguide structures since the ratio between the polymers can never be fully controlled.

2. It is very difficult to obtain a homogenous and smooth film during spin-coating. Large air bubbles form either during or directly after spin-coating, resulting in large areas with no resist coverage. Several approaches to increase the adhesion between the polymer and the Si wafer were tried such as; a HF (hydrofluoric) dip directly before spin-coating to ensure a perfectly clean Si wafer with no oxide, HMDS (HexaMethylDiSilazane) treatment for increased adhesion commonly used for other resists and storage in 250 °C oven to ensure the Si wafer is completely dry. None of these treatments improved the result. In another approach, the polymers were degassed after dilution with the solvent to remove any excess solvent. However, this did not improve the result either. Figure 3.2 below shows a typical image of an air bubble in the film and the consequences in the final structures.

3. The top surface of the spin-coated polymer film reacts with oxygen from the atmosphere creating an *inhibition layer*. This layer is very sticky and cannot be cross-linked. This inhibition layer results in three significant disadvantages (i) it is a problem during alignment as the mask cannot touch the polymer film which results in reduced pattern resolution (ii) some of the polymer is removed during development. The thickness of the cross-linked polymer can therefore differ significantly from the thickness directly after spin-coating and (iii) the thickness of the inhibition layers depends on the time between spin-coating and cross-linking since it results from the diffusion of oxygen into the polymer matrix. This puts a strict time frame on the process sequence and significantly reduces flexibility in the cleanroom.

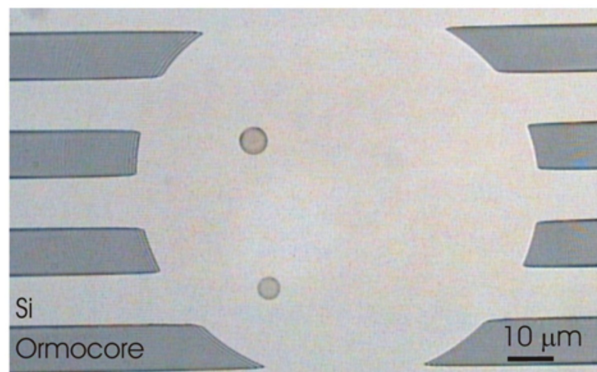

Figure 3.2: It proved impossible to obtain a homogeneous film of Ormocore leaving structures that could not be used.

Since the processing of the ORMOCERs proved to be too difficult the decision was made to move to another material combination and no final systems were fabricated using ORMOCERs.

3.2 SU-8

Since the Nanoprobe research group holds previous experience from working with the UV-sensitive polymer SU-8 and has previously shown that SU-8 cantilevers can be fabricated [38, 39], this material presented itself as an obvious alternative when the ORMOCERs proved not to be suitable. Moreover, other research groups have shown that SU-8 is a good candidate as waveguide material for integrated optics, both for fabricating multi mode waveguides [76,77] and for the fabrication of single-mode waveguides [78–80]. To be able to fabricate waveguides with low coupling loss the index step between the core and the cladding must be tailored to fit the NA of the input

fiber. This has previously been achieved by Ruano-López *et al.* by diluting SU-8 with a liquid aliphatic epoxy resin and using this mixture as cladding material together with a SU-8 core [81]. No such mixtures were required in this work because in early 2005 MicroResist, that also are the suppliers of SU-8, launched a new product; the mr-L XP series. These resists are developed as an alternative to SU-8 for micro fabrication processes where problems with delamination and cracking as a result of high intrinsic stress commonly are seen [82]. In fact, mr-L is a modified version of SU-8 where a plasticizer, *propylene carbonate*, simply is added to reduce the intrinsic stress and provide a more flexible material [71]. Due to this addition, the refractive index is also modified, which makes it suitable as cladding material surrounding a SU-8 waveguide core. The two materials are also based on different solvents; SU-8 is based on cyclopentanone and mr-L is based on γ-glycolacetate, which might also be a reason for the slight difference in their refractive indices.

3.2.1 Processing

Both SU-8 and mr-L can be structured with UV-lithography [83]. The first step of the processing is to spin-coat the films onto a carrier wafer (typically Si or Pyrex). The thickness of the film is determined by the viscosity of the polymer solution and the spin speed.

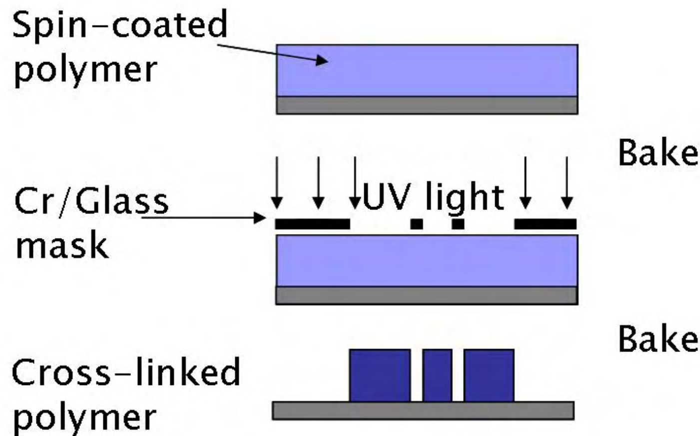

Figure 3.3: Both SU-8 and mr-L are negative resists where the pattern from the photo-mask is transferred into the polymer layers by exposure to UV light. The exposed areas cross-link upon a consecutive baking step.

Afterwards, the wafers are baked on a programmable hotplate in a two-step-process at 60 °C and 90 °C to evaporate the solvent from the film. The patterns are transferred into the film by exposing the polymer to UV light, *i-line* 365 nm, through a photo-mask. A consecutive baking step, again at 60 °C and 90 °C, induces cross-linking of the polymer and defines the pattern. This step is called the post-exposure bake (PEB). The non-exposed areas can afterwards be developed in the solvent PGMEA (poly glycol methyl ether acetate). The process flow is shown schematically in figure 3.3. The process sequence containing all parameters for this system is found in Appendix B.

3.2.2 Refractive index variations

It is crucial to know the effect of the processing on the final values of the refractive index of the polymers to ensure optimal waveguiding. Most polymers are known to be highly affected by changes in their processing [84–86] and it has previously been reported in the literature such changes also affect the value of the final refractive index [87].

Caused by the processing

To analyse the effect of the processing on the resulting refractive index six wafers of cross-linked SU-8 2005 and mr-L 6050 are prepared. The wafers are divided into three batches processed at different temperatures: 60, 90 or 110 °C. Both soft bake and PEB are performed at the same temperature. Moreover, each wafer is divided into six areas which are exposed to different dosages of UV light. The same lamp with an intensity of 9.0 mW/cm^2 is used and the exposure time is varied between 10-70 s in 10 s intervals. All six areas on the wafer are flood-exposed. The refractive index of the different areas is measured using a prism coupler (Metricon 1020, Pennington NJ, USA), which measures both the film thickness and refractive index using a fitting routine [88]. A profiler (Tencor P-1, Tencor Instruments, USA) is used to measure the thickness of the cross-linked films as a means to calibrate the prism coupler. The value of the thickness measured by the prism coupler is compared with the value from the profiler and no significant deviation is observed. The prepared samples are used for all investigations of the stress in the film caused by the processing described in this section.

The resulting refractive indices from the process variations are plotted in figure 3.4. For clarity of presentation only three exposure dosages are presented, corresponding to under exposure (20 s), optimised exposure (30 s) and over exposure (40 s). It can clearly be seen that with increasing exposure dosage and increasing processing temperature, the refractive index of

the films *decrease*. The same trend is seen for both polymers. The reason for this is not fully understood but it can probably be attributed to either (i) increased cross-linking density (ii) reduced solvent content or (iii) significant increase of the intrinsic stress. However, it shall be noted that the *refractive index step* i.e. the difference between the core refractive index and the cladding refractive index remains more or less constant at 0.004. Furthermore, it is seen that the refractive index of the cladding material is always lower than the refractive index of the core material. This means that the material combination is still suitable for waveguide fabrication as long as the same process sequence is always applied, to ensure that a known refractive index is obtained.

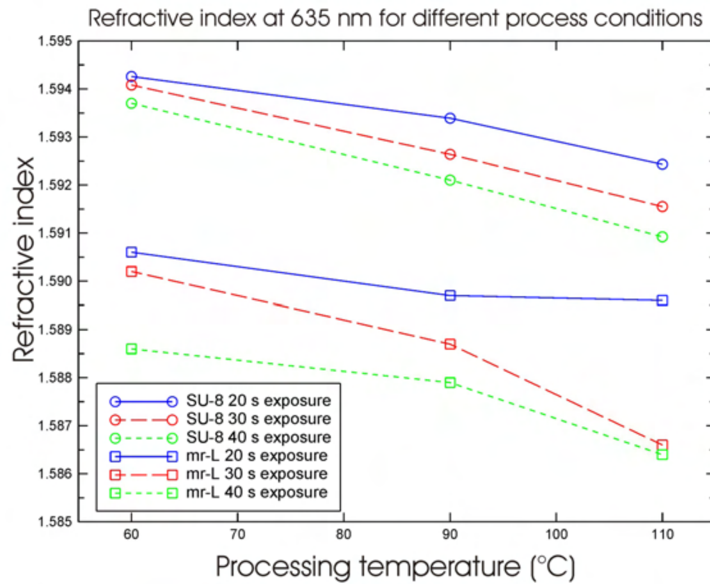

Figure 3.4: The refractive index of both SU-8 and mr-L is seen to be highly dependent on the process conditions with decreasing values for both increased temperatures and increased exposure dosages.

The second experiment with the samples is to monitor the effect of further baking steps, so-called *hard bakes*. The data is presented in figure 3.5. Here, the same samples initially processed at 60, 90 and 110 °C are used. The refractive index is measured directly after processing and after a following hard bake (hb) at an elevated temperature of either 90 °C or 120 °C. It can be seen that the film processed at 60 °C is affected by both hard bakes and the film processed at 90 °C is affected by the bake at 120 °C. However, the film processed at 110 °C is not affected by the hard bake at 90 °C.

It is also interesting to note that the resulting values of the refractive index after the films have been baked at the same temperature coincide, even for the samples initially processed at different temperatures. This is seen in figure 3.5(A) where the values of the films processed at 60 °C and 90 °C have the same value of the refractive index after the 120 °C bake.

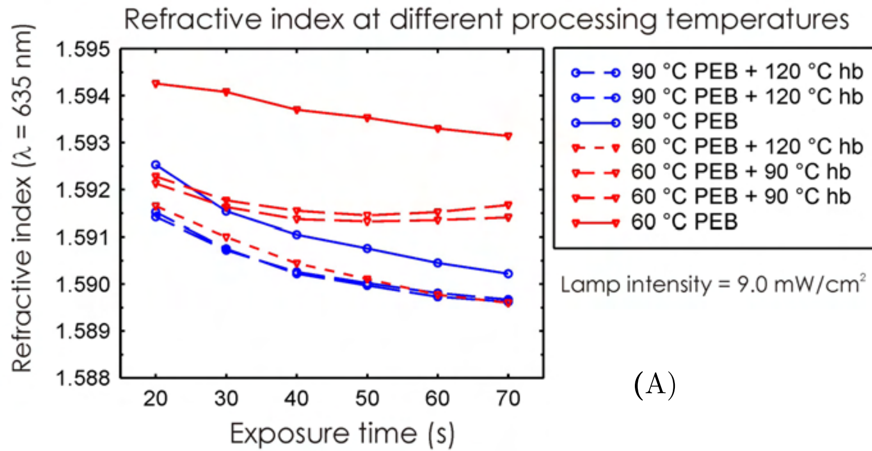

(A)

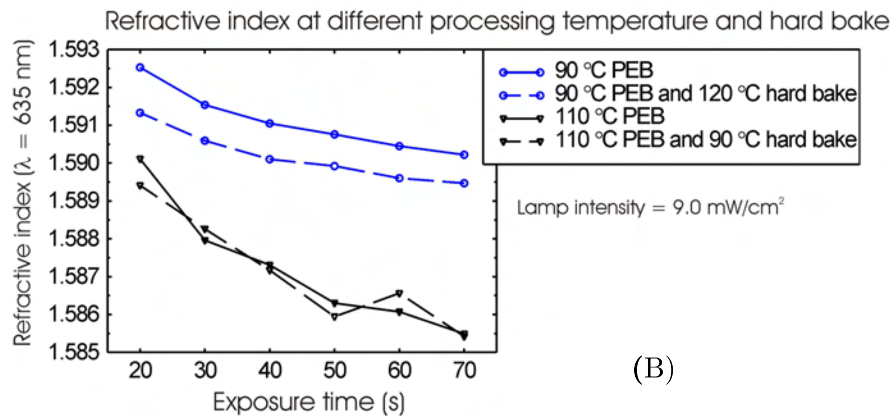

(B)

Figure 3.5: The temperature of the hard bake must exceed the PEB to have an effect on the refractive index. (A) Repeated hard bakes at the same temperature results in the same refractive index every time. (B) The film processed at 110 °C is not affected by a hard bake at 90 °C since the temperature is not greater than the PEB temperature.

From these observation it can be concluded that the temperature of the hard bake needs to be higher than the processing temperature to change the refractive index and that it is the highest temperature the film is subjected to that determines the value of the final refractive index, independent of the initial processing temperature. This finding is very important because it means that temperature fluctuations during bio/chemical measurements

with this type of chip will not affect the refractive index of the system as such fluctuations very seldom exceed 90 °C, which is the standard processing temperature. Such fluctuations in the refractive index would result in artifacts in the read-out and these must be confirmed not to be present.

In the last set of experiments the effect of a second UV dosage and the resulting change of the refractive index is monitored. These results are presented in figure 3.6. Here, only the sample processed at 90 °C is shown for clarity of presentation. It can be seen that the refractive index of the film is not changed if the film is only exposed to UV light but with a following baking step the refractive index is decreased significantly. This finding also points in the direction that it is an increase in cross-linking density of the polymer that is the underlying factor of the variations in the refractive index. However, according to the theory of polymer physics an increase in cross-linking density will *increase* the refractive index and not decrease the value as observed here [89].

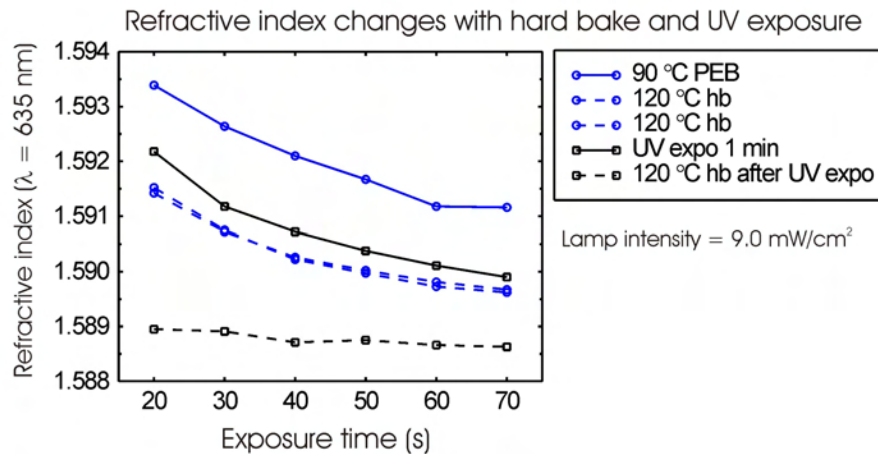

Figure 3.6: The refractive index is not decreased by only exposing the polymer to UV light but a following hard bake decreases the value considerably.

The observation clearly stresses the importance of developing an optimised process sequence for the fabrication and to always use the same parameters. Moreover, this also indicates that the refractive index of the top and bottom mr-L cladding will not be identical in the final structures due to the extra processing the lower cladding is subjected to during the patterning of the waveguide core layer and the top cladding. This is further discussed in Chapter 6.

Relation to stress

Since the observation of the change of the refractive index from the process variations is not supported by the theory of polymer physics a further set of experiments is conducted where changes in the refractive index and the correlation with the stress in the polymer film is investigated. It is known from photo-elastic theory that stresses in a polymer film will affect the refractive index of the material [90] and the effect is shown on polymeric waveguides in the literature [91]. It is therefore crucial for this process to ensure a good control of the material stresses. The samples for this set of experiments are processed at different temperatures: 60, 90 and 110 °C. For all samples a 4.5 µm thin film of SU-8 is spin-coated onto a Si wafer. The films are soft baked at 10 min at their respective temperature, exposed for 30 s at an intensity of 9.0 mW/cm^2 and subjected to PEB for another 10 min at their respective temperature. The stress in the film is found by scanning the wafer before the polymer is deposited and after the film is cross-linked with a profiler to measure the radius of curvature of the wafer. This method uses the theory developed by G.G. Stoney [60] which relates the radius of curvature of the wafer to the stress of the thin film, equation (3.1).

$$\sigma_f = \frac{E_s}{6(1-\nu_s)} \frac{t_s^2}{t_f} \frac{1}{R} \tag{3.1}$$

where σ_f is the stress in the film, E_s and ν_s are the Young's modulus and Poisson ratio of the substrate respectively, t_s and t_f are the thicknesses of the substrate and the film respectively and R is the radius of curvature of the wafer.

Both the refractive index and the stress in the films are measured directly after processing. To induce further stresses in the films the wafers are baked on a hotplate for 2 min and directly afterwards, the measurements of both the refractive index and the stress are repeated. The values are measured again a few days later (3 days - 1 week) to see if any stress release occurs and how this affects the refractive index. The wafers are baked twice at 90 °C and twice at 120 °C. Both 90 °C bakes are performed before the 120 °C bake since it was previously noted that the temperature has to be increased to be effective, figure 3.5. The data obtained is presented in figure 3.7 where the refractive index is plotted with a line and the stress is represented by the columns. From the graph it can clearly be seen that further heat treatments decrease the refractive index and increase the stress in all films. It is also interesting to note that this trend is not static but at every "resting point" the values start to return towards their initial level. However, during the experimental time period the values are not seen to return fully. Another interesting observation is that both the refractive index and the

stress values of all three samples converge towards the same value; 1.5910 for the refractive index and 22 MPa for the stress. In fact, the spread between the values directly after processing is 0.0013 units and 9.8 MPa but after the last 120 °C bake the spread is reduced to only or 0.00025 units and 1.9 MPa. Both values have decreased their spread by 80 %.

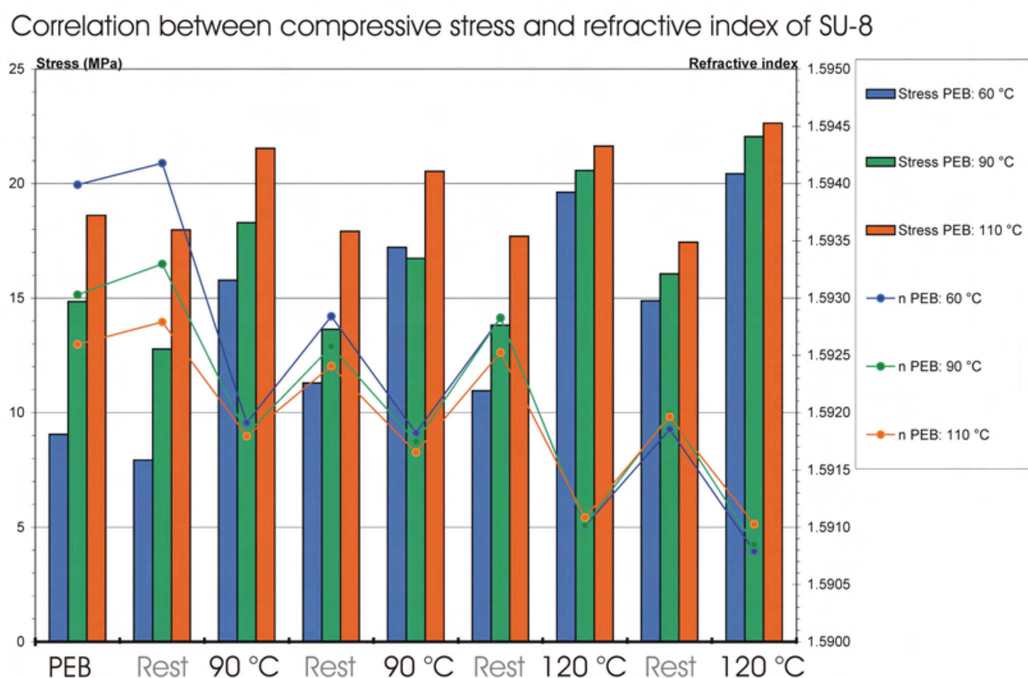

Figure 3.7: Correlation between refractive index and stress in SU-8. The stress is represented by the columns and it is seen to increase after every baking step. The refractive index is plotted in the lines and it is seen to decrease with the baking steps. The values converge towards the same values for all samples; 1.5910 for the refractive index and 22 MPa for the stress.

From the data in figure 3.7 the correlation between increased stress in the film and decreased refractive index seems straight forward. However, two alternative explanations for these trends are also considered. Possibly, not all solvent is evaporated during the soft bake of the film processing but extensive further heat treatments are required. This explanation is supported by the observation that the most noticeable change is seen for the sample processed at 60 °C. Since all wafers are baked for the same amount of time during soft bake and PEB (10 min) less solvent will have evaporated from this film and a more significant difference will be seen after the following hard bakes. Alternatively, the change in refractive index is explained by the evaporation

of water from inside the polymer film during the baking steps. To investigate this a reference sample is stored in a N_2-box after a 120 °C bake. If the refractive index is increasing as a result of re-absorption of evaporated water then no change should be seen for this wafer. However, the same behaviour was observed for this wafer compared with the other wafers that were not stored in a controlled environment, so this cannot be the explanation.

In conclusion, the explanation for the refractive index variations seen with changes in processing and further heat treatments is most likely the increase in stresses of the polymer films. Stress is induced in the polymers as thermal stress during the cool-down of the PEB after cross-linking (when the polymer matrix is fixed) due to the mis-match of the thermal expansion co-efficients of the polymer film and the Si substrate. Moreover, it can be concluded that the value of the refractive index is determined by the highest temperature the film is subjected to, figure 3.8.

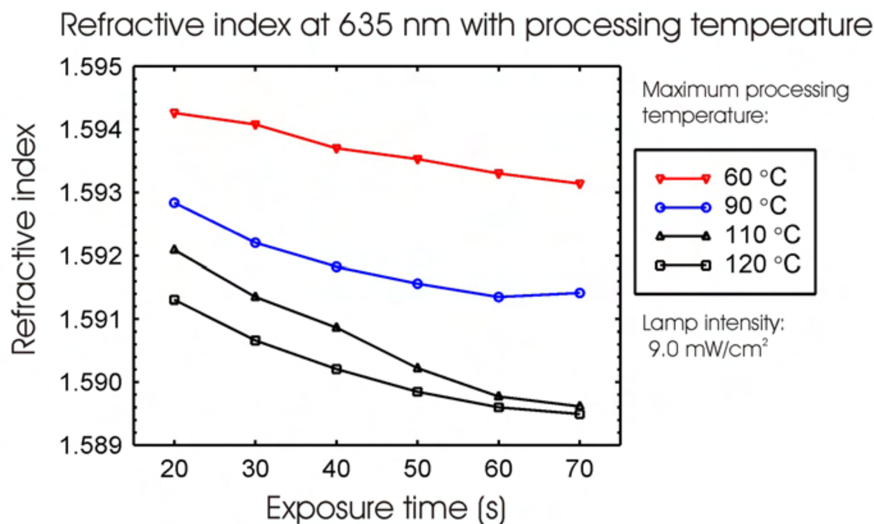

Figure 3.8: The refractive index of the SU-8 is determined by the maximum processing temperature the film is subjected to. This change is attributed to the stress in the film, which is directly linked to the maximum temperature of the processing which induces thermal stress in the polymer film.

Throughout this section the refractive index is measured at 635 nm. The system is operated at a final wavelength of 1 310 nm so to obtain an expected value of the refractive index at this wavelength the light source in the prism coupler is exchanged to a diode at 1 550 nm. One calibration experiment is performed where the refractive index is measured both at 635 nm and 1 550 nm when the polymer film is subjected to a baking step. The same

change in the refractive index is seen at both wavelengths. It is therefore valid to assume that the difference will be the same for all process steps. No significant difference is expected in the refractive index of the SU-8 at 1 310 nm compared to the measured value at 1 550 nm since the refractive index of SU-8 changes most drastically in the region 100 - 800 nm and then reaches a fairly wavelength independent level of $\sim$ 1.57 [92]. Therefore, the refractive index at 1 310 nm can be calculated from the measurement at 635 nm. The values of the refractive indices of the final waveguide structures are listed in table (3.1).

	λ = 635 nm	λ = 1 550 nm
SU-8 core	1.5912	1.5725
mr-L top cladding	1.5871	1.5683
mr-L lower cladding	1.5841	1.5653
Δn_{low}	0.0041	0.0042
Δn_{top}	0.0071	0.0072

Table 3.1: Refractive index of final waveguide structures at the different wavelengths. It is assumed the value of the refractive index is the same at 1 310 nm as measured at 1 550 nm. The value of the refractive index of the lower cladding has a lower value due to the extra process steps this layer is subjected to.

3.2.3 Stress-optical co-efficient

The relation between changes in the refractive index caused by changes in the stress of the material is represented by the *stress optical co-efficient,* κ.

$$\kappa = \frac{\Delta n}{\Delta \sigma} \tag{3.2}$$

where n is the refractive index of the material and σ is the stress.

For the films used in the previous experiment, the stress-optical co-efficient is plotted for the different processing temperatures, figure 3.9(A). It can be seen that the processing temperature does not affect the value of the stress optical co-efficient significantly. The average value is (-2.64 $\pm$ 0.1) $\times$ 10^{-4} MPa^{-1}. The structures for this project are all processed at 90 °C with a stress optical co-efficient of -2.57 $\times$ 10^{-6} MPa^{-1}. The cladding polymer, mr-L has a slightly lower stress optical co-efficient of -1.64 $\times$ 10^{-6} MPa^{-1}, figure 3.9(B). Experimental results with these waveguide materials have not been presented in the literature before.

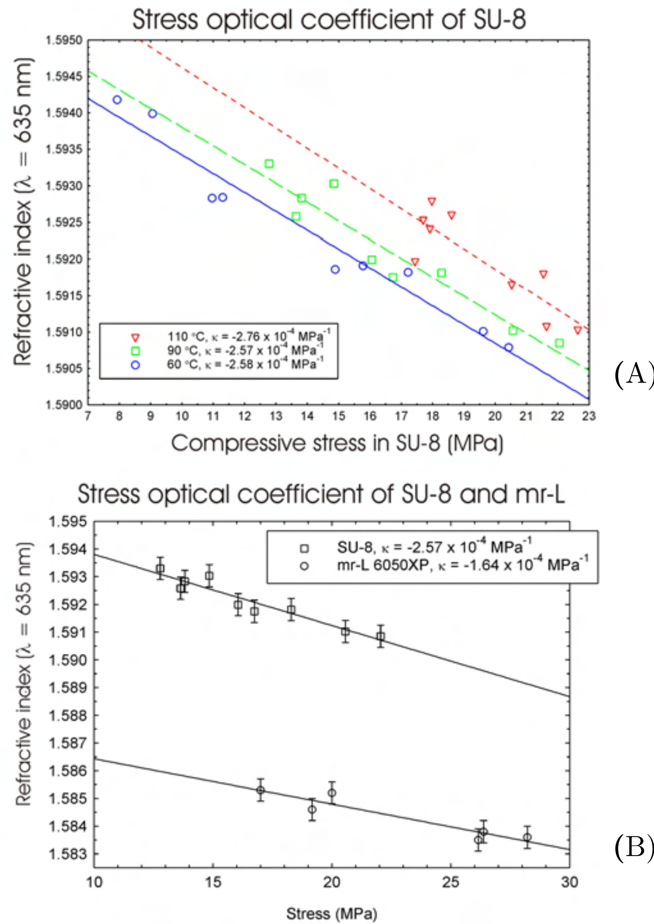

Figure 3.9: (A) The stress optical co-efficient of SU-8 samples processed at different temperatures. The value is not significantly changed with increased processing temperature. The processing temperature is listed in the legend. (B) Stress-optical co-efficient of both SU-8 and mr-L. The value is slightly lower for the mr-L cladding material.

When the probe and detection molecules bind onto the top surface of the cantilever a surface stress is generated. It is therefore crucial to ensure that this process does not affect the refractive index of the material, as that would result in an artifact in the read-out. A typical surface stress generated from the immobilisation of DNA onto the cantilever is 4 mN/m [23–25]. Assuming the layer constituting the probe molecules and analyte has a thickness in the nm-region, the resulting stress in the cantilever is in the order of 1 MPa. This will only result in a refractive index variation of $\sim 10^{-6}$ which is negligible.

3.2.4 Spectral absorption

The chemical structure of the SU-8 monomer is shown in figure 3.10 with its different chemical bonds marked. The material cross-links via cationic ring-opening polymerisation of the epoxy groups [93] so the number density of epoxy groups is considerably lower in the cross-linked polymer compared with the monomer solution. When light travels through the material the chemical bonds absorb energy via vibrational excitation [94], which leads to significant losses in the material. It is therefore crucial to know at what wavelengths the material absorbs the least.

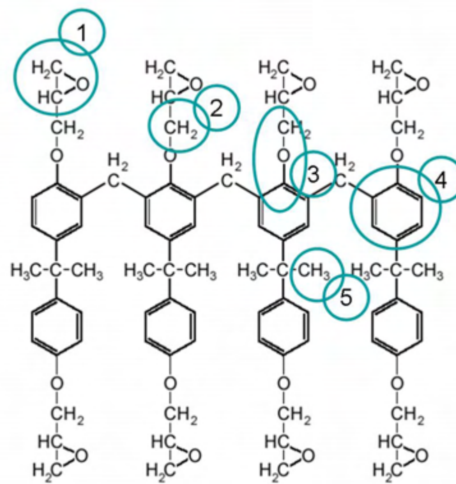

Figure 3.10: The different chemical bonds in the SU-8 monomer are marked. Vibrations of these bonds are excited by light traveling through the material leading to propagation loss.

The absorption loss of the material is measured by propagating white light through a 10 µm wide, 4.5 µm high and 20 mm long waveguide and measuring the intensity of the output light over the spectral range 800 - 1 700 nm. This experimental method is described in more detail in Chapter 6. Figure 3.11 shows the total loss for this waveguide and each chemical bond of the polymer is seen to be represented in the spectra. The chemical group (-C-O-C-) does not absorb within this spectral range. The peak at 1 430 nm is difficult to interpret since it is -NH_2 that absorbs at this wavelength but there are no such chemical groups in the SU-8 monomer. It might be that this absorption peak is accounted for either by the photo-initiator of the SU-8 polymer or by the added plasticizer in the cladding material. Alternatively it might be the -OH absorption peak expected at 1 440 nm that is slightly shifted. The -OH bonds are generated during the cross-linking and

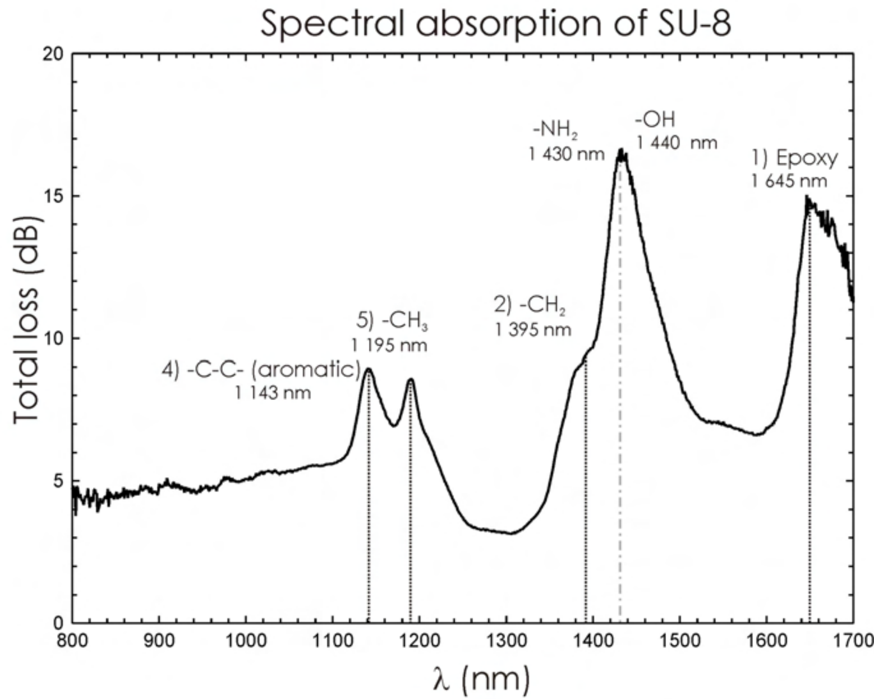

Figure 3.11: Waveguides fabricated in SU-8 are best operated in the second telecommunication window at 1 300 nm or at 1 580 nm where the vibrational absorption of the material has minima.

this chemical group is known to absorb strongly, which manifests itself as a large and broad peak in the spectra. It can be seen that the preferred operating wavelength of these waveguides is 1 300 ± 20 nm or 1 580 ± 10 nm.

3.2.5 Birefringence

Birefringence is the phenomenon where the effective refractive index (n_{eff}) of the two polarization states are different, an effect generated both by a dimensional component and a stress component [95]. As previously mentioned, the stress of the waveguides discussed here is very low and not believed to contribute significantly to the birefringence. The dimensions in the horizontal and vertical direction are different and this will probably lead to a small birefringence. However, the optical detectors used in all the experimental work are not polarisation dependent and the effect of birefringence is therefore not studied.

3.3 Summary

Here, the material properties of the SU-8 and mr-L polymers are presented. The fabrication process is described and the experience from working with two alternative materials is briefly mentioned. The material properties such as vibrational absorption are analysed and it is noted that the best wavelengths to operate such a system at is 1 300 ± 20 nm or 1 580 ± 10 nm.

Moreover, the effect of the process sequence on the refractive index is investigated and it is shown that it is highly important to always apply the same process parameters to achieve systems with the same optical properties. A refractive index of the SU-8 core material of the final device is measured as 1.5725 at 1 550 nm. The value for the mr-L cladding layer subjected to only one exposure dosage is 1.5683 and the value for the other cladding layer is 1.5653 due to the extra process steps this layer is subjected to.

Chapter 4

System fabrication

A novel fabrication method is developed to achieve a direct fabrication of free-hanging cantilevers. This chapter presents the different steps in the fabrication of the complete system and the important parameters are discussed. The fabrication process can be used both to structure a system with completely embedded waveguides or with buried channel waveguides using air as top cladding. The exact process sequence is found in Appendix B.

4.1 Negative resists and free-hanging structures

Both SU-8 and mr-L are negative resists, which means that the exposed areas cross-link. This in turn means that in a two-layered structure the top layer cannot be structured as free-hanging over the lower layer simply because the UV light used to cross-link the top layer penetrates through and irradiates the bottom layer as well. Therefore, cantilever chips fabricated by UV-lithography have to be fabricated up-side-down, with the cantilever closest to the Si carrier wafer and the supporting chip body processed on top [38, 96]. This is schematically shown in figure 4.1.

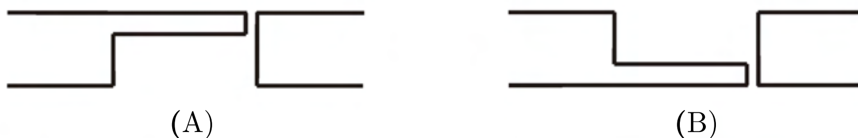

Figure 4.1: Schematic drawing of the limitations of negative UV-resists. (A) It is not possible to directly cross-link a free-hanging cantilever on top of its chip body. (B) Therefore, cantilever chips need to be fabricated up-side-down.

Usually, the procedure of fabricating the cantilevers up-side-down does not present a problem since the chip can easily be turned after the release if that would be necessary for the set-up used for the measurements. However, the system fabricated in this project requires three layers; lower cladding layer, cantilever waveguide layer and top cladding layer. This puts some restrains on the fabrication technique since it is not possible to fabricate free-hanging cantilevers on top of the lower cladding layer and furthermore it is not possible to spin-coat and structure the top cladding onto a free-hanging cantilever. Therefore, a novel fabrication method is developed.

In the literature a few interesting fabrication techniques that possibly could be used here are presented. Metz *et al.* show the fabrication of SU-8 microchannels using poly(propylene) carbonate and poly(ethylene) carbonate as sacrificial layers [97]. The technique might be suitable as the sacrificial layer can be kept underneath the cantilevers for support during the processing of the top cladding. At the end of the process the sacrificial layer is removed by a heat treatment. It is an advantage that no liquids are introduced since the free-hanging cantilevers can have difficulties to withstand the capillary forces if submerged. However, the minimum thicknesses of the channel cover layer fabricated in this work is in the range of 10 μm, which is not sufficiently thin for the fabrication of microcantilevers. Moreover, temperatures between 200 - 300 °C are required to decompose the sacrificial material as the final step of the process. Another interesting fabrication method has been presented by Daniel Haefliger in the Nanoprobe research group. He shows the fabrication of free-hanging cantilevers utilising soft-lithography to pattern an 'integrated mask' on the support layer [98]. This process technique allows for the fabrication of structures down to a thickness of ~4 μm, and could be a possible fabrication technique to use for this type of system. The integrated mask can remain on the cantilevers for support during the processing of the top cladding layer.

While developing this new fabrication procedure a similar process method was published by M. Agirregabiria *et al.* [99] where the fabrication of multi-layered SU-8 structures by successive bonding and releasing steps is shown. Some of the differences between these two methods are that (i) M. Agirregabiria *et al.* bond two cross-linked SU-8 layers together without using any intermediate gluing layer (ii) they use Kapton [100] as the release layer and (iii) they do not use the Pyrex wafer as part of their final device. Moreover, the fabrication process presented here does not require any violent release steps (M. Agirregabiria *et al.* use ultra sound for this) and the fabrication method presented here adds a further level of process flexibility by the addition of the integrated Cr/Au mask. All this is discussed further in the next section.

4.2 Novel fabrication method

The principle of this new fabrication method is to fabricate half the system (cantilever waveguide layer and top cladding) on one wafer up-side-down as shown in figure 4.1(B) and then transfer these structures onto a lower cladding layer via two consecutive bonding steps. In total, three wafers are included in the fabrication process - denominated *Wafer A*, *Wafer B* and *Wafer C* - and of these two can be re-used. Below follows the different steps in the process. First, the preparation of each wafer individually is described and afterwards the bonding and transfer procedure is explained.

Wafer A: This is a Si wafer where the half chips are structured and fully developed before the subsequent bonding steps. Before structuring the SU-8 layer the wafer is coated with a thin fluorocarbon film. The fluorocarbon film serves as a release layer for the structures in the final step [101, 102]. Investigations of this release layer are presented in section 4.4.

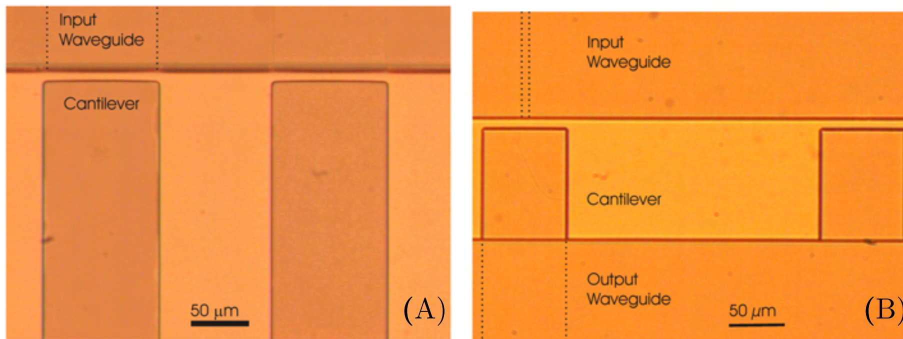

Figure 4.2: Microscope images of two cantilevers situated in the micro channel after the development of the half chips on Wafer A. The outline of the waveguides are marked for clarity. The gap between the input waveguide and the cantilever is 10 μm. (A) In the 1st generation design the input waveguide and the cantilever have the same width. (B) For the 2nd generation design the input waveguide is always 10 μm wide independent on the cantilever width.

The cantilever waveguide layer is spin-coated to a thickness of 4.5 μm. The cantilevers are structured to different dimensions as listed in table (2.1). The gap between the input waveguide and the cantilever is either 5 μm or 10 μm. The cantilever waveguide layer is exposed in hard contact mode and baked on a hotplate for 20 min before the non-exposed areas are developed in PGMEA. The mr-L top cladding is spin-coated to a thickness of 22 μm and exposed in hard contact mode. The exposure dosages and baking times are optimised to ensure a sharp edge profile of the top cladding at the end facet of the input waveguide. Moreover, the exposure is optimised for

perfect alignment of the top cladding and the input waveguide facet. Figure 4.2 shows microscope images of a top view of the cantilevers in the channel after both layers are cross-linked and developed. On the left hand side of the images the input waveguides are marked for clarity. Profiler measurements (Dektak 8, Veeco Instruments, USA) across the whole wafer show an average height variation of only 1.69 µm. However, close to the channel a maximum protrusion of the waveguide layer through the top cladding of 5.52 µm is seen. This is because the top cladding is not able to fully compensate for the height variation caused by the waveguide layer due to the close proximity of the wide output waveguides. Figure 2.1(C) in Chapter 2 shows this effect schematically.

Wafer B: This wafer is a Pyrex wafer with an integrated mask patterned directly on the wafer. Therefore, the channel structures are patterned in a Cr/Au metal layer onto the wafer. The Pyrex wafer is first cleaned in soap (Triton X-100, Union Carbide, USA) and ultra sound for 20 min followed by 10 min of piranha (H_2SO_4 + H_2O_2) at 80 °C. The metal layer is patterned by conventional lift-off using the photo-resist AZ5214E (Hoechst, Frankfurt am Main, Germany). The Cr layer is used as an adhesion promoter for the Au mask. Afterwards, a 5 µm thin layer of SU-8 is spin-coated onto this wafer and soft baked. This layer acts as a bonding layer in the first bonding step and the layer is spin-coated to a thickness of 5 µm to compensate for the height variations noted on wafer A above.

Wafer C: This wafer is also a Si wafer coated with a thin layer of fluorocarbon. On this wafer a 22 µm thick layer of mr-L is spin-coated and soft baked. The mr-L layer serves as the lower cladding layer that the half chips are bonded onto.

At this stage all three wafers are prepared and the process of bonding them together is started. All bonding steps are performed in a bonder (EVG-NIL, EV Group, Austria) with temperature control on both top and bottom wafer holders, a controllable piston force and the possibility to evacuate the chamber before bonding to prevent the entrapment of air in-between the wafers. Moreover, it is possible to align two wafers before bonding them together, a feature that is used when bonding wafer A and wafer B. Figure 4.3 shows the remaining process steps labelled 1-6. Each step is discussed individually below in the text, referring to its process number, with comments about the specific considerations that need to be taken. The steps shown in figure 4.3 comprise the optimised process sequence. The next section discusses some process difficulties encountered and alternative processes sequences developed.

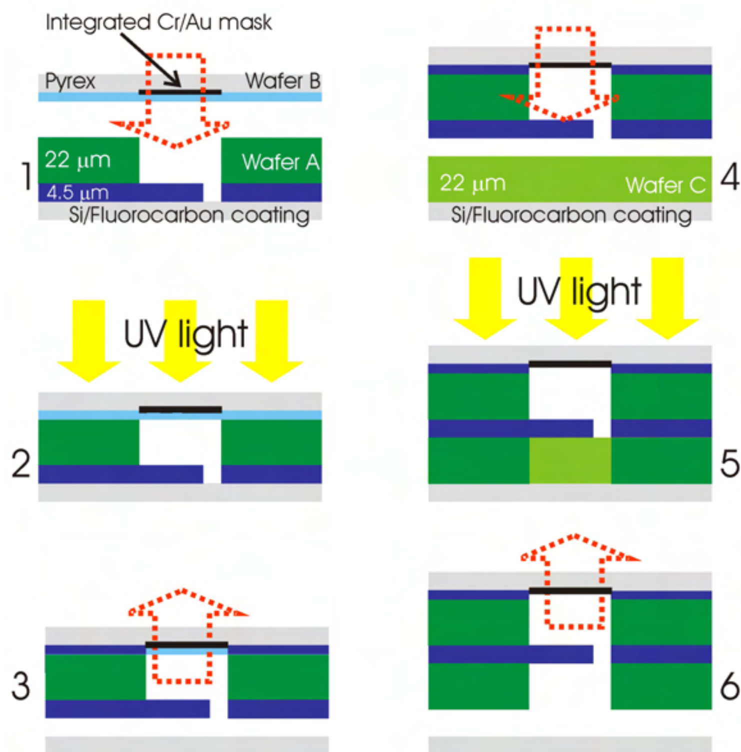

Figure 4.3: When the three different wafers are prepared, the final system is fabricated in a six-step-process. The different steps and their respective requirements are discussed in the text. The exact process sequence with all parameters is found in Appendix B.

1. The Si wafer with the structured chips (wafer A) and the Pyrex wafer with the integrated Cr/Au mask (wafer B) are aligned and placed in the bonder. The chamber is evacuated in a two-step-process as the wafers simultaneously are heated up to 90 °C. When the set temperature is reached the wafers are pressed into contact with a piston force of 1 000 N. The temperature is maintained at 90 °C for 30 min before a slow cool-down back to room temperature is started. The piston force is not released until both wafers have reached a temperature of 30 °C. Figure 4.4 shows the variation of the chamber pressure, piston force and chuck temperatures during the first 50 min of the process. The total time of the process is 6 hours due to the slow cool-down of the top wafer holder. In this step the 5 µm layer SU-8 spin-coated onto wafer B acts as a gluing layer between the two wafers. When the wafer chucks heat up the SU-8 becomes free-flowing and compensates in height for the waveguide protrusions on wafer A.

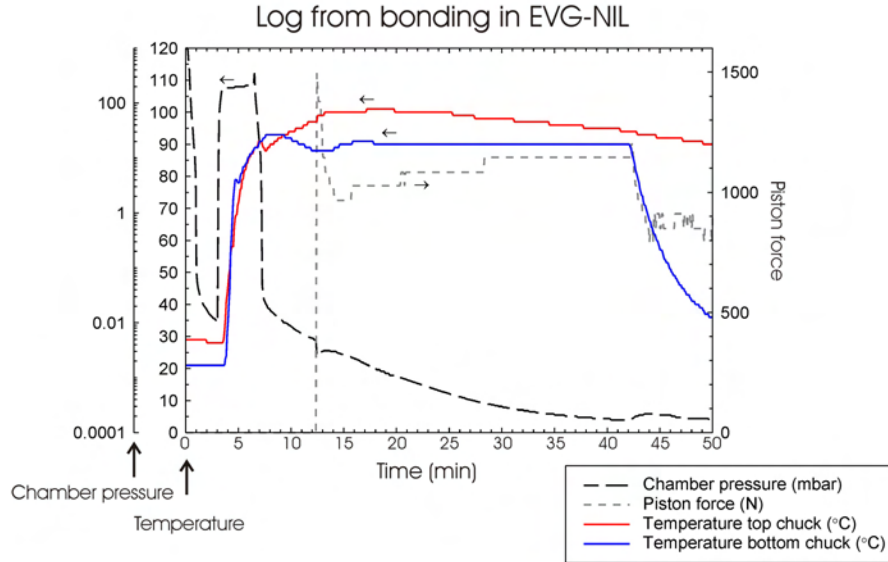

Figure 4.4: The chamber pressure, piston force and chuck temperature monitored during the first 50 min of the bonding process, which corresponds to the active bonding period. After 45 min a strong bond is obtained between the wafers and the wafer holders are cooled back down to room temperature. The piston force is set to remain at 1 000 ± 100 N for the remaining process time.

From the optimisation of the process it is seen that (i) both top and bottom wafer holders need to be heated up to ensure that the SU-8 layer reaches a temperature above its *glass transition temperature* (∼ 50 °C) and becomes free-flowing (ii) the wafer holders need to remain at this elevated temperature for at least 30 min to ensure that the SU-8 has time to fill all gaps (iii) the piston force shall not be released before both wafers have reached a temperature below 30 °C to avoid sliding the wafers out of alignment (iv) a maximum force of 1 000 N shall be used as a greater force destroys the chips.

2. The wafers are taken out of the bonder and exposed to UV light in a standard mask aligner (MA-6, Karl Süss, Switzerland) in flood-exposure mode. Here, the integrated Cr/Au mask protects the cantilever region from exposure. The thin SU-8 layer is cross-linked in a consecutive PEB ensuring a tight bond between the structured chips and the SU-8 coated Pyrex wafer. The wafers are baked with the Pyrex wafer facing the hotplate to ensure the thin SU-8 layer is heated up to 90 °C. During the previous bonding step SU-8 flows down into the

channel where the cantilevers are situated. Figure 4.5 shows the importance of a good alignment between the patterned chips and the Cr/Au mask. In figure 4.5(A) a sufficient alignment is not obtained and the SU-8 bonding layer is cross-linked in the following exposure step and sticks to the cantilevers. Figure 4.5(B) shows an image where this is prevented as the mask protects the cantilever region and the SU-8 cannot be cross-linked.

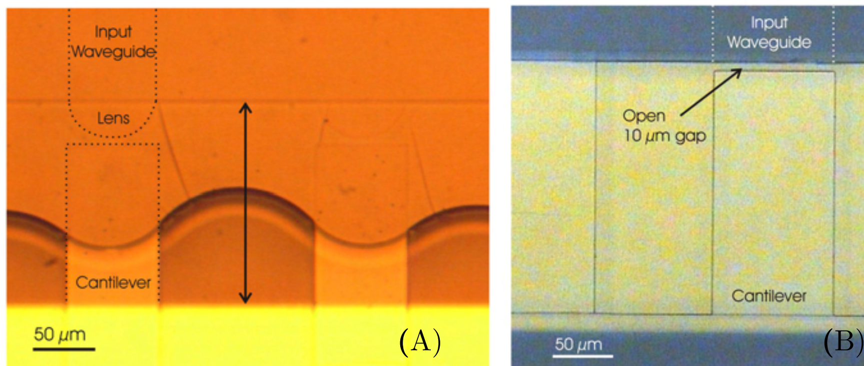

Figure 4.5: It is important to ensure that the pyrex wafer with the Cr/Au mask is aligned correctly to the structured chips. (A) With an off-alignment of the protective mask the cantilevers are stuck to the bonding layer. The black arrow indicates the misaligned regions. (B) With a correct alignment the gap between the input waveguide and the cantilever is resolved.

3. The wafers are separated with a scalpel and due to the low adhesion of the fluorocarbon coating the chips are transferred from wafer A to wafer B. The non-exposed SU-8, protected by the Cr/Au mask, is developed in PGMEA. The wafers have to be separated very gently to ensure that no mechanical damaging of the cantilevers is introduced. At this stage, the cantilevers are free-hanging. Figure 4.6 shows SEM images of a released chip where the cantilever is seen to be perfectly straight and aligned with the waveguide lens on the opposite side.

To obtain a high release yield of the chips from wafer A, it is crucial that a strong bond is obtained to all chips on the wafer. This stresses the importance of using the correct thickness of the SU-8 bonding layer on wafer B. Figure 4.7 shows two images of the cantilevers in the microchannel comparing two different thicknesses of the bonding layer. In figure 4.7(A) only a 1.6 µm thin bonding layer is used and it is clearly seen that contact is only obtained at the protruding waveguide region. Figure 4.7(B) shows the same region on the chip where a 5 µm thick layer of SU-8 is used. Here, close contact is obtained over the whole

region with some SU-8 even flowing into the channel. This situation ensures a tight seal between the two wafers.

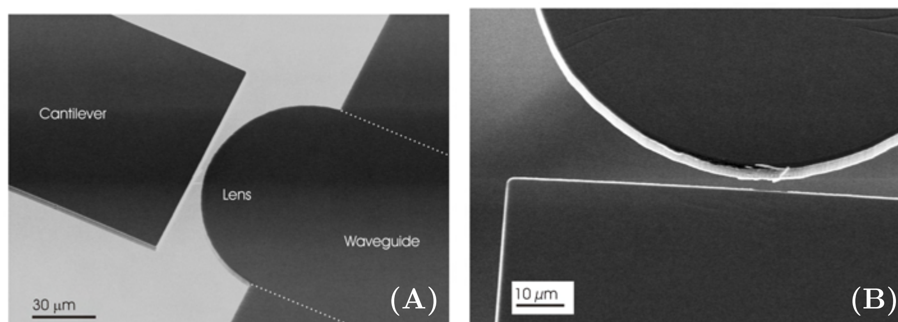

Figure 4.6: SEM images showing the cantilever and waveguide lens to be perfectly aligned after the release from the Si wafer. The gap between the two is only 5 µm. The different parts of the chip have been labelled for clarity. (A) The lens is protruding from the top cladding. (B) Zoom of the image in (A).

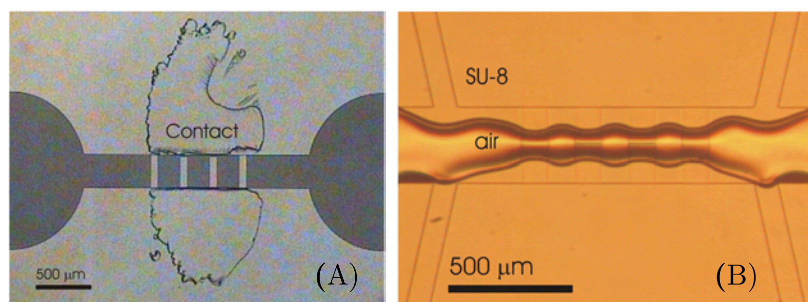

Figure 4.7: (A) When using only a 1.6 µm thin layer of SU-8 to bond the two wafers a sufficient seal is not obtained due to the height variation across wafer A. (B) A 5 µm thick SU-8 layer ensures close contact between the two wafers, with some SU-8 even flowing into the channel.

At this stage of the process free-hanging cantilevers with both input and output waveguides are fabricated and by using air as cladding the chips can be used for measurements. However, to enable integration of a liquid handling system a lower cladding layer is also required. The lower cladding is, like the top cladding, structured in the polymer mr-L. This layer defines the second half of the liquid channel at the cantilevers and provides a lower cladding for the input and output waveguides.

4. To obtain a lower cladding for the waveguides, wafer B with the chips is bonded to wafer C coated with mr-L. The bonding principle is the same as in step 1 but with a reduced contact force of only 100 N not to compress the mr-L layer and to avoid damaging the fragile cantilevers.

5. Afterwards, the wafers are taken out of the bonder and transferred to the mask aligner where the mr-L is exposed to UV light in flood-exposure mode. The integrated Cr/Au mask on wafer B protects the mr-L layer underneath the cantilevers from cross-linking. It is crucial that the Cr/Au mask on wafer B is perfectly aligned with the structures on wafer C as the lower cladding otherwise will cross-link and stick to the cantilevers.

6. After a PEB to cross-link the thick mr-L, the wafers are separated with the use of a scalpel and the non-exposed mr-L is developed in PGMEA. At this stage the processing of the chips is finished.

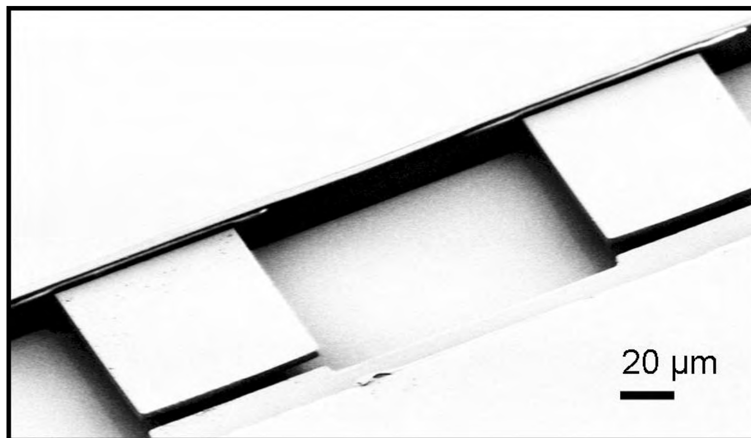

Figure 4.8: SEM image of a final chip. The cantilevers are free-hanging and perfectly straight. There has been a slight mis-alignment of the top cladding which leaves the input waveguides bare at the last part.

Figure 4.8 shows an SEM image of free-hanging cantilevers fabricated in the process described here. The total thickness of the structures is only 45 μm. It is therefore beneficial not to release them from the Pyrex wafer but to use this wafer as a support for further handling. The chips are sawn out of the Pyrex wafer to ensure that all waveguide facets are free for coupling of the input and output fibers.

It shall be noted that for the measurements the chips are turned upside-down with the Pyrex wafer facing the bottom. This means that what

is defined as top cladding during the fabrication is denoted *lower cladding* during the measurements described in Chapter 8 and the layer defined as lower cladding during the fabrication is denoted *top cladding*.

4.3 Further process investigations

The adhesion of the fluorocarbon film between the Si wafer and the two polymers is a critical parameter of the process described above; it must be sufficiently high to enable the Si wafer to act as a carrier wafer during the fabrication and it must be low enough to allow for the release of the structures as the final step. At one point during the project the properties of the fluorocarbon recipe changed and the adhesion improved drastically. This in turn meant that no structures could be released. A different recipe was then used but here the adhesion proved too low and the chips structured on wafer A fell off during the development step of the preparation of the individual wafers. No deposition recipe could be found with the desired adhesion. It is not understood why these changes occurred and it is outside the scope of this PhD thesis to investigate it. Therefore, two alternative process procedures were developed and investigated instead.

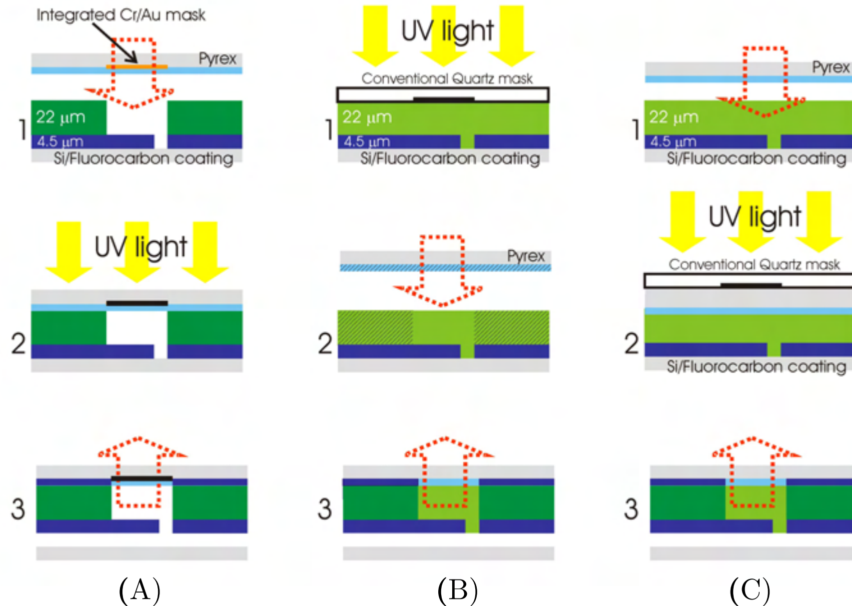

Figure 4.9: Alternative process sequences for the bonding of wafer A and B. (A) Standard process described in the previous section. (B) The chips and the SU-8 bonding layer are exposed before the bonding step. (C) The two wafers are bonded together before the exposure.

Figure 4.9 shows the different process sequences developed, where (A) shows the process described in the previous section to clarify the differences. Figure 4.9(B) shows the first approach investigated. Here, the cantilever waveguide layer is patterned on wafer A and mr-L is spin-coated on top and soft baked. Wafer B has a 5 µm thin layer of SU-8 spin-coated and soft baked on top but *no* integrated Cr/Au mask. To define the structures on wafer A a conventional quartz mask is used when exposing the wafer in a mask aligner. Wafer B is exposed in flood-exposure mode without a mask. Directly after the exposure step the two wafers are bonded together. No alignment of these wafers is required since there are no structures on wafer B. The same bonding protocol as described above in step 1 is used and the heating step during the bonding process is utilised as the PEB for cross-linking the two polymers. Afterwards, the wafers are taken out of the bonder and separated using a scalpel and the chips are transferred from wafer A to wafer B. After the release the non-exposed mr-L is developed. The release yield of this method proved to be very low, only around 20 %. The reason for this is because sufficient contact is not obtained between the two wafers during the bonding due to the edge bead on wafer A. Since the structures on wafer A are not developed before the bonding step the edge bead created during the spin-coating is still present. Moreover, it is speculated that the parts of the chip that cross-link during the bonding step expand slightly in the horizontal plane. This expansion in turn leads to a vertical movement of the non-exposed polymer towards the second wafer. The end result is that the full contact between the exposed chips and wafer B is prevented by the non-exposed polymer.

In the second approach, figure 4.9(C), the two wafers are bonded together first and exposed and cross-linked afterwards. On wafer A the cantilever waveguide layer is patterned and developed and the top cladding mr-L layer is spin-coated and soft baked. Wafer B has a 5 µm thin layer of SU-8 spin-coated but *no* integrated Cr/Au mask. The two wafers are bonded with the same bonding protocol as described in step 1 of the original process. After the bonding step both wafers are placed in a mask aligner and the mr-L is patterned using a conventional quartz mask by exposing through the Pyrex wafer. After the PEB the two wafers are separated with a scalpel and the non-exposed mr-L is developed in PGMEA.

This approach to fabricated the chips resulted in the same problem with insufficient contact between the wafers due to the edge bead on wafer A. The process yield is $\sim$ 20 %. Moreover, the edge definition is drastically reduced when the structures are defined by exposing through the Pyrex wafer. This is because the distance between the mask and the polymer film is increased to 700 µm. As a result, it is not possible to develop the 5 µm gap between the input waveguide and the cantilever when the structures are exposed through the Pyrex wafer. The 10 µm gap can still be developed though.

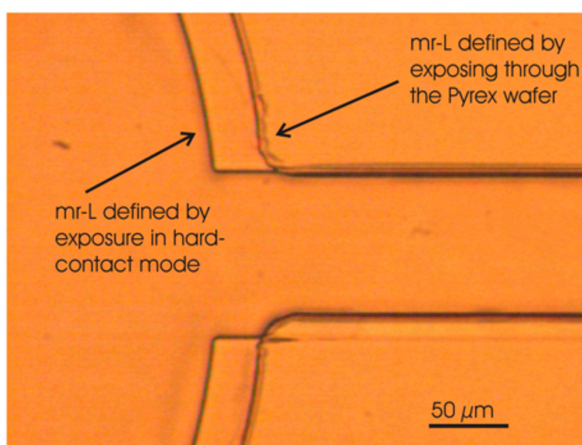

Figure 4.10: Comparison between a polymer layer exposed in hard contact mode or exposed through the Pyrex wafer. A conventional quartz mask is used in both cases. The edge definition is drastically decreased when exposing through the Pyrex wafer due to the increased distance between the mask and the polymer film.

Figure 4.10 shows a microscope image comparing a layer of mr-L exposed in hard contact mode and a second layer of mr-L exposed through the Pyrex wafer. The difference in edge definition is clearly seen. The modified fabrication processes described in figure 4.9(B) and (C) are possible alternatives to the initial process depicted in figure 4.9(A) but not ideal. The process yield should be possible to improve by performing an edge bead removal step before the bonding.

4.4 Release layer investigation

The fluorocarbon coating used as release layer for the chips was initially developed by Daniel Haefliger in the group and has been further investigated and optimised by Stephan Keller [102,103]. When the chips are released from the Si wafer characterstic marks are left on the wafer where the chip was placed, indicating that some of the fluorocarbon coating remains on the released cantilevers, figure 4.11.

To investigate this effect, AFM analysis of a chip is performed in tapping mode. A cantilever chip is scanned on both on the top side (processed in contact with air) and on the bottom side (processed in contact with the fluorocarbon film) and the topography of the two surfaces is compared. The AFM is scanned at the chip body and not at the cantilever to avoid any artifacts in the measurements from the bending of the SU-8 cantilever itself.

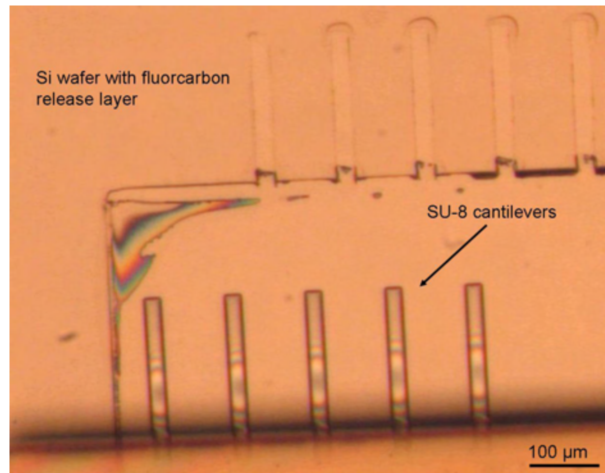

Figure 4.11: Marks on Si wafer after chip release. Most likely some of the fluorocarbon coating remains on the lower surface of the cantilevers.

The AFM scans are performed by Zachary Davies at MIC, DTU.

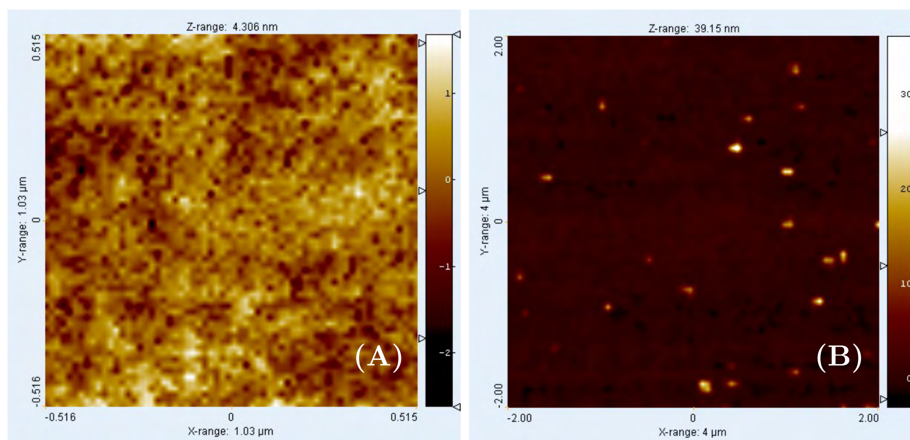

Figure 4.12: (A) 1 µm × 1 µm scan and (B) 5 µm × 5 µm scan on the air side of the chip. The bright spots in (B) are dust particles. The rms surface roughness of this surface is 0.5 nm.

Figure 4.12 shows two AFM scans of the SU-8 surface processed in contact with air. In figure 4.12(A) a 1 µm × 1 µm area is scanned and from this measurement the root-mean-square surface roughness of the SU-8 is found to be 0.5 nm and the peak-to-peak value is 4.3 nm. This surface can be considered smooth and no particular surface structure is seen. When zooming out and scanning a 5 µm × 5 µm area in figure 4.12(B), bright spots can

be seen. These are dust particles with an average height of 30 - 35 nm. The dust particles are there because the chips have been stored for a few months before the AFM scans are performed.

When scanning the surface processed in contact with the fluorocarbon film something very interesting is seen, the AFM scans are shown in figure 4.13. In the small 1 µm × 1 µm scan, the root-mean-square surface roughness is determined to be 1.2 nm and the peak-to-peak value is 8.3 nm. Both these values are considerably higher than for the SU-8 surface processed in contact with air. Moreover, when the scan area is increased to 5 µm × 5 µm a diamond like region is seen where the first 1 µm × 1 µm scan is performed. The height difference between these two areas is approximately 3.5 nm. From this observation it is speculated that some of the fluorocarbon film remains on the SU-8 cantilever chip when this is released from the Si wafer. What is seen in figure 4.13(B) is probably a compression or alternatively a removal of this remaining layer. The total thickness of the fluorocarbon coating cannot be determined since it cannot be ensured that the layer is completely removed. What can be said is only that its minimum thickness is 3.5 nm as measured. Moreover, in the AFM scans in figure 4.13(A) palette structures are seen. However, it is not possible to determine whether these are true structures on the SU-8 surface processed in contact with the fluorocarbon film or whether they are simply tip artifacts from the measurement.

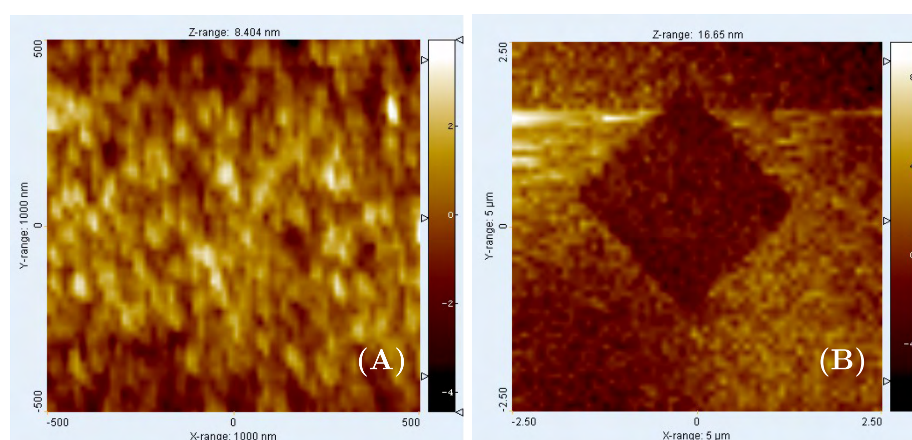

Figure 4.13: (A) 1 µm × 1 µm scan and (B) 5 µm × 5 µm scan on the fluorocarbon side of the chip. The rms surface roughness of this surface is 1.2 nm.

As discussed in Chapter 2 one of the fundamental requirements of a cantilever to be used as a sensor is that the chemical structure and/or the surface properties of the two cantilever faces are different. These AFM scans show

that the surface roughness of the two SU-8 surfaces differ significantly. From this observation it can be assumed that the two surfaces will react differently to the introduction of probe and analyte molecules. So there are advantages with the remaining fluorocarbon film (i) the layer is obtained during the processing (ii) the fluorocarbon remains ensure that the two cantilever surfaces are different (iii) its material properties are very similar to SU-8 which reduces drift and artifacts associated with the bi-material fabrication of the cantilever [104].

4.5 Summary

The new fabrication method of the system developed in this PhD project is discussed in this chapter. It is shown that free-hanging and well-aligned cantilevers with a thickness of 4.5 μm can be obtained in a direct fabrication process. The process sequence is optimised for the fabrication of embedded waveguides but it is also shown that the fabrication of a system with buried channel waveguides using air as top cladding can be fabricated.

Chapter 5

Read-out theory

This chapter discusses the theoretical approach used for analysing the sensitivity of the two different read-out methods. The work was initiated as a Desktop project with the students Christian Kallesøe, Christian Møller Pedersen and Thomas Pedersen [105]. The theory has then been further developed together with Fabien Amiot and Christian Flindt. The work shows that it is the reflection mode read-out that offers the highest sensitivity but to obtain this level of sensitivity the cantilever front-end must be coated with a reflective layer.

5.1 Overlap integrals

The intensity distribution of the fundamental mode can be modelled as a bell-shaped Gaussian function [57]. When analysing the sensitivities of the two different read-out modes *overlap integrals* between the wavefunctions in the different regions are used. This is simply a method to determine the degree of coupling of the light between the different regions, schematically shown in figure 5.1.

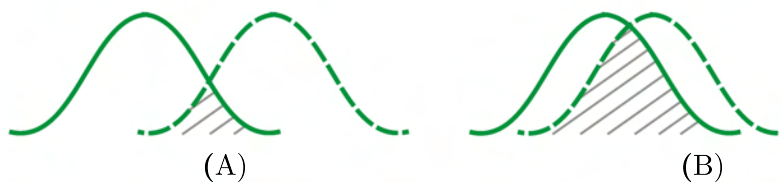

Figure 5.1: Schematic drawing of the principle of overlap integrals. (A) The overlap between these two modes is very low whereas the two modes in (B) show a good overlap. The resulting value of the overlap integral is called the *coupling efficiency* and it varies between 0 and 1 where 0 corresponds to no overlap at all.

Overlap integrals account for coupling losses due to mode mis-match as well as transverse and longitudinal off-set [105]. However, it does not account for is the change in the *amount* of back-reflected light reaching the input waveguide as a result of the change in the angle between the incident light and the cantilever front-end and the resulting change in direction of the back-reflected light. However, for a cantilever with a typical length of 200 μm and a deflection of 100 nm the angle will change from 0° (at zero deflection and considering only rays at perpendicular impact) to 0.06°, which is negligible. Therefore, the movement of the cantilever can be assumed as purely translative. The full theoretical approach on how to calculate the fundamental mode size to be used in the overlap integrals is found in Appendix C.

5.2 System layout

For the calculations the system is divided into five regions of different dimension and index step, shown in figure 5.2.

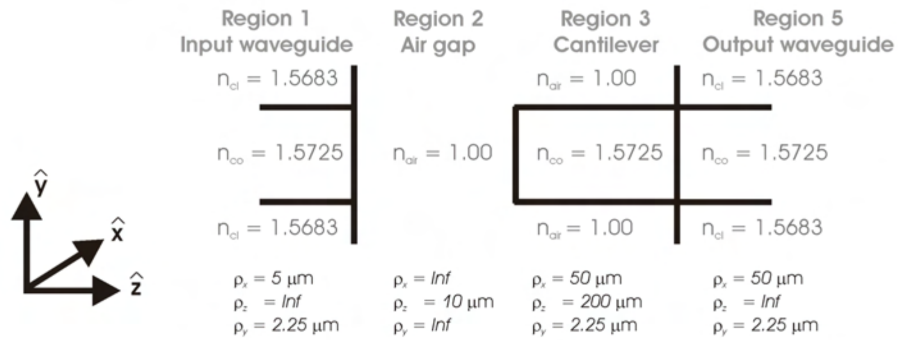

Figure 5.2: Cross-sectional view of the different optical regions the system is divided into. The air gap has a length l, always taken as 10 μm in these calculations. For clarity of presentation region 4 is not shown but it represents the light reflected in region 2. Here, the light enters into the chip from the left hand side. The denomination of the different regions is used throughout this chapter for the beam waists and the wavefunctions. The waveguides are assumed to be homogenous.

Region 1 corresponds to the 10 μm wide input waveguide and region 2 is the air gap between this waveguide and the cantilever. Region 3 is the cantilever, i.e. a waveguide suspended in air. Region 5 is the output waveguide connected to the cantilever. The width of the output waveguide is tapered down to 10 μm from the initial width of the waveguide. No losses are assumed to be introduced from this taper so the width of region 5 is determined by the width of the cantilever it is connected to, to give a correct value of

the overlap integral. The index step of region 5 is the same as for region 1. Finally, region 4 is the "imaginary" region of the reflected light. This has been assigned a separate region since the beam waist will differ compared to region 2 even though the dimensions and refractive indices are exactly the same. In region 2 and 4 the light is not confined in a waveguide structure and the beam waists develop in each direction as discussed in Chapter 2

$$w(l) = w_0 \left[1 + \left(\frac{\lambda l}{\pi w_0^2} \right)^2 \right]^{1/2}$$

where w_0 is the initial beam waist, λ is the free-space wavelength and l is the distance traveled [58].

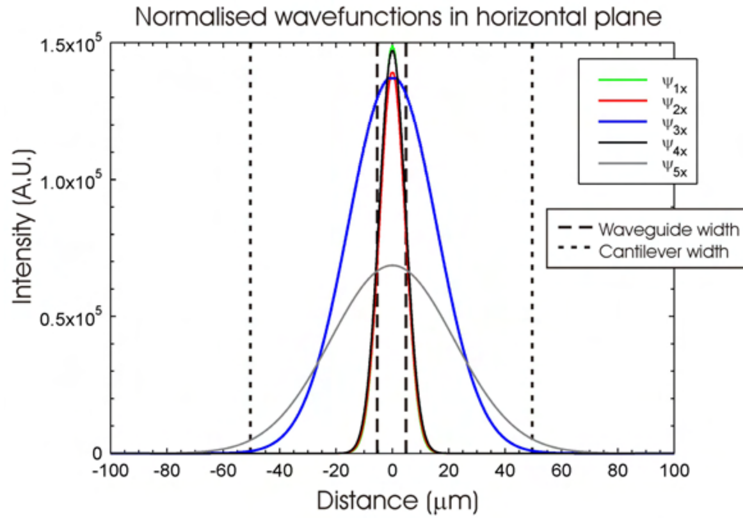

Figure 5.3: The normalised wavefunctions for the five different regions in the horizontal plane. ψ_{2x} and ψ_{4x} are plotted for $z = l = 10$ μm. The dotted lines show the dimensions of the waveguide cores. It shall be noted that the input waveguide is only 10 μm wide whereas the cantilever is 100 μm wide.

The wave functions in the different regions are plotted in figure 5.3 and 5.4. By comparing ψ_1 and ψ_2 it can be seen that ψ_2 does not spread very much in the gap as it approaches the cantilever but remains almost identical to ψ_1. This is most clearly seen in figure 5.4. Likewise, ψ_4 is also almost identical to ψ_1. Looking at figure 5.4 it is interesting to compare the confinements of the different wavefunctions. It is seen that it is only ψ_3 that is strictly confined to the core, due to the large index step between the cantilever core and the surrounding air. ψ_5 spreads almost as much as ψ_1 into the cladding layer.

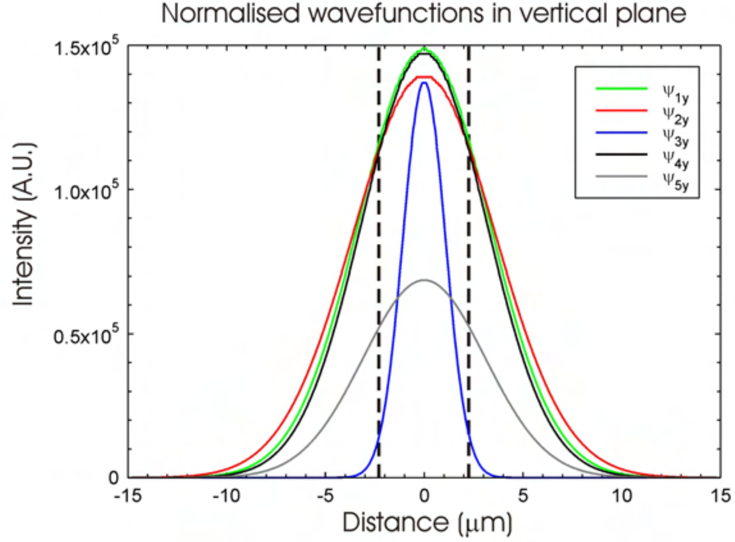

Figure 5.4: The normalised wavefunctions for the five different regions in the vertical plane. ψ_{2y} and ψ_{4y} are plotted for $z = l = 10$ μm. The dotted lines show the dimensions of the waveguide core.

5.3 Reflection mode

For the reflection mode read-out the light enters the system in the input waveguide (region 1) and travels across the air gap (region 2) to the cantilever. At the cantilever, the light is reflected (region 4) and couples back into the input waveguide (region 1) and exits the system. The refractive index and dimensions of region 4 are the same as for region 2 but the beam waists of the light differs. The coupling efficiency of the reflection mode, α_{ref} is found from computing the overlap integral of $\psi_2(x,y,l)$ & the cantilever front-end and $\psi_4(x,y,l,lb)$ & $\psi_1(x,y)$ at the cantilever/input waveguide interface

$$\alpha_{ref} = \alpha_{\psi_2/\text{cant}} \times \alpha_{\psi_4/\psi_1}$$

As the cantilever deflects the back-reflected light is shifted in the vertical axis. This shift leads to a decrease in the overlap between $\psi_4(x,y,l,lb)$ and $\psi_1(x,y)$ resulting in a decrease in the intensity signal of the returning light.

The full calculations are found in Appendix D with a final expression for α_{ref} as

$$\alpha_{ref} = \frac{\int_{-\rho_x wgin}^{\rho_x wgin} \int_{\theta_{min}}^{\theta_{max}} \psi_4(x, y + d_{slit}, l, lb)\psi_1(x, y)\ dxdy}{\int_{-\infty}^{\infty} \int_{-\infty}^{\infty} \psi_1^2(x, y)\ dxdy} \tag{5.1}$$

where $\rho_x wgin$ is the half width of the input waveguide, θ_{max} and θ_{min} are the integration limits for the returning light, d_{slit} is the center position of the deflected cantilever and l and lb both correspond to the distance between the cantilever and the input waveguide, taken as 10 µm.

5.4 Transmission mode

In the transmission mode, the light enters into the system via the input waveguide (region 1), travels through the air gap (region 2) and is coupled into the cantilever (region 3). Finally, the light couples into the output waveguide (region 5) and exits the system. If the cantilever bends less light will couple from region 2 into region 3.

The coupling efficiency of the transmission mode, α_{trans} is found from the overlap integrals of $\psi_2(x,y,l)$ & $\psi_3(x,y)$ at the air/cantilever interface and $\psi_3(x,y)$ & $\psi_5(x,y)$ at the cantilever/output waveguide interface

$$\alpha_{trans} = \alpha_{\psi_2/\psi_3} \ \times \ \alpha_{\psi_3/\psi_5}$$

The full calculations are found in Appendix D. α_{trans} is calculated as

$$\alpha_{trans} = \frac{\int_{-\infty}^{\infty} \int_{-\infty}^{\infty} \psi_2(x, y, l)\psi_3(x, y + d)\ dxdy}{\int_{-\infty}^{\infty} \int_{-\infty}^{\infty} \psi_1^2(x, y)\ dxdy} \times \\ \times \frac{\int_{-\rho_x wgout}^{\rho_x wgout} \int_{-\rho_y}^{\rho_y} \psi_3(x, y)\psi_5(x, y)\ dxdy}{\int_{-\rho_x cant}^{\rho_x cant} \int_{-\rho_y}^{\rho_y} \psi_3^2(x, y)\ dxdy} \tag{5.2}$$

where d is the cantilever deflection, $\rho_x wgout$ is the half width of the output waveguide, ρ_y is the half height of the cantilever waveguide layer and $\rho_x cant$ is the half width of the cantilever.

5.5 Theoretical output

Mathematica 5.1 (Wolfram Research, USA) is used for calculating α_{ref} and α_{trans} as described in the previous two sections. Using the values of the

refractive indices and dimensions from figure 5.2 the coupling efficiencies of the two modes are compared, figure 5.5. One assumption made in the calculations is that the integrals are only valid for a maximum cantilever deflection of ± 8.55 µm. These limits correspond to the region where the cantilever is fully illuminated. The calculated coupling efficiencies within this valid region are shown in figure 5.5(A).

For the situation of a 200 µm long cantilever this represents a surface stress range of almost ± 10 N/m which is well outside the range of typical biomolecular interactions [106]. Figure 5.5(B) shows the coupling efficiency within a cantilever deflection of ± 1 µm. By studying the plots three conclusions can be drawn:

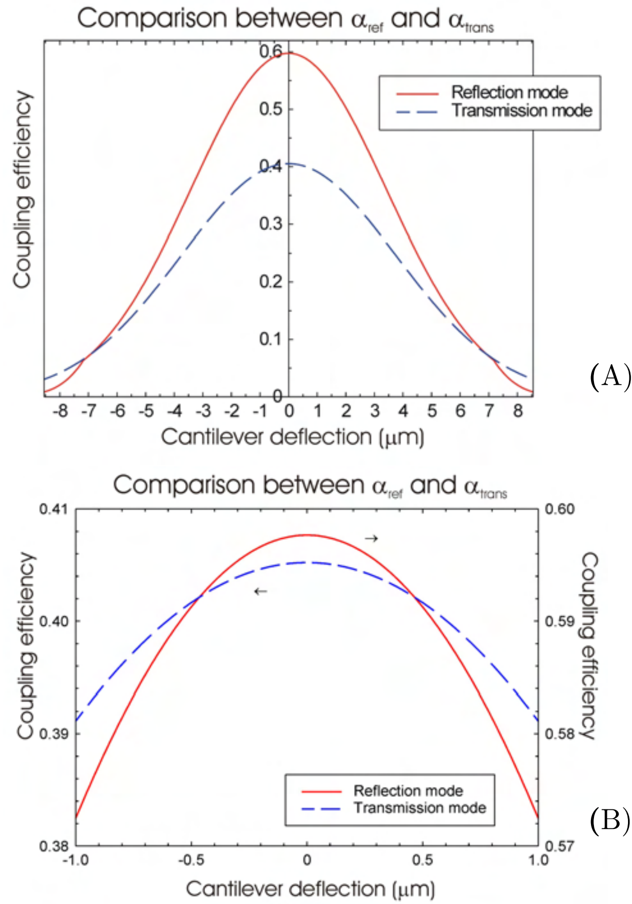

Figure 5.5: Comparison between the coupling efficiencies of the two read-out modes. The reflection mode has a higher coupling efficiency due to the better overlap of ψ_4 and ψ_1 compared to ψ_2 and ψ_3 for the transmission mode. (A) Cantilever deflection of ± 8.55 µm. (B) Zoom of a cantilever deflection of ± 1 µm.

1. At zero deflection of the cantilever, the reflection mode read-out corresponds to a higher coupling efficiency than the transmission mode read-out. The values are 0.598 and 0.406 respectively. This is because of the better overlap between the back-reflected light $\psi_4(x,y,l,lb)$ and the mode in the input waveguide $\psi_1(x,y)$ compared to the wavefunction of the light reaching the cantilever $\psi_2(x,y,l)$ and of the light inside the cantilever $\psi_3(x,y)$.

2. The sensitivity of the reflection mode is slightly higher than of the transmission mode. This is most clearly seen in the $\pm$ 1 µm deflection plot, figure 5.5(B) where the slope of the reflection mode read-out is steeper than the slope of the transmission mode read-out. In the steepest region the coupling efficiency in the reflection mode varies as 0.036 μm^{-1} and the corresponding value for the transmission mode coupling efficiency is 0.016 μm^{-1}. Both values are given for a negative cantilever deflection.

3. Both read-out modes have their *lowest sensitivity* close to the zero deflection point of the cantilever. This is of great disadvantage since the aim is to monitor minimal cantilever deflections. The reason for the low sensitivity in this region is the centering of the fundamental mode in the waveguides assumed in the calculations.

From the conclusions of the theoretical output it is seen that optimal sensitivity is not obtained with perfectly homogeneous waveguides. What is required to greatly increase the sensitivity of both read-out modes is to shift the intensity distribution of the light $\sim$ 3 µm in the vertical plane. This can be obtained practically by using two different cladding materials with a large refractive index difference. As seen in Chapter 3 the refractive indices of the mr-L used as top cladding is different compared with the mr-L used as bottom cladding due to the extra process steps this layer is subjected to. The resulting effect on the modes is studied in Chapter 6.

For the calculations of α_{ref} and α_{trans} the cantilever front-end is assumed 100 % reflective in the reflection mode and 100 % transmissive in the transmission mode. This is naturally not true and the Fresnel reflections at the medium interfaces need to be accounted for, as discussed in Chapter 2 [56]. Equation (2.3) determines the amount of back-reflected light for rays of perpendicular impact, R_{Fres}.

In the reflection mode drop in the optical power is seen when the light exits the input waveguide. At the cantilever front-end only a small amount of the light is reflected back and when this light couples back into the input waveguide the optical power drops again due to the Fresnel reflections.

P_{out} in the reflection mode is therefore calculated as

$$P_{out} = P_{in} \times R_{Fres} \times (1 - R_{Fres})^2 \times \alpha_{ref}$$

For the transmission mode read-out some of the optical power is lost as the light exits the input waveguide and as the light couples into the cantilever. This results in P_{out} in the transmission mode calculated as

$$P_{out} = P_{in} \times (1 - R_{Fres})^2 \times \alpha_{trans}$$

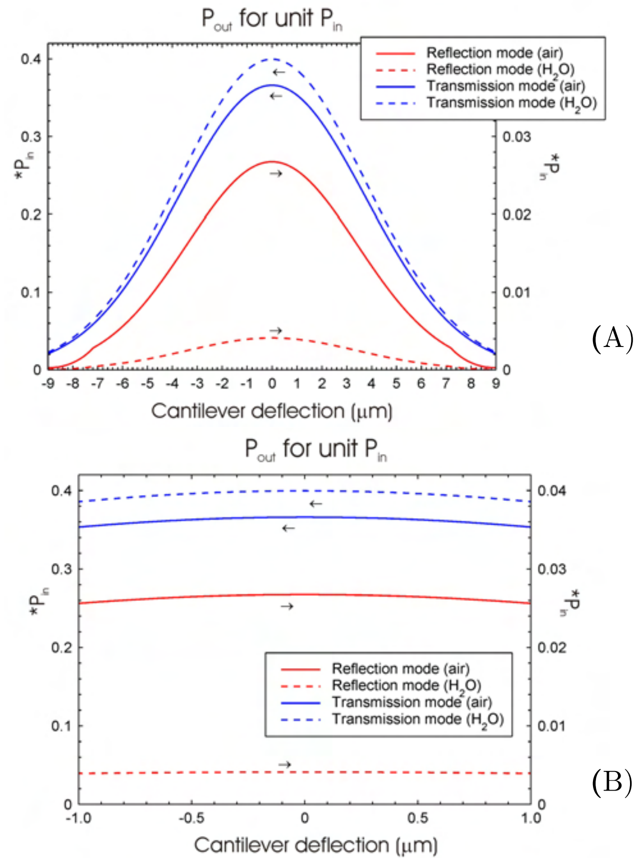

Figure 5.6: Comparison between the optical out-put of the two read-out modes when the gap between the input waveguide and the cantilever is either filled with air or a buffer solution. For the latter situation, the output from the reflection mode is seen not to be sufficient.

Taking the medium of the gap between the input waveguide and cantilever to be air with a $n_2 = 1$ the value of R_{Fres} is 4.5 %. However, the aim of the system developed in this work is to be used as a bio/chemical sensor and such analyses are usually performed in buffer solution. For this situation, the expression of R_{Fres} is modified with $n_2 = 1.33$ and the Fresnel reflections only correspond to 0.69 %. The corresponding intensity levels of the two read-out modes are presented in figure 5.6. From the plot it is seen that the intensity of the transmission mode is increased from 37 % to 40 % of P_{in} when the microchannel is filled with a buffer solution instead of air whereas the intensity output of the reflection mode is greatly reduced. In fact, the intensity level of the back-reflected light is only 0.41 % of P_{in} when the system is operated in liquid compared to 2.5 % of P_{in} when the system is operated in air.

One way to significantly improve the read-out of the reflection mode is to coat the cantilever front-end with a a reflective material, such as a thin layer of Au. Assuming that the side-walls of the SU-8 are not too rough to introduce critical scattering, a 30 nm layer of Au will ensure close to 100 % reflectivity of the cantilever front-end [107]. Such a situation modifies the expression for P_{out} in the reflection mode to be

$$P_{out} = P_{in} \times (1 - R_{Fres})^2 \times \alpha_{ref}$$

Figure 5.7 compares the optical power output from the two different read-out modes when the medium between the input waveguide and the cantilever is a buffer solution.

As expected, the reflection mode is seen to out-perform the transmission mode if the cantilever is coated with a reflective layer. It shall be noted that the plot for the transmission mode is for the situation of a bare SU-8 cantilever. The expected value of P_{out} for the three different situations are 0.59, 0.40 and 0.0041 times P_{in} respectively. No devices with this type of reflective coating have been fabricated in this project. All operations of the system fabricated in this work are carried out in air. To calculate the minimum detectable signal expected from the two read-out modes the values of P_{out} from figure 5.6 are used and the value of P_{in} is taken as 20 μW. The resulting read-outs are plotted in figure 5.8.

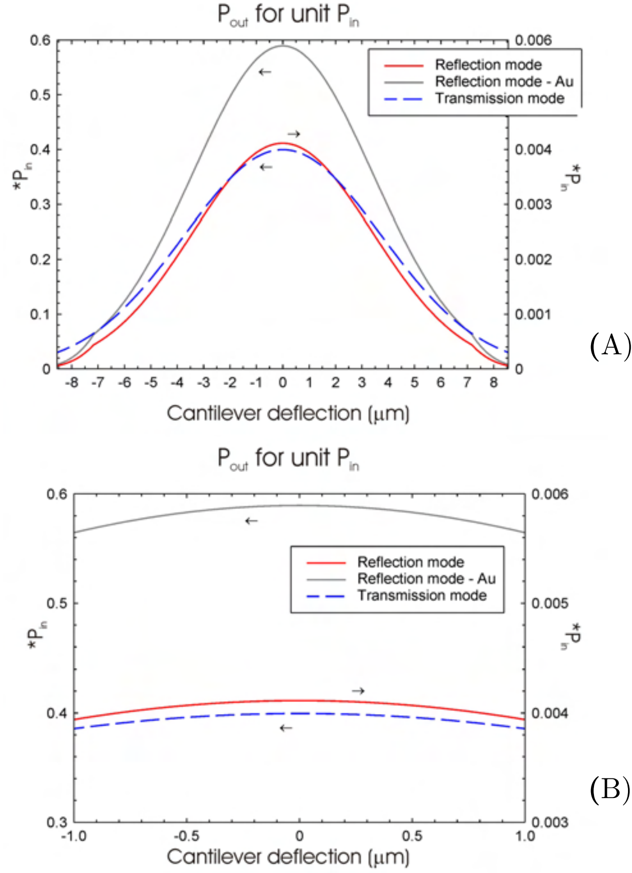

Figure 5.7: Comparison between the optical out-put of the two read-out modes both where the front-end of the cantilever is pure SU-8 and where it is coated with a reflective Au layer. For the latter situation, the reflection mode is seen to out-perform the transmission mode. The gap between the input waveguide and cantilever is taken to be filled with a buffer solution of n = 1.33.

Using a conservative noise level estimate of ± 5 nW for both read-out modes the minimum detectable cantilever deflection is calculated as 300 nm for the reflection mode and 30 nm for the transmission mode if the cantilever is operated in the region of the steepest slope. If the situation of perfect alignment between the cantilever and the input waveguide is considered instead, the values are significantly increased due to the nature of the Gaussian beam in this region. For this situation a minimum deflection of 640 nm in the reflection mode and 160 nm in the transmission mode is required for an intensity change of 0.01 μW. The sensitivity of the reflection mode is decreased drastically because of the low signal-to-noise ratio and the assumption that the noise levels are equal. Chapter 8 discusses the results from the characterisation of the read-out modes of the fabricated chips.

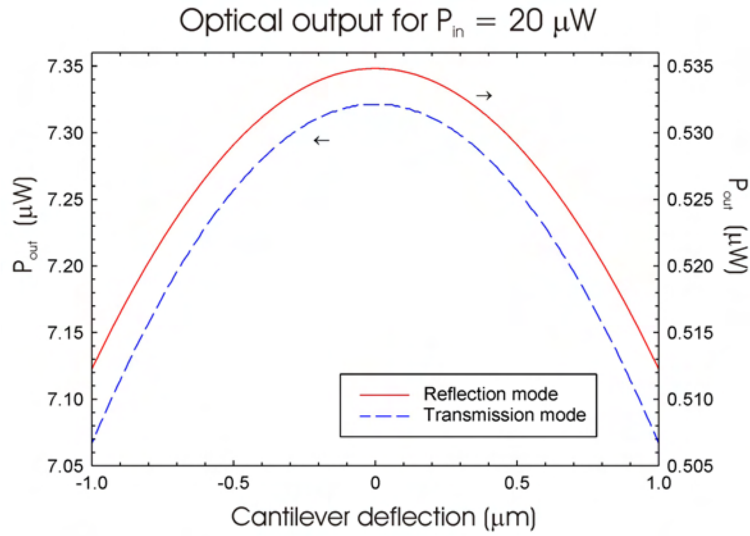

Figure 5.8: Theoretical calculation on the read-out sensitivities for both modes. The value of P_{in} is taken as 20 µW, which is the measured value from fiber-to-fiber. The medium between the input waveguide and cantilever is air with n = 1.

5.6 Summary

This chapter shows the theoretical approach for calculating the read-out sensitivity of the two different modes of operation. It is shown that the reflection mode has a higher coupling efficiency than the transmission mode but that the optical output and thereby the signal-to-noise ratio of the transmission mode is higher. The sensitivity of the reflection mode can be significantly improved by the addition of an extra process step to coat the cantilever front-end with a reflective material. The calculated minimum detectable cantilever deflection is 30 nm in the transmission mode read-out and 300 nm in the reflection mode read-out.

Chapter 6

Waveguide characterisation

The material SU-8 used for the fabrication of the waveguides in this system has previously been presented together with other cladding materials than mr-L [70,76,78,108–111]. The combination of SU-8 as core material and mr-L as cladding material has been presented for the fabrication of multi mode waveguides by M. Karppinen *et al.* and Immonen *et al.* [112, 113]. Single-mode waveguides with this material combination have not been reported before. This chapter discusses the different experiments performed to analyse the optical properties of these waveguides, such as the propagation and coupling loss, mode profiles and spectral absorption.

6.1 Set-up

All equipment is placed on an optical table (90 cm × 150 cm, Thorlabs, USA). A 635 nm laser diode and a 20X lens with a 0.35 numerical aperture are used to facilitate the alignment of the fibers to the sample by projecting the waveguide output facet onto the wall while optimising the input fiber position. Single-mode fibers with 9-µm-diameter core and 125-µm-diameter cladding (Corning, USA) are used for butt-coupling the light in and out of the sample. All fibers have FC connectors at the opposite end for easy exchange of light sources and detectors. The numerical aperture of the fibre is 0.13 [9]. The fibers are cleaned with ethanol and prepared with a fiber cleaver (EFC11, Ericsson, Sweden) before being placed on custom-made fiber holders and secured with magnets. The fiber holders are placed on x-y-z-stages (NanoMax-TS, MellesGriot, USA). For some measurements index-matching oil (Immersionsoel, n = 1.5180) is used. For the cut-back measurements at 635 nm and 1 535 nm the red light diode and a lightwave multimeter (Agilent 8163A, Agilent Technologies, USA) with a 81662A laser unit are used as light sources. For detection a lightwave multimeter (HP 8153A, Hewlett Packard, USA) with two different detector units: HP 81530A (450 - 1 200 nm) and HP 81532A (800 - 1 700 nm) is used. For cut-back

measurements over the spectral range 800 - 1 700 nm a white light source (AQ-4303B, Ando, Japan) and a spectrum analyser (HP 86140A, Hewlett Packard, USA) are used. A CCD camera (XCD-X710, Sony, Japan) is used during the investigations of the mode profiles where the 635 nm light is focused onto the CCD camera with the 20X lens. The images are captured and analysed with ImageTool (Image Tool, UTHSCSA). The set-up is seen in figure 6.1 below.

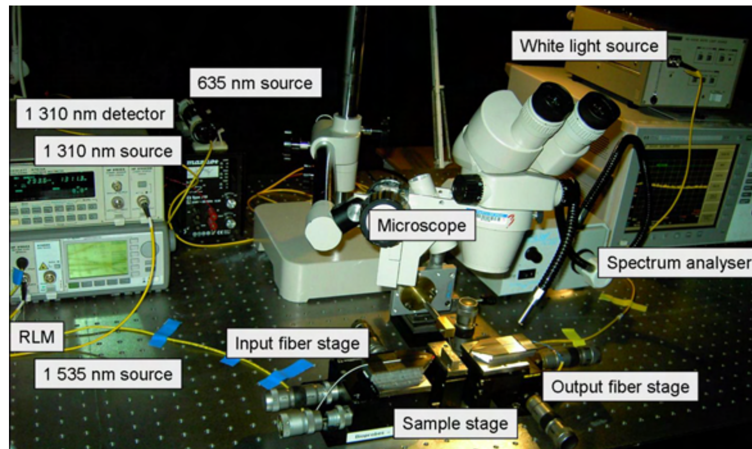

Figure 6.1: All equipment used for the optical characterisation of the waveguides. A microscope is used for viewing the sample during the alignment of the fibers. Here, the RLM unit used in Chapter 8 is also seen.

6.2 Propagation loss

For the investigation of the propagation loss of the waveguides, embedded waveguides of different widths: 3, 5 and 10 µm are fabricated. The Si substrate is prepared with a 3 µm thick thermally grown SiO_2 buffer layer to prevent substrate leakage. The waveguides are structured with mr-L as both bottom and top cladding (22 µm thick) and the wafer is cleaved to different lengths by scribing on the backside of the Si wafer. The propagation loss of the waveguides is determined via the *cut-back method* where the loss of the waveguide is measured as the length of the waveguide is cut-back from 80 mm to 22 mm. By plotting the data, both the propagation loss and the coupling loss of the waveguides can easily be calculated. In this thesis, the coupling loss is always stated *per facet* so the total coupling loss of the waveguide is twice that value since each waveguide has two facets. As a first step the wavelengths of 635 nm and 1 535 nm are investigated and the data is plotted in figure 6.2.

From the graphs it is seen that both the propagation loss and the coupling loss are very high for all waveguides, both at 635 nm and 1 535 nm. At 635 nm the 3 μm wide waveguide shows a lower propagation loss, 2.7 dB/cm and a lower coupling loss, 5.5 dB/facet compared to the 5 μm wide waveguide that has a propagation loss of 2.8 dB/cm and a coupling loss of 6.5 dB/facet.

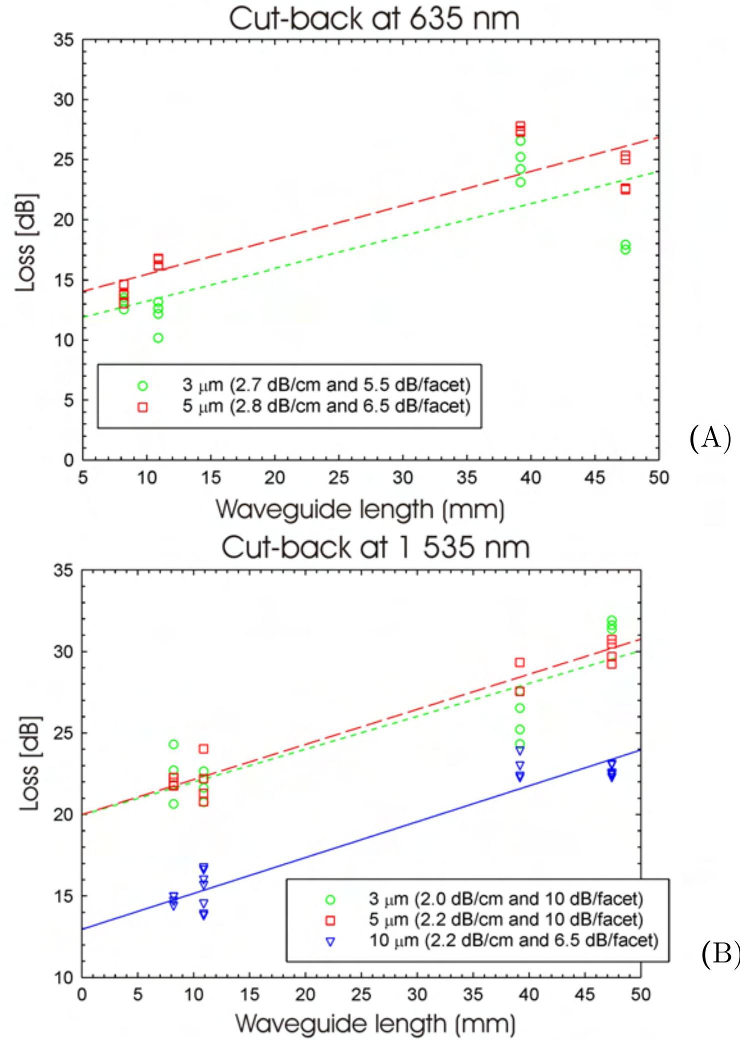

Figure 6.2: (A) Cut-back measurements at 635 nm show a propagation loss for these waveguides of $\sim$ 3 dB/cm. The coupling loss is very high, over 5 dB/facet. (B) At 1 535 nm these waveguides show a propagation loss of $\sim$ 2 dB/cm. The coupling loss is extremely high at this wavelength, over 10 dB/facet for the 3 and 5 μm wide waveguides and 6.5 dB/facet for the 10 μm wide waveguide.

At 1 535 nm the 3 and 5 µm wide waveguides show approximately the same values; propagation loss of ∼ 2 dB/cm and coupling loss of 10 dB/facet. The 10 µm wide waveguide has the same propagation loss, 2 dB/cm but a considerably lower coupling loss of only 6.5 dB/facet due to the greater overlap between the fiber mode and the waveguide mode. Since the 10 µm wide waveguide has the lowest coupling loss, all waveguides in the final system are fabricated with this width. Nevertheless, the propagation and coupling losses are not acceptable and the experiment is repeated over the spectral range 800 - 1 700 nm to find a more suitable wavelength of operation. The resulting data is shown in figure 6.3 and 6.4. Here, the same type of samples processed under identical conditions are used for the analysis and measurements are performed on four samples that are 88, 78, 58 and 20 mm long. The propagation and coupling losses are calculated by the *principle of least squares* [114]. The different peaks of the data are attributed to absorption of vibrational energy of the materials. This is discussed in detail in Chapter 3.

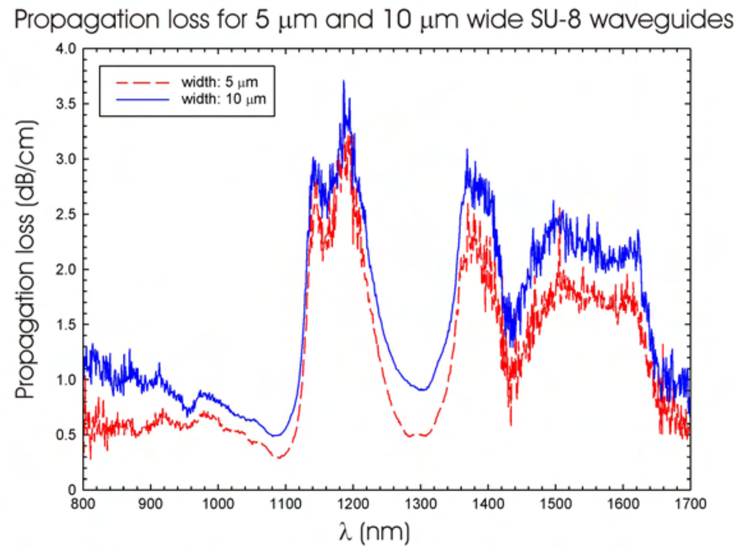

Figure 6.3: Propagation loss of a 5 µm and a 10 µm wide waveguide over the spectral range 800 - 1 700 nm. The waveguides are best operated at 1 100 nm and 1 300 nm where they show the lowest propagation loss. The peaks are due to vibrational absorption of the molecular bonds of the SU-8 material, as discussed in Chapter 3.

From figure 6.3 it can be seen that the wavelength regions 1 090 ± 10 nm and 1 300 ± 20 nm are much better suited for operation of these waveguides. The propagation loss in the first region is only 0.6 dB/cm and the value is the second region is ∼ 1 dB/cm. Both values are given for a 10 µm wide waveg-

uide. The data in figure 6.4 shows that the coupling losses are 2 dB/facet and 0.25 dB/facet at these regions respectively. Since the input and output waveguides in the final cantilever sensing system have a total length of only 1.65 cm it is easily concluded that it is more important to operate at a wavelength with a low coupling loss. In this wavelength region laser diodes are readily available at 1 310 nm which therefore is chosen as the wavelength of operation of this system. These findings also stress the importance to design the waveguides with a width of 10 µm to ensure a good modal overlap between the butt-coupled fibers and the waveguides [90].

From the measurements of the coupling losses across the spectral range a significant absorption peak at 1 450 nm is seen. This peak is commonly associated with absorptions of H_2O [94]. When the samples used here are sawn out the saw blade is cooled under a stream of water that also washes the complete sample. It is speculated that some of this water is absorbed into the polymers and that some of the water is adsorbed onto the waveguide facet. However, to generate a loss of 6 dB at one facet, the gap between the fiber and the input waveguide needs to be 1 mm and completely filled with liquid water [115]. This is naturally not the situation and it is therefore very difficult to explain the presence and significance of this absorption peak.

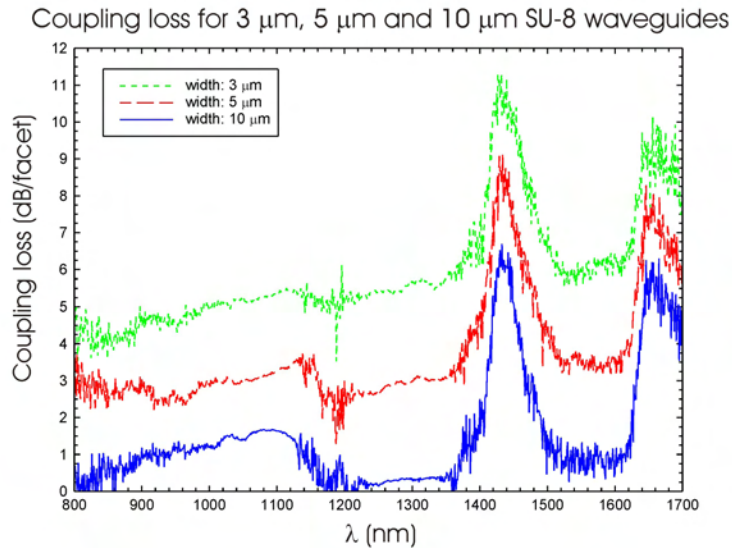

Figure 6.4: Coupling loss of a 3, 5 and 10 µm wide waveguide. The coupling loss is considerably lower for the 10 µm waveguide compared to the 3 µm wide waveguide due to the better mode overlap with the 9-µm-diameter input fibre. The absorption peak at 1 450 nm might be attributed to adsorbed water on the waveguide facets.

Facet quality

The extremely high coupling losses of up to 10 dB/facet seen in figure 6.2 are not acceptable. When repeating the experiment with index-matching gel between the input fibre and the waveguide no significant improvement is seen. However, when the measurement is repeated over the whole spectral range in figure 6.4 the losses are significantly reduced. The explanation is that the samples used in figure 6.2 are cleaved whereas the sample in figure 6.4 is sawn. Figure 6.5 shows SEM images clearly presenting the difference in facet quality.

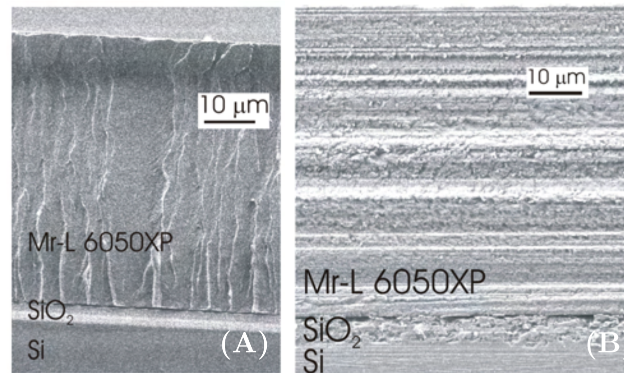

Figure 6.5: SEM images showing a cleaved (A) and a sawn (B) facet. It is clearly seen that the sawn facet is much smoother than the cleaved facet. The waveguide core structure cannot be seen due to the small index contrast between the two materials.

To obtain a clear cut in a Si wafer, best result is obtained if the wafer is scribed on the backside and cleaved so that the wafer splits along the crystal lines. However, since both mr-L and SU-8 are far from crystalline materials the same results are not obtained for these structures. This is clearly seen in figure 6.5 where SEM images of a cleaved (A) and a sawn (B) facet are compared. Figure 6.6 compares the results from cut-back measurements with a cleaved sample (black circles) and a sawn sample (open circles). It is seen that the propagation loss is the same for both samples but the coupling loss is reduced by over 5 dB/facet when the sample is sawn.

6.3 Mode profiles

The mode profiles of the waveguides are studied to ensure that only single-mode propagation occurs and to investigate the vertical position of the mode. 635 nm light is coupled into the waveguide and the exiting light is focused onto a CCD camera with a 20X lens. For calibration of the CCD camera an image of the whole system facet is taken. The thickness of the system is

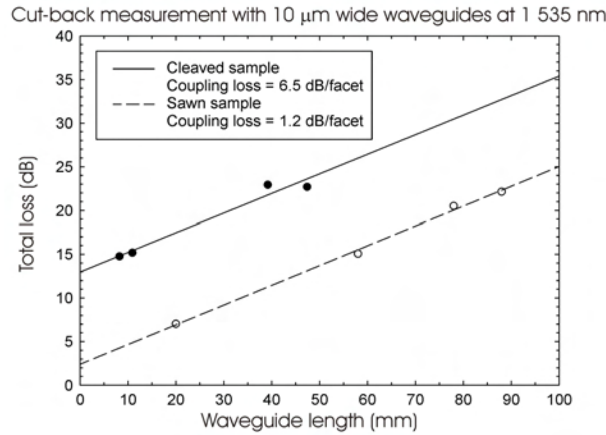

Figure 6.6: Much lower coupling loss is obtained when the sample is sawn compared to cleaved. A reduction of over 5 dB/facet is seen. The propagation loss is the same for both types of samples clearly showing that it is the cleaving method that is the cause of the great coupling loss.

known and the conversion between distance and number of pixels is straightforward. The accuracy of the measurements is ± 1 μm with this method. For these measurements only straight waveguides with a thickness of 4.5 μm are used. For light propagating inside a waveguide the *mode field diameter* (MFD) is used to define its modal width as discussed in Chapter 2 where figure 2.2 shows the definition schematically. The measured values are compared with the calculated values from Chapter 5 where a Gaussian mode profile of the waveguides is assumed, figure 5.3 and 5.4. The different types of waveguides studied are presented in figure 2.1 in Chapter 2.

Figure 6.7 shows the mode profiles of a 10 μm wide embedded waveguide, which is the same as the input waveguide used in the final system. In the horizontal direction the mode profile is completely symmetric with a MFD of 9.0 μm. In the vertical direction the MFD is 6.6 μm. It can also be seen that the mode is not symmetric around the core in the vertical direction. As discussed in Chapter 3 the processing affects the value of the final refractive index of the polymers. Here, the lower cladding layer is subjected to three exposures and six different baking steps whereas the top cladding is only exposed once and baked twice. This means that the index step between the core and the lower cladding is slightly higher compared to the index step between the core and the top cladding and a slight shift of the mode is expected. However, since the difference in refractive index step is so small the light is still seen to be centered in the waveguide and it is only the penetration depths into the two claddings that differ.

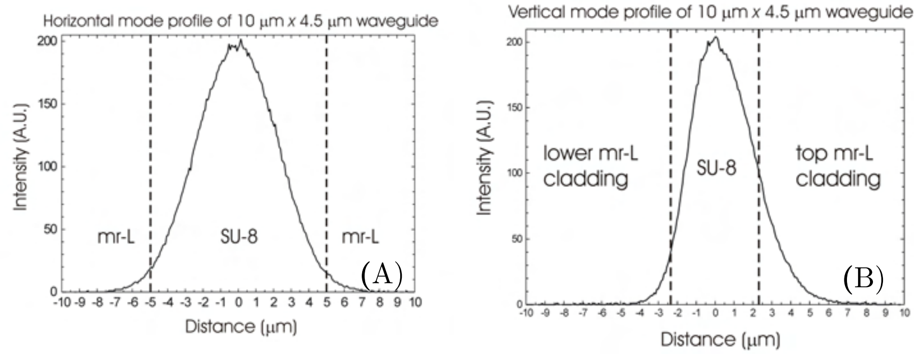

Figure 6.7: Mode profile of 10 μm embedded SU-8 waveguide. (A) Horizontal mode profile of the input waveguide with a measured MFD of 9.0 μm. (B) The vertical mode profile shows a shift towards the top mr-L cladding of the waveguide mode. The MFD is 6.6 μm.

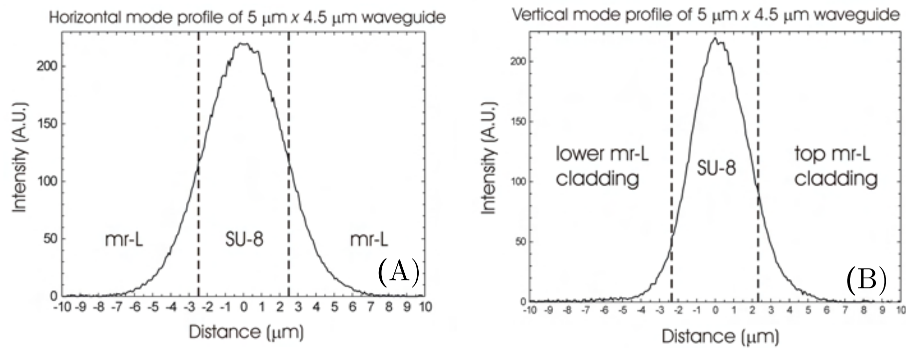

Figure 6.8: Mode profile of 5 μm embedded SU-8 waveguide. (A) Horizontal mode profile with a measured MFD of 8.7 μm. (B) The vertical mode profile shows a shift towards the top mr-L cladding of the mode profile due to the slight difference in the refractive indices of the claddings from the processing. The MFD is measured as 6.2 μm.

The mode profiles of a 5 μm wide embedded waveguide is observed and compared with simulation data of the same waveguide type performed with FiMMWAVE (Photon Design, UK). Figure 6.8 shows the measured mode profiles. In the horizontal direction the mode profile is symmetric with a MFD of 8.7 μm. Like for the 10 μm wide waveguide the vertical mode profile is asymmetric with a MFD of 6.2 μm. Figure 6.9 shows the simulation output where the mode profile of the 5 μm wide waveguide is modelled. Even though the index step between the core and the top cladding is different from the index step between the core and the lower cladding the mode is still centered

in the waveguide and no vertical shift is seen. This is probably because the difference in index step is only in the order of 10^{-3}. To obtain a significant shift of the maximum intensity peak of the mode a larger index step is required.

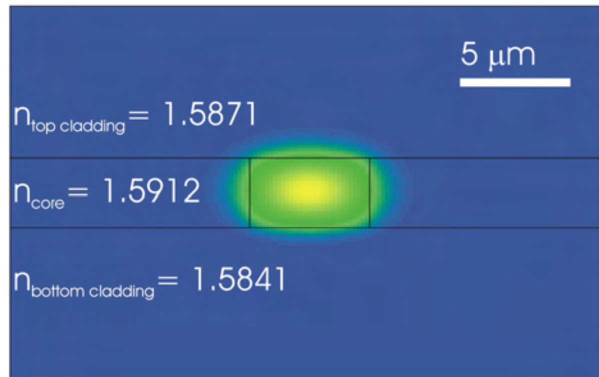

Figure 6.9: Simulation output of the mode distribution of an asymmetric waveguide. No shift of the mode profile is seen but the field penetrates considerably deeper into the top cladding than the bottom cladding. This is also observed from the mode profiles of the waveguide samples.

Figure 6.10 shows the calculated value of the MFD of the light travelling inside the waveguide and the initial beam waist (w_0) of the light exiting the waveguide as the width of the waveguide is varied. The calculations are performed for embedded waveguides at a wavelength of 1 310 nm. The height of the waveguide is 4.5 µm. From the plot it can be seen that a waveguide that is 5 µm wide has an expected MFD of 15.8 µm and a 10 µm wide waveguide has an expected MFD of 16.8 µm. The values do not compare very well with the measured values (8.7 µm and 9.0 µm respectively) but the graph does show that the difference in the MFD between a 5 µm wide waveguide and a 10 µm wide waveguide is marginal, like the measurements also show. The reason for the discrepancy between the calculated and measured values is a combination of the uncertainty in the refractive indices of the core and cladding layers, the fact that the calculations are performed for symmetric waveguides and the uncertainty in the experimental procedure to measure the MFDs. Moreover, the simulations are not limited by excitation from a single-mode fiber, which is the situation for the real samples.

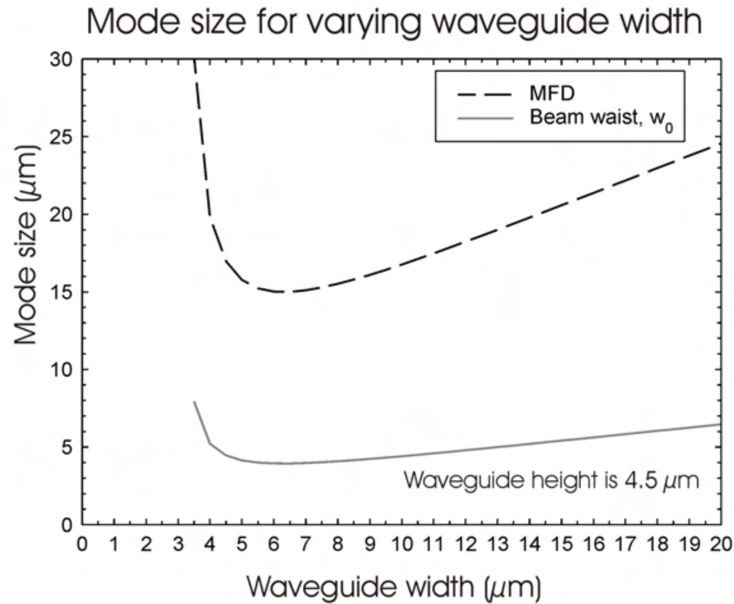

Figure 6.10: Mode size in the horizontal plane with varying waveguide widths calculated for symmetric embedded waveguides with an index step of 0.0042. The height of the waveguide is 4.5 μm. There is no significant difference in the MFD between a waveguide that is 5 μm wide or 10 μm wide. For a waveguide width less than 3.5 μm the value of the beam waist goes to infinity and is therefore not plotted.

Figure 6.11 shows the horizontal (A) and vertical (B) mode profiles of a 10 μm wide rib waveguide structured on a mr-L lower cladding. It is clearly seen that no light propagates in the air and that a shift of the mode profile of ∼ 1 μm is obtained in the vertical direction. The MFD in the horizontal direction is 7.7 μm. MFD is 5.6 μm. The calculated values of the MFD's for this waveguide structure is 7.9 μm in the horizontal direction and 4.1 μm in the vertical direction. It is interesting to note that the calculated values for the horizontal direction compare much better with the measured values for the rib waveguide than for the embedded waveguides. This is because the mode is confined strictly to the core and the value of the refractive index of the cladding is fully known in the latter structure.

Another interesting observation of the rib waveguide is the importance of the alignment of the input fiber. Due to the larger index step between the core and the surrounding air, this waveguide supports further modes than only the fundamental mode. Figure 6.11(A) shows two plots of the mode profile of the 10 μm wide waveguide. The contour seen in grey is the optical output if the input fiber is not aligned perfectly at the center of the

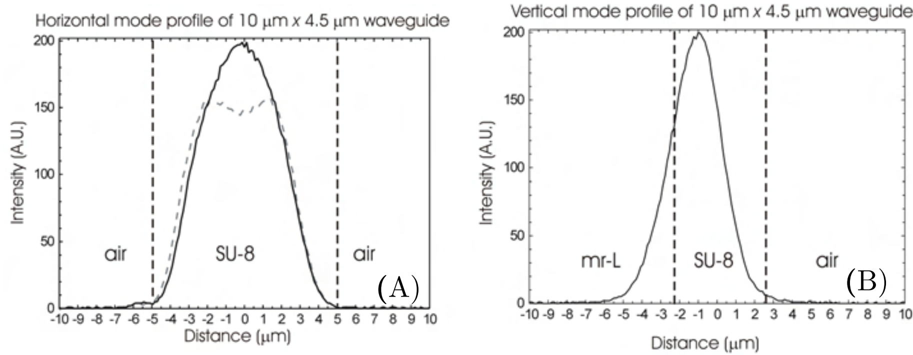

Figure 6.11: Mode profile of 10 μm rib SU-8 waveguide. (A) Horizontal mode profile with a MFD of 7.7 μm. The grey dotted line shows the excitation of the first order mode if the input fiber is not perfectly centered. (B) The vertical mode profile shows a shift towards the lower mr-L cladding since it cannot propagate in the air. The measured MFD 5.6 μm.

waveguide. In this situation the first order mode is excited instead of the fundamental mode due to the symmetry of the different modes. However, if the fiber is moved into the center of the waveguide, only the fundamental mode is excited. This stresses the importance of aligning the fibers correctly with the waveguides.

6.4 Summary

This chapter discussed the characterisation of the optical properties of the waveguides fabricated with the novel material combination using SU-8 as core and mr-L as cladding. It is seen that the best operating wavelength is 1 310 nm. At this wavelength the propagation and coupling losses have values of 1 dB/cm and 0.25 dB/facet respectively for a 10 μm wide and 4.5 μm high waveguide. Hagerhorst *et al.* present single-mode SU-8 waveguides with a propagation loss of only 0.3 dB/cm at 1 300 nm, which is significantly lower than the value measured here. The waveguides fabricated by Hagerhorst *et al.* are SU-8 rib waveguides structured on a SiO_2 buffer layer [70]. Embedded single-mode SU-8 waveguides are presented by Tung *et al.* where NOA16 is used as top cladding. These waveguides are also structured on a SiO_2 buffer layer and the propagation loss obtained is 1.25 dB/cm at a wavelength of 1 550 nm [78]. This value is also lower than what is measured in this work. However, neither these structures nor the structures presented by Hagerhorst *et al.* allow for the definition of a free-hanging waveguide layer.

In this chapter it is also seen that the best facet quality is obtained by sawing the samples out since these waveguides are not fabricated in crystalline materials and therefore do not cleave well. The mode profiles are studied in order to ensure that only single-mode excitation occurs and to investigate any shifts in the position of the maximum intensity of the mode in the vertical direction. It is seen that all waveguides only support the fundamental mode as long as the input fiber is aligned perfectly with the waveguide. It is also seen that the MFD of the 5 μm embedded waveguide is the same, within the experimental uncertainty, as for the 10 μm wide waveguide. This shows that the waveguides are truly in the *weak guidance approximation*. Moreover, it is seen that the sensitivity of the read-out should be improved by using a buried channel waveguide with air as top cladding for input waveguide in the system as this results in a mode shift of ~ 1 μm downwards.

Chapter 7

Cantilever characterisation

This chapter presents mechanical characterisation of the cantilever structures alone. The measurements are performed by Montserrat Calleja at IMM-CSIC in Madrid, Spain. The cantilevers are fabricated at MIC, DTU. The resonance frequency is measured to find the value of the spring constant of the cantilevers. Moreover, a comparative experiment is performed with a SU-8 cantilever and a commercial Si_3N_4 cantilever where the improved sensitivity, due to the lower Young's modulus of the SU-8, is shown.

7.1 Cantilever fabrication

These cantilevers are fabricated at MIC following the process described in Chapter 3 and the exact process sequence is found in Appendix E. It shall be noted that there are *no waveguides* structured in these cantilevers.

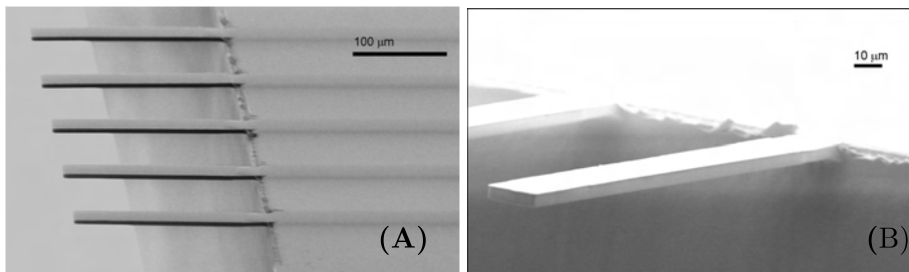

Figure 7.1: (A) An array of five released cantilevers on a chip. (B) Each cantilever is seen to be perfectly straight. The thickness of these cantilevers is 4.5 µm.

The cantilevers are structured with a thickness of 4.5 µm and after development they are released from the Si wafer by simply lifting with a pair of tweezers. Figure 7.1 shows SEM images of a released chip with 20 µm wide cantilevers that are 200 µm long.

On some chips an interesting observation can be made; there seems to be a small bend in the cantilever at the point of clamping, figure 7.2(A). The origin of this shape is not fully understood but it is probably caused at the stage of the cross-linking of the support layer. When this thick layer cross-links the stresses generated start to pull on the under-lying cantilever layer. Due to the low adhesion of the fluorocarbon layer, the cantilevers might start to lift at the point of clamping and become fixed in this shape during the following PEB. However, looking at a whole chip with 15 cantilevers, figure 7.1(B), their apices are seen to be well aligned even though most cantilevers show this small bend at their clamping. It has not been investigated how this might affect the bending profile of the cantilever upon surface stress changes and the propagation of the light through the cantilever but this is of course important to understand. The reason why this has not been studied is that this bend does not appear on all chips but has only been observed on a few.

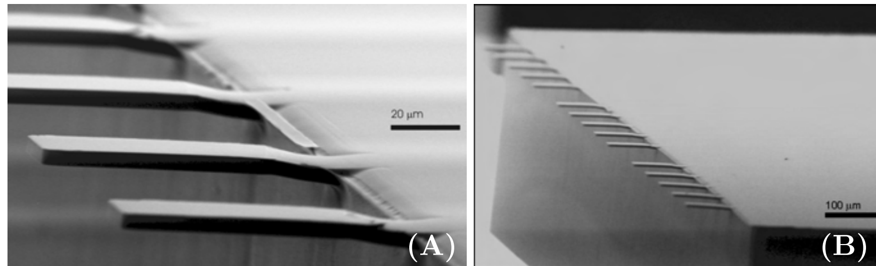

Figure 7.2: (A) Some cantilevers show a small bending at the point of clamping. (B) However, this does not seem to affect the overall alignment of the cantilever apices.

7.2 Resonance frequency and spring constant

The mechanical properties of the cantilevers are studied by measuring the resonance frequency in air and liquid (water). The theoretical expression for the resonance frequency is

$$f_{res} = \frac{1}{2\pi}\sqrt{\frac{k}{m^{\star}}}$$

where k is the spring constant and $m^{\star}$ is the effective mass of the cantilever [116]. The effective mass is calculated as the mass of the cantilever combined with the mass of any surrounding fluid the cantilever is forced to move during the vibrations.

Figure 7.3 shows the resonance frequency of a 4.5 µm thick, 20 µm wide and 200 µm long cantilever measured as 43 kHz in air and 15 kHz in liquid.

The reduced frequency in liquid is because of the increased effective mass of the cantilever. The resonance frequency of a 1.5 μm thick, 20 μm wide and 200 μm long cantilever is also measured, both in air and liquid. The valus of the resonance frequency are found to be 17 kHz and 3.4 kHz in air and liquid respectively.

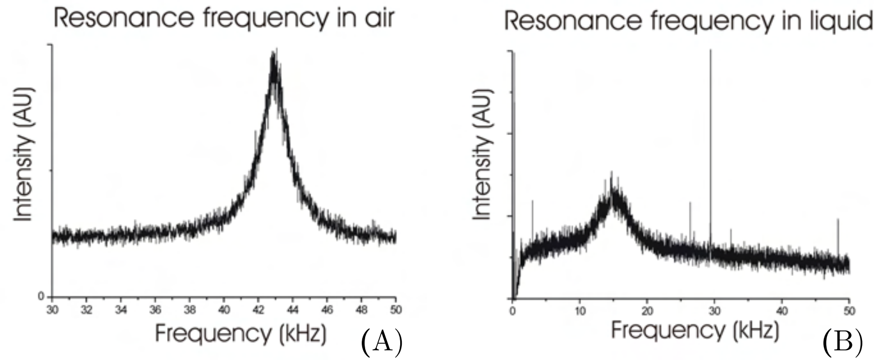

Figure 7.3: The resonance frequency of a 4.5 μm thick, 20 μm wide and 200 μm long cantilever is 43 kHz in air but only 15 kHz in liquid due to the increased effective mass of the cantilever when it is submerged in a fluid with a greater density.

From the resonance frequency measurements the spring constant can be calculated and the values are found to be 1.58 N/m for the 4.5 μm thick cantilever and 0.088 N/m for the 1.5 μm thick cantilever, taking the density of SU-8 to be 1 200 kg/m^3 [117] and assuming that the effect of the air on the effective mass is negligible.

7.3 Cantilever sensitivity

As discussed in Chapter 2 cantilevers react to temperature fluctuations and pH changes of the surrounding medium due to the bi-material structure. Montserrat Calleja has performed a thorough study on the effect of small changes in both temperature and pH that typically arise in a bio/chemial assay. These experiments have been published in *Applied Physics Letters* [104]. In another experiment, the sensitivity of two different cantilever types are compared [118]. The SU-8 cantilever used in this experiment is 1.6 μm thin and coated with a 10 nm layer of Au to enable the same chemistry on both cantilevers for an accurate comparison. The reference cantilever is a 800 nm thin commercial Si_3N_4 cantilever (Olympus, Japan) that is also coated with a 10 nm layer of Au. Both cantilever are 20 μm wide and 200 μm long. 20 ml of 2 μM ss-DNA followed by 20 ml of 1 mM MCH (mercapto-hexanol) is introduced to the liquid cell where the cantilevers are situated and their respective bendings are monitored.

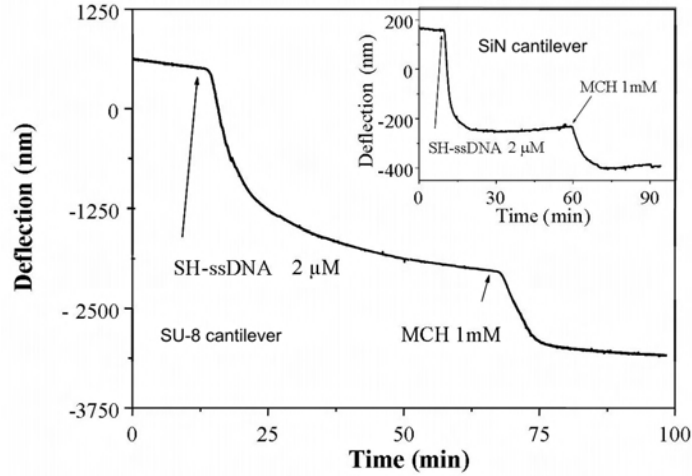

Figure 7.4: The SU-8 cantilever shows a six times greater bending (2 500 nm) compared to the Si_3N_4 cantilever (400 nm) shown in the inset, when the DNA is introduced.

The theoretical expression for cantilever deflection, Δd, in relation to an applied surface stress, $\Delta\sigma$, is defined in Chapter 2 as

$$\Delta d = \frac{3(1-\nu)l^2}{Et^2}\Delta\sigma$$

where ν and E are the Poisson's ratio and Young's modulus of the cantilever material respectively and t and l is the thickness and the length of the cantilever respectively.

The Young's modulus of SU-8 is 4.95 GPa [119] and the value for Si_3N_4 is 200 GPa [120]. Substituting for the material properties and the dimensions of the cantilevers and assuming that the same surface stress is generated on both cantilevers, it can be seen that the SU-8 cantilever is expected to bend ten times more than the Si_3N_4 cantilever even though this cantilever is twice as thick as the Si_3N_4 cantilever. From the measurement it is seen that the SU-8 cantilever bends six times more than the commercial cantilever. The measured value compares well with the calculated value and the small discrepancy between the two is most likely due to inhomogeneities of the 10 nm Au layer and the probe density on the cantilevers. Another source of error are uncertainties in the dimensions of the cantilevers. It is due to the softer properties of the SU-8 material that this cantilever shows superior surface stress sensitivity to the Si_3N_4 cantilever. By decreasing the thickness of the SU-8 cantilever further improvements of the sensitivity is expected. A

further advantage with the SU-8 cantilevers is that they are less susceptible to noise from variations in temperature and pH [104].

7.4 Summary

The SU-8 cantilevers fabricated here are shown to offer higher surface stress sensitivity and to be less affected by noise factors such as temperature fluctuations or pH changes in the measurement liquids compared to conventional Si_3N_4 cantilevers [104,118]. This is a consequence both of the material properties and the specific fabrication method where a fluorocarbon film is used as the release layer.

Chapter 8

System characterisation

This chapter describes the characterisation of the optical read-out methods performed on the final fabricated system. By mechanically deflecting the probe a known distance the optical intensity variations are monitored in both the reflection mode and the transmission mode. The aim of the measurements is to show proof-of-principle, which is successfully done for both read-out modes. Necessary improvements of the calibration method is also discussed.

8.1 Set-up

The set-up for the calibration of the read-out modes uses the same optical fibers and mechanical parts as described in Chapter 6. The light source is a 1 310 nm laser unit (HP 81552SM, Hewlett Packard, USA) mounted in the HP 8153A lightwave multimeter. The Agilent 8163A lightwave multimeter holds one return loss meter (RLM) (HP 81534A, Hewlett Packard, USA) used to detect the back-reflected light from the cantilever and one photodetector (HP 81532A, Hewlett Packard, USA).

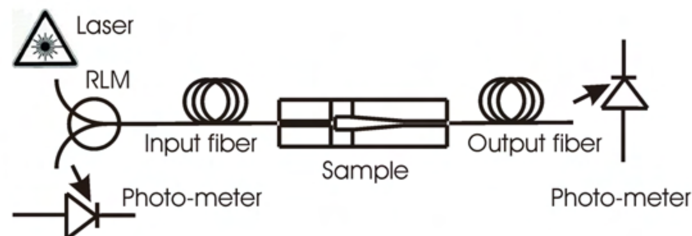

Figure 8.1: Schematic image of the set-up for the calibration of the system. The 1 310 nm laser is coupled via the RLM detector for operation both in transmission and reflection mode.

The set-up is shown schematically in figure 8.1. The 1 310 nm light source is coupled into the RLM that is mounted in channel A in the Agilent 8163A lightwave multimeter. The light is butt-coupled into the system from the RLM via a single-mode fiber. The read-out from the RLM corresponds to the read-out of the reflection mode. Another single-mode fiber is butt-coupled to the output waveguide of the system and connected to the HP 81532A module mounted in channel B of the lightwave multimeter. This unit gives the read-out from the transmission mode. Data recording occurs with LabView (National Instruments, USA) from both channels simultaneously on a PC the lightwave multimeter is connected to via a GPIB interface. The sampling rate is 1 s.

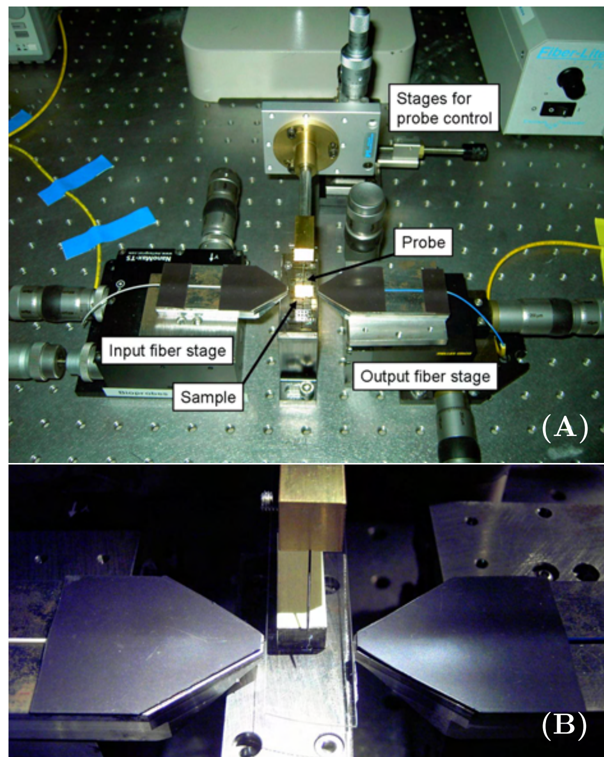

Figure 8.2: The set-up used for the calibration of the system. (A) The probe is used to control the cantilever deflection while the optical output from the reflection mode and the transmission mode is monitored. (B) Zoom of the probe and the sample with the input fiber on the left-hand-side and the output fiber on the right-hand-side.

To characterise and calibrate the two read-out modes a set-up is assembled where a tungsten probe (9111-09, Terra Universal, USA) is used to mechanically deflect the cantilever while the optical output from the two

read-out modes is monitored. The tip radius of the probe is 25 μm. Figure 8.2 shows a picture of the set-up. Two stages (M-461, Newport, USA) make up the lower region of the set-up and these are used to control the position of the probe in the horizontal plane. A 5 cm long metal rod is secured onto a third stage of the same type mounted vertically on the two lower stages. At the end of the rod the probe is fastened at an 45 ° angle to the rod. The vertical displacement of the probe is controlled with a micrometer screw (DM-13B, Newport, USA) to an accuracy of ± 0.25 μm. For the following measurements it is assumed that the tip of the probe moves with the same displacement as the micrometer screw. The probe is place at the apex of the cantilever and therefore the displacement of the cantilever is assumed to be identical to the movement of the micrometer screw. This assumption is valid due to the rigidity of the set-up and the softness of the cantilever. Obviously, the range of displacements generated by the probe does not reflect the expected cantilever deflections generated by any real bio/chemical analyses. The aim of these experiments is purely proof-of-principle.

Alignment procedure

The input fiber is directly spliced onto the RLM. This means that simple alignment with red light where the light source is exchanged afterwards is not possible because sufficient power cannot pass through the RLM at 635 nm. Therefore, a six-step-alignment procedure is used:

1. The 635 nm laser diode is connected via a freshly cleaved fiber and aligned to the input waveguide of the system by focusing the output light with the 20X lens onto the CCD camera.

2. The lens and CCD camera are moved and a freshly cleaved output fiber is connected to the red light detector and aligned to the output waveguide of the system. At this stage the input fiber shall not be moved.

3. The input fiber is exchanged to the fiber from the RLM module that is first freshly cleaved. The 1 310 nm light is connected via the RLM.

4. The output fiber is changed from the red light detector to the infra red light detector.

5. The input fiber from the RLM is aligned to the input waveguide of the system. At this stage the output fiber shall not be moved.

6. Final fine adjustments of the two fibers is performed to ensure optimal alignment.

8.2 Light propagation

The first investigation that is performed on the complete system is a comparison between the mode profile of the input waveguide and the mode profile exiting the system.

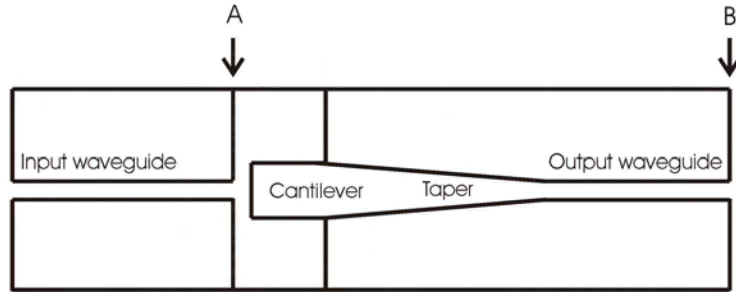

Figure 8.3: Schematic drawing marking the two different cross-sectional planes in the system where the mode profiles are compared. **A** marks the input waveguide and **B** marks the output waveguide.

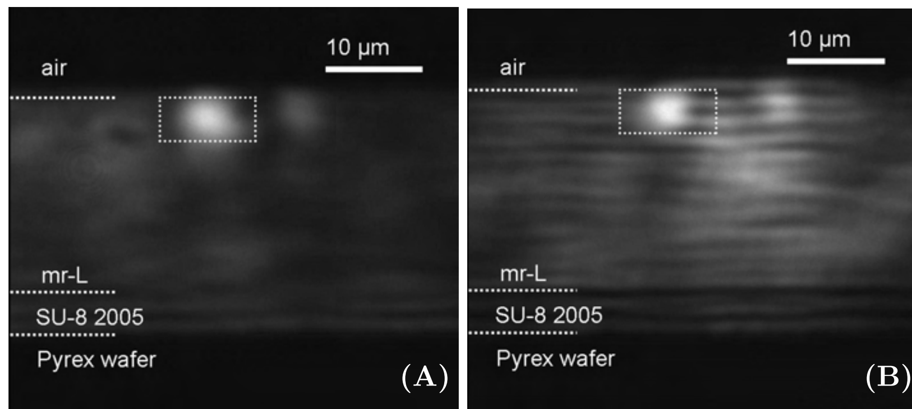

Figure 8.4: CCD images comparing the output light from (A) a 10 µm wide straight buried waveguide and from (B) the output waveguide of the system. The waveguide cores and the different regions are marked for clarity.

For this study a system with air as top cladding is used. The input waveguide is a 10 µm wide and 4.5 µm high channel waveguide. The output waveguide starts with a 75 µm wide and 100 µm long cantilever suspended in air and continues with a channel waveguide that is tapered down to 10 µm at the end of the chip. Figure 8.3 marks the cross-sectional planes where the two mode profiles are observed. **A** marks the input waveguide and **B** marks the output waveguide.

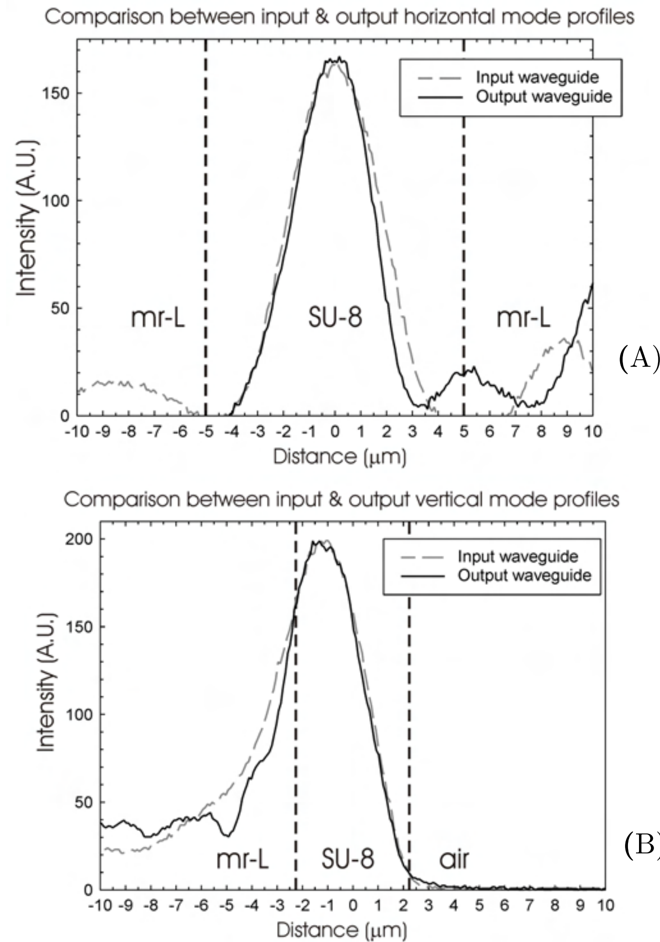

Figure 8.5: Comparison between the mode profile of the input and output waveguides. (A) The MFD of the input waveguides is 7.7 μm and the output waveguide measures 5.8 μm in the horizontal direction. (B) The MFD of the input waveguides in the vertical direction is 8.0 μm and the output waveguides measures 5.0 μm. No significant change in the MFD of the light occurs as it travels across the system.

The mode profile from the input waveguide is obtained by aligning the fiber to one of the 10 μm wide straight reference waveguides that are structured at the outer region of the chip. An image of the output light is captured by the CCD, figure 8.4(A). For the mode profile of the light exiting the system the fiber is aligned to a cantilever waveguide in the same chip. The CCD image of this mode is shown in figure 8.4(B). The waveguide cores and facet regions are marked in both images for clarity. From the images in figure 8.4 it can be seen that some light travels in the cladding of the system. The cladding modes are due to bad facet quality that prevents 100 %

coupling of the light into the waveguide core. However, it is still easy to see the waveguide structure and that most of the light is centered at the waveguide core. Figure 8.5 compares the intensity profiles of the light exiting the input waveguide and the output waveguide. Both the horizontal and vertical profiles are shown. The mode profile of the input waveguide is shown in light grey and the mode profile of the output waveguide is represented by the black curve. From figure 8.5 it can be seen that only single-mode propagation occurs in both waveguides in both the horizontal and the vertical direction. It can be noted that the MFD in both the vertical and horizontal directions are slightly smaller for the output waveguide compared to in the input waveguide. However, the difference is well within the experimental error of this type of measurement and it is concluded that no significant change in the MFD occurs as the light travels across the system.

8.3 Transmission mode

To characterise the transmission mode read-out the tungsten probe is placed at the apex of the cantilever without touching it. The probe is moved in 1 μm steps in 3 min time intervals. The system is given 3 min for stabilisation of the output signal between the different inputs. Figure 8.6 shows the read-out of a typical measurement in the transmission mode.

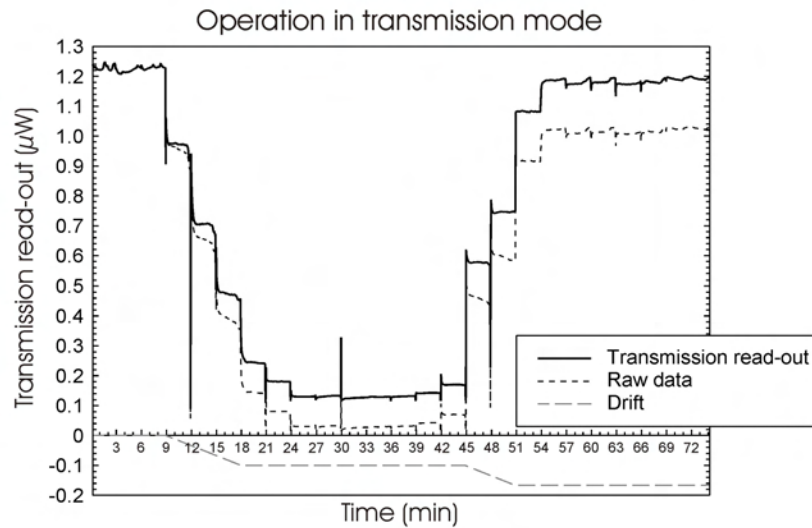

Figure 8.6: Typical data obtained for the transmission mode read-out when the probe is placed at the apex of the cantilever and deflects the cantilever in 1 μm steps. The maximum deflection here is 9 μm.

Both the raw data, the drift and the resulting output signal are plotted. The drift in the measurement is represented by the slope of the light grey plot. The drift is calculated from the linear 3 min intervals and it is assumed the drift stems from the drift of the micrometer screw and the stages holding the input and output fibers. It is not possible to exactly determine when the probe first touches the cantilever by observation in the microscope. Therefore, the probe is brought in contact with the chip and then lifted ~ 3 μm upwards before the measurement is started. The point of contact is then determined from the measurement data afterwards. This naturally adds a degree of uncertainty to the measurement. From the data output it can be approximated that the probe is placed 2 μm above the cantilever initially. The probe is moved downwards a total of 9 μm and between 30 min and 36 min on the time line in figure 8.6 the probe is maintained at this maximum displacement. Afterwards, the probe is returned to its initial position in 1 μm steps. As the probe deflects the cantilever the intensity of the throughput light is decreased and as the cantilever is moved back to its original position the output light level is returned almost to its initial value. There is a small discrepancy of -0.02 μW between the initial and the final values of the intensity level. This difference is well within experimental errors. Another interesting observation is that the intensity of the light never reaches zero but 100 nW light can always pass through the system as stray light outside the waveguides.

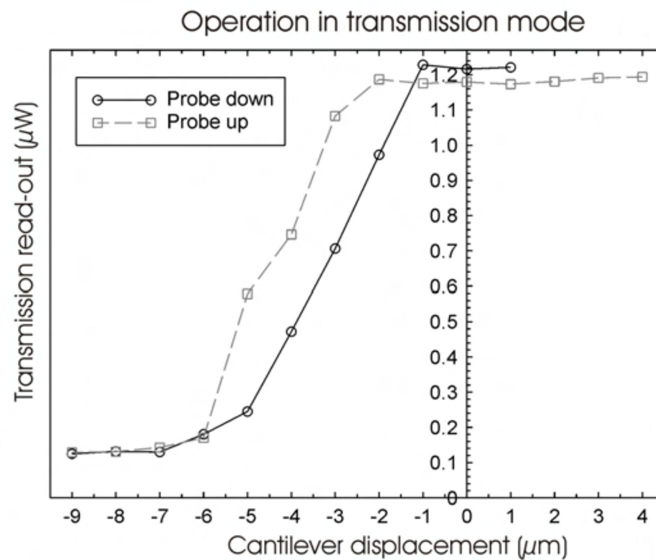

Figure 8.7: Measurement output for the transmission mode read-out where the optical intensity is plotted versus the cantilever deflection. The error bars in the measurement are the same size as the data points.

Figure 8.7 shows the optical output intensity for the different cantilever displacements as measured in figure 8.6 both as the probe is moved downwards (black circles) and upwards again (grey squares). The data points are connected for guidance of the eye. The intensity profiles are seen to be close to a Gaussian profile with the steepest slope at a cantilever deflection of 3 μm. The expected shift of the mode profile as seen in figure 6.11(B) is not easy to determine. However, the shift is only expected to be 1 μm which is the size of the steps the micrometer screw is moved and therefore very difficult to detect. At a light intensity around 1 μW the noise in the photo-detector is $\sim$ 5 nW. This means that the minimum detectable difference in the read-out signal of the photo-detector is 0.01 μW. From the plot in figure 8.7 such an intensity change corresponds to only a 45 nm deflection of the cantilever, if the cantilever is operated in the region of steepest slope in the graph (with an initial cantilever deflection of 3 μm). Using Stoney's equation (3.1) this translates to a surface stress sensitivity of only 0.19 N/m.

8.4 Reflection mode

The read-out sensitivity of the reflection mode is monitored simultaneously with the transmission mode where the probe is moved in 1-μm-steps in 3 min time intervals. Figure 8.8 shows the output in the reflection mode read-out as the probe is moved downwards.

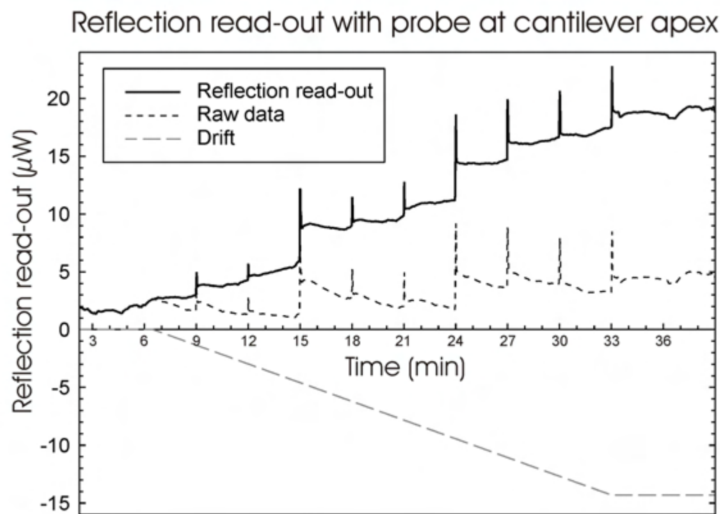

Figure 8.8: Typical data obtained in the reflection mode read-out. When the cantilever is deflected the reflection signal is increased because light is reflected off the tungsten tip.

Both the raw data, the drift and the resulting output signal are plotted. Again, the level of the drift is found from the slope of the light grey plot. The drift is calculated from the linear 3 min intervals and it is assumed the drift stems from the drift of the micrometer screw as it is moved downwards. After the negative drift in the output data is subtracted the contradicting observation is made that the reflection signal *increases* when the cantilever is deflected. Figure 8.9 shows the side view of the set-up at the cantilever waveguide region. The figure is drawn to scale to give a clear impression of the situation.

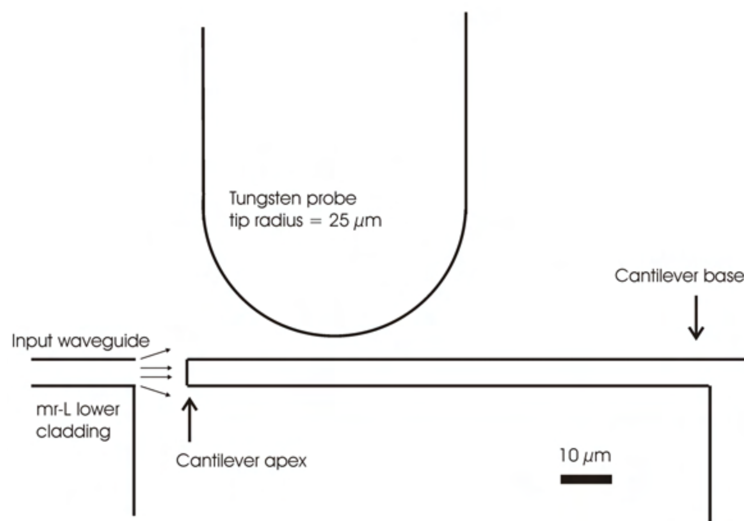

Figure 8.9: Schematic drawing of the probe used to deflect the cantilever. The image is drawn to scale for the 100 μm long cantilever used and it can clearly be seen that it is likely that the probe has a large influence on the reflected light.

Since the probe is placed at the apex of the cantilever the most likely reason for the observed increase in the read-out signal is that light reflects *off the probe*. To investigate this assumption the same experiment is performed placing the probe at the cantilever base instead of the apex. For this measurement the probe is moved downwards in 5 μm steps in 3 min time intervals and a lower resolution is therefore obtained from the measurement. Figure 8.10 shows the comparison between the data obtained for the two different probe positions.

It is clearly seen that the position of the probe along the cantilever is highly influential on the result of the read-out signal. The probe is first placed at the apex of the cantilever to obtain a correct calibration of the cantilever deflection. However, with respect to the optical read-out this is not

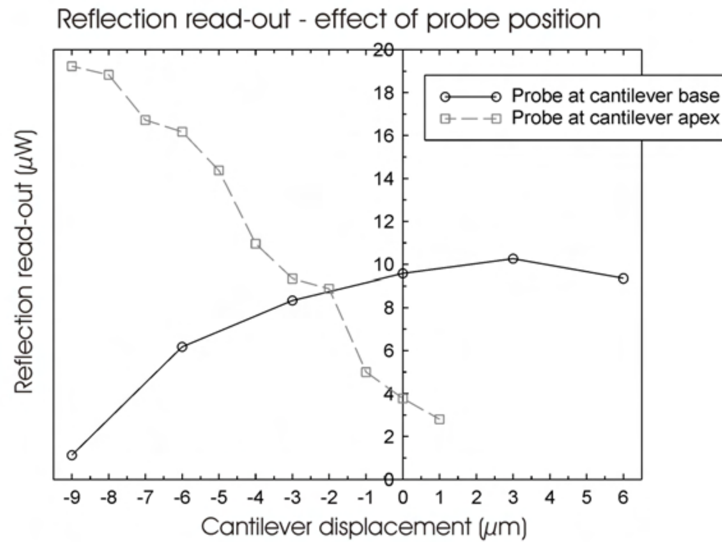

Figure 8.10: When the probe is placed at the apex of the cantilever the light intensity increases as the cantilever is deflected (grey squares). When the probe is pushing close to the clamping position of the cantilever the light intensity decreases (black circles).

the optimal position as the probe itself is seen to reflect light back into the input waveguide. In fact, close to 100 % of the light is reflected at a cantilever deflection of 9 μm. When the probe is placed close to the point of clamping of the cantilever the output signal decreases with increased cantilever deflection. This shows that light is probably not reflected off the probe in this situation. However, here it is not possible to determine the cantilever deflection precisely. Moreover, the cantilever becomes permanently deflected when the probe is pushing at the base due to mechanical rupture. It can therefore be concluded that this method of calibration of the system is not optimal for the reflection mode read-out and a minimum detectable deflection cannot be determined. It would be preferable to have a non-reflective probe or alternatively to structure an integrated electrode in the cantilever that can be used to thermally deflect the cantilever a known distance [121].

8.5 Comparison with theoretical calculations

The experimentally obtained data is compared with the theoretically calculated values of the read-out sensitivities of the two modes. Figure 8.11 shows the expected intensity variations with an optical input of 20 μW, which is the value of the fiber-to-fiber (FTF) measurement. The calculated output

intensity for zero displacement of the cantilever is 0.535 µW in the reflection mode and 7.35 µW in the transmission mode. The significantly lower value in the reflection mode is because of the low reflectivity of the cantilever front-end, as discussed in Chapter 5. From figure 8.10 an optical output in the order of 10 µW is measured in the reflection mode at zero deflection of the cantilever waveguide. From figure 8.7 the corresponding value for the transmission mode is noted to be 1.2 µW. A large deviation is seen between the calculated and the measured values in both read-out modes.

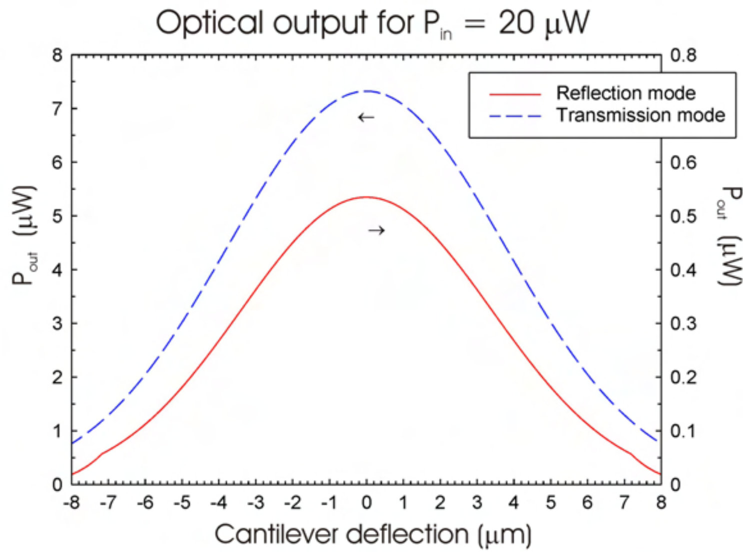

Figure 8.11: Expected optical output for P_{in} of 20 µW. When the cantilever is perfectly aligned with the input waveguide an output intensity of 0.535 µW is expected in the reflection mode and 7.35 µW is expected for the transmission mode.

For the reflection mode read-out the intensity of the measured reflected light is 20 times higher than the calculated value. The reason for the large difference is that the theoretical approach does not account for the reflections off the input fiber end and the input waveguide facet. In Chapter 6 the importance of the facet quality is discussed and it is clearly seen in figure 6.6 that even the sawn samples show a facet with a rather high surface roughness. This surface roughness decreases the coupling efficiency into the waveguide and results in large reflections due to scattering. Moreover, the surface roughness of the cantilever front-end is not accounted for here. Most likely it is not perfectly smooth and an increase in the reflected light intensity can therefore be expected. Moreover, parasitic reflections occur from all other surfaces of the system. These are also not accounted for in

the theoretical model. It is therefore not surprising to see that the amount of reflected light in the measurement is considerably higher than in the theoretical calculations.

To analyse the situation in the transmission mode read-out it is easier to translate the throughput intensity to losses across the system. The loss of the system is calculated from the simple expression

$$\text{Loss} = 10 \times \log\left(\frac{P_{out}}{P_{in}}\right)$$

where P_{in} is the value from the FTF measurement [95].

The theoretically expected loss in the transmission mode is 4.4 dB and the measured value is 12.2 dB. The difference between these two values arises because the coupling loss into the system and the propagation loss through the waveguides are not included. There might also be losses introduced by the taper of the output waveguide. When these factors also are included the value of the expected loss increases to

$$\text{Total loss} = 4.4 + (2 \times 0.2) + (1.65 \times 1.2) + 0.5 = 7.28 \text{ dB}$$

There is still approximately 5 dB loss that is not accounted for. This might be attributed to a greater coupling and propagation loss of these waveguides as compared to the embedded waveguides investigated in Chapter 6. Figure 8.12 marks the different regions in the system that contribute to each extra source of loss.

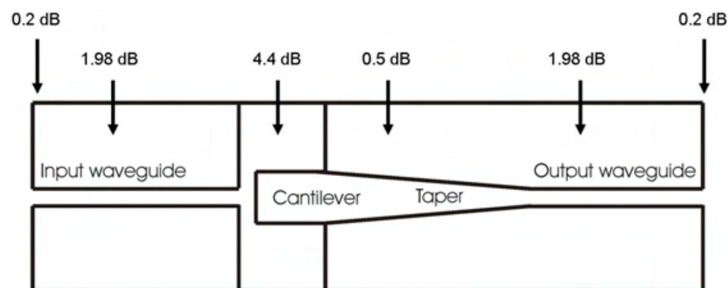

Figure 8.12: The extra sources of loss introduced into the transmission mode read-out are marked on this schematic drawing of the system.

Figure 8.13 plots the comparison between the measurements and the theoretically calculated sensitivity of the two read-out modes. The theoretical curve for the reflection mode is multiplied by a factor 20 and the transmission mode curve is multiplied by a factor 0.2 to account for the extra sources of losses in the complete system generating the discrepancy between theory and measurements. From the data it can be seen that the calculated sensitivity of the transmission mode compares very well with the measured sensitivity once the correction factor has been applied. The fit between theory and measurement is not as good in the reflection mode. The better agreement between theory and measurement in the transmission mode compared to the reflection mode is simply because both the theoretical model and the measurements are more straight-forward for the transmission mode read-out.

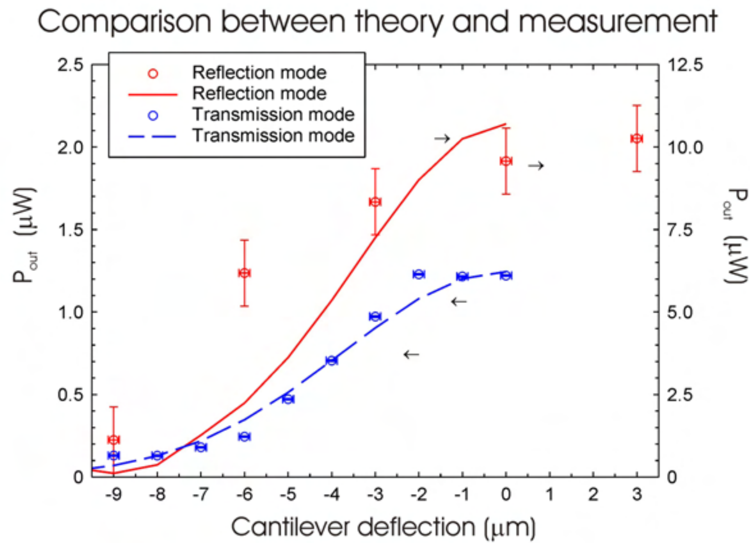

Figure 8.13: Comparison between theoretical and experimental results. A good fit is seen between the theoretical curve and the measured values when the total losses in the system are included for the transmission mode. The fit for the reflection read-out mode is not as good. The curve of the theoretical values for the reflection mode is multiplied by a factor 20 and the curve for the theoretical values of the transmission mode is multiplied by a factor 0.2.

8.6 Summary

The aim of this chapter is to show the proof-of-principle of the two read-out modes of the integrated optical detection system developed in this PhD. To do that, first it is assured that light *can* propagate through the system by observing the mode profiles of the input waveguide and of the light exiting the system. No significant difference in the MFDs is observed. The read-out from the two modes are monitored simultaneously as the cantilever is mechanically deflected in 1 μm steps by a tungsten probe. The deflections of the probe is controlled with a micrometer screw placed at the apex of the cantilever. From the experiments it can be concluded that this is not the ideal method of calibrating the system in the reflection mode since the probe has a tip diameter of 50 μm and interferes with the light path significantly. However, proof-of-principle is shown for the two read-out modes with an expected deflection sensitivity of 45 nm for the transmission mode if the cantilever is operated in the region of highest sensitivity. Optimisation of the calibration method needs to be performed before a conclusive values can be determined for the read-out sensitivity in the reflection mode. From the measurements it is also seen that the shift of the center position of the mode profile due to the inhomogeneous waveguide structure is not significant so an initial cantilever deflection of 2 - 3 μm is required for optimal sensitivity. Such deflection could be achieved by coating the cantilever with a layer of Au after the release [122]. This Au layer can also be used for binding the probe molecules via thiol-chemistry.

Chapter 9

Concluding Remarks

9.1 Alternative read-out method

During the work on this PhD project an idea of another detection scheme was also discussed. In this scheme, light enters the system via an input waveguide, like in the systems presented. Opposite to the presented read-out methods though, this input waveguide is on the same side of the air gap as the cantilever, which the light passes through. After exiting the cantilever and travelling across the air gap the light reaches an inclined surface and is reflected out of the system. Such a design makes it possible to place the photo-detector in the lid of the packaging of the system or alternatively at the bottom of the micro channel. Moreover, instead of simply detecting the intensity variations of the through-coupled light this read-out scheme is a pure miniaturised version of the optical lever principle known from AFM, where the movement of the output light is followed on the photo-detector.

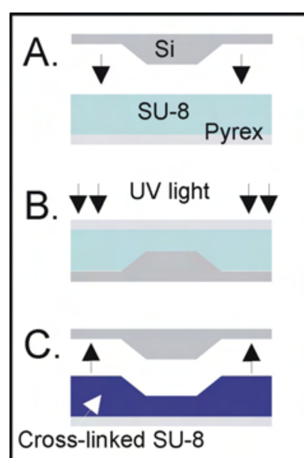

Figure 9.1: Schematic drawing of the 'Step-and-Flash' fabrication method.

Such a system requires a 45° sloped side wall at the opposite side of the cantilever. Standard UV-lithography does not allow for such structuring so the method of *'Step-and-Flash'* is investigated. Figure 9.1 shows the method schematically. The process steps are the same as for standard UV-lithography with the modification that a mould is used to form the SU-8 during the soft bake before it is exposed and cross-linked. Here, a KOH-etched Si stamp is used as the mould and the stamp can easily be removed once the polymer is cross-linked. The structures in the Si stamp used here have an inclination of 54.7° from the KOH etching but there are alternative etching recipes that allow for a resulting 45° degree etching angle [123]. More details on the process optimisation and possible applications of this fabrication method is found in the publication *Sloped side walls in SU-8 structures with 'Step-and-Flash' processing* [124]. Figure 9.2 shows SEM images comparing the Si stamp used and the resulting SU-8 structures. A very good agreement in the spatial resolution is seen.

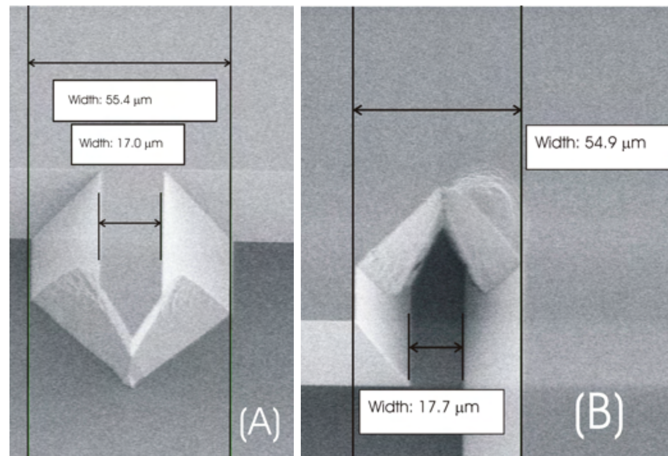

Figure 9.2: SEM images of (A) Si stamp and (B) the resulting SU-8 structures patterned with 'Step-and-Flash'.

9.2 Conclusions

In this PhD project the fabrication of a novel read-out method for a cantilever based sensor based on integrated optics is presented. A new material combination is investigated to obtain single-mode waveguides with low propagation losses. Both the cantilevers and the waveguides are structured in a polymeric material suitable for the fabrication of the complete sensing system. The negative resist SU-8 is used for the cantilever waveguide material and the negative resist mr-L is used as cladding material of the waveguides as well as the device material of the complete system.

Embedded waveguides with a propagation loss of 1.2 dB/cm at 1 310 nm and coupling loss of 0.25 dB/facet at the same wavelength are fabricated and characterised. This material combination is highly suitable for the fabrication of an all-polymeric device, especially since the mr-L resist is specifically designed as a low-stress material where the complete backbone of the system can be fabricated without the issue of delamination and cracking.

The sensitivity of the refractive index of the polymers to changes in the processing is studied in detail. It is shown that it is highly important to always apply the same process parameters to the different waveguide layers to obtain identical waveguides across different batches.

The mode profiles are studied of both homogeneous and in-homogenous waveguides to ensure that only single-mode propagation occurs and to facilitate the calibration process of the read-out methods. From the mode profiles it is seen that the penetration depth of the light differs between the top and bottom cladding due to the process sensitivity of the mr-L polymer. However, no significant shift of the mode profile is seen for the embedded waveguides. It can therefore be concluded that the difference in the index step is minor.

A novel fabrication method is developed to enable the direct fabrication of free-hanging structures patterned in a negative resist applying only UV-lithography. By using a release layer with a tailored adhesion [125] the structures are fabricated on a Si wafer and afterwards transferred onto another wafer via a *bond-and-transfer* process. The structures remain on the final Pyrex wafer for support. Before experiments the samples are sawn out and it is shown that the cleaving technique is highly influential on the final coupling loss of the waveguides.

Theoretical calculations, using the Gaussian approximation of the mode profiles, are performed to find values of the bending sensitivity in both read-out modes. The sensitivity of the reflection mode is expected to be higher than the transmission mode but the signal-to-noise ratio of the reflection mode is seen to be significantly lower. Two methods to increase this are discussed. The transmission mode has a calculated minimum detectable cantilever deflection of 30 nm.

Finally, proof-of-principle is shown for both detection modes by mechanically deflecting the cantilever while simultaneously recording the optical outputs. In the transmission mode read-out a minimum detectable cantilever deflection of 45 nm is measured in the most sensitive region. No conclusive value can be given for the reflection mode read-out since the calibration

method proved to have flaws for this read-out mode. However, with the integration of an electrode to thermally displace the cantilever it is expected to be possible to calibrate even this read-out mode. Such a calibration method would also result in cantilever deflections in the same order as the deflections expected from real life applications of this system.

As a final conclusion, this work shows the integration of a novel read-out method utilising integrated optics in an all-polymer device. Such a system has not been presented in the literature before. It is believed that both read-out modes present two interesting new types of integrated read-out for cantilever based sensors. Optical read-out has benefits over electrical integrated read-out since it is not affected by conducting liquids or external electromagnetic fields. There might be an issue with the adsorption of the probe molecules onto the cantilever since this could affect the mode profile of the cantilever waveguide. There might also be issues with water absorption of the polymeric materials, although this is expected to be very low. Neither of these effects have been studied in this work. The reflection mode has the advantage over the transmission mode that it does not use the cantilever as a waveguide. Thereby, it is not as sensitive to refractive index changes of the surrounding medium or surface stress changes on the cantilever. The greatest challenge for the reflection mode read-out is to obtain a sufficiently high signal-to-noise ratio. This could be achieved e.g. by coating the cantilever front-end with a reflective layer.

The commercial interest of such a biosensor as presented here was investigate by participation in the nation-wide business plan competition Venture Cup 2005/2006. Out of a total of 80 originally submitted business plans, the PolyCan business plan was chosen top-five with respect to the business idea, top-ten with respect to the commercialisation plan and awarded an over-all third position in the competition. This clearly shows that there is a large commercial interest in a cantilever based biosensor developed for point-of-care analyses and it is with greatest sincerity I hope to see this work further developed.

Bibliography

[1] M.J. Madou. *Fundamentals of microfabrication.* CRC Publisher, Boca Raton, 2nd edition, 2002

[2] B.R. Eggins. *Chemical Sensors and Biosensors.* Wiley & Sons, Stuttgart, 2002

[3] M. Keusgen. Biosensors: new approaches in drug discovery, *Naturwissenschaften* **89** (2002) 433-444

[4] G.M. Shepherd. *Neurobiology*, Oxford University Press, New York, 3rd edition, 1994

[5] E. Engvall, P. Perlman. Enzyme-linked immunosorbent assay (ELISA). Quantitative assay of immunoglobulin G, *Immunochemistry* **8**(9) (1971) 871-874

[6] www.q-sense.com

[7] www.biacore.com

[8] www.axelabiosensors.com

[9] www.corning.com

[10] G. Binning, C.F. Quate, Ch. Gerber. Atomic force microscope, *Physical Review Letters* **56**(9) (1986) 930-933

[11] T.R. Albrecht, C.F. Quate. Atomic resolution imaging of a nonconductor by atomic force microscopy, *Journal of Applied Physics* **62**(7) (1987) 2599-2602

[12] T. Thundat, R.J. Warmack, G.Y. Chen, D.P. Allison. Thermal and ambient-induced deflections of scanning force microscope cantilevers, *Applied Physics Letters* **64**(21) (1994) 2894-2896

[13] J.K. Gimzewski, Ch. Gerber, E. Meyer, R.R. Schlittler. Observation of a chemical reaction using a micromechanical sensor, *Chemical Physics Letters* **217**(5-6) (1994) 589-594

[14] D.R. Baselt, G.U. Lee, R.J. Colton. Biosensor based on force microscope technology, *Journal of Vacuum Science and Technology B* **14**(2) (1996) 789-793

[15] L.G. Carrascosa, M. Moreno, M. Álvarez, L.M. Lechuga. Nanomechanical biosensors: a new sensing tool, *Trends in Analytical Chemistry* **25**(3) (2006) 196-206

[16] B. Ilic, C. Czaplewski, M. Zalalutdinov, H.G. Craighead, P. Neuzil, C. Campagnolo, C. Batt. Single cell detection with micromechanical oscillators, *Journal of Vacuum Science and Technology B* **19**(6) (2001) 2825-2828

[17] R. Raiteri, M. Grattarola, H.-J. Butt, P. Skládal. Micromechanical cantilever-based biosensors, *Sensors and Actuators B* **79** (2001) 115-126

[18] M.F. Hagan, A. Majumdar, A.K. Chakraborty. Nanomechanical forces generated by surface grafted DNA, *Journal of Physical Chemistry B* **106** (2002) 10163-1013

[19] K.W. Wee, G.Y. Kang, J. Park, J.Y. Kang, D.S. Yoon, J.H. Park, T.S. Kim. Novel electrical detection of label-free disease marker proteins using piezoresistive self-sensing micro-cantilevers, *Biosensors & Bioelectronics* **20** (2005) 1932-1938

[20] M. Álvarez, A. Calle, J. Tamayo, L.M. Lechuga, A. Abad, A. Montoya. Development of nanomechanical biosensors for detection of the pesticide DDT, *BioSensors & BioElectronics* **18** (2003) 649-653

[21] S. Cherian, R.K. Gupta, B.C. Mullin, T. Thundat. Detection of heavy metal ions using protein-functionalized microcantilever sensors, *BioSensors & BioElectronics* **19** (2003) 411-416

[22] K.M. Hansen, H.-F. Ji, G. Wu, R. Datar, R. Cote, A. Majumdar, T. Thundat. Cantilever-based optical deflection assay for discrimination of DNA single-nucleotide mismatches, *Analytical Chemistry* **73** (2001) 1567-1571

[23] J. Fritz, M.K. Baller, H.P. Lang, H. Rothuizen, P. Vettiger, E. Meyer, H.-J. Güntherodt, Ch. Gerber, J.K. Gimzewski. Translating biomolecular recognition into nanomechanics, *SCIENCE* **288** (2000) 316-318

[24] G. Wu, H. Ji, K. Hansen, T. Thundat, R. Datar, R. Cote, M.F. Hagan, A.K. Chakraborty, A. Majumdar. Origin of nanomechanical cantilever motion generated from biomolecular interactions, *Proceedings of the National Academy of Science of the USA* **98**(4) (2001) 1560-1564

[25] R. McKendry, J. Zhang, Y. Arntz, T. Strunz, M. Hegner, H.P. Lang, M.K. Baller, U. Certa, E. Meyer, H.-J. Güntherodt, Ch. Gerber. Multiple label-free biodetection and quantitative DNA-binding assay on a nanomechanical cantilever array, *Proceedings of the National Academy of Science of the USA* **99**(15) (2002) 9783-9788

[26] R. Berger, E. Delamarche, H.P. Lang, Ch. Gerber, J.K. Gimzewski, E. Meyer, H.-J. Güntherodt. Surface stress in the self-assembly of alkanethiols on gold, *SCIENCE* **276** (1997) 2021-2024

[27] F. Liu, Y. Zhang, Z.-C. Ou-Yang. Flexoelectric origin of nanomechanical deflection in DNA-microcantilever system, *BioSensors & Bioelectronics* **18** (2003) 655-660

[28] M. Álvarez, L.G. Carrascosa, M. Moreno, A. Calle, Á. Zaballos, L.M. Lechuga, C. Martínez-A, J. Tamayo. Nanomechanics of the formation of DNA self-assembled monolayers and hybridisation on microcantilevers, *Langmuir* **20** (2004) 9663-9668

[29] M.R. Begley, M. Utz, U. Komaragiri. Chemo-mechanical interactions between adsorbed molecules and thin elastic films, *Journal of the Mechanics and Physics of Solids* **53** (2005) 2119-2140

[30] N. Backmann, C. Zahnd, F. Huber, A. Bietsch, A. Plückthun, H.P. Lang, H.-J. Güntherodt, M. Hegner, Ch. Gerber. A label-free immunosensor array using single-chain antibody fragments, *Proceedings of the National Academy of Science of the USA* **102**(41) (2005) 14587-14592

[31] M. Godin, P.J. Williams, V. Tabard-Cossa, O. Laroche, L.Y. Beaulieu, R.B. Lennox, P. Grütter. Surface stress, kinetics, and structure of alkanethiol self-assembled monolayers, *Langmuir* **20** (2004) 7090-7096

[32] H.P. Lang, R. Berger, F. Battiston, J.-P. Ramseyer, E. Meyer, C. Andreoli, J. Brugger, P. Vettiger, M. Despont, T. Mezzacasa, L. Scandella, H.-J. Güntherodt, Ch. Gerber, J.K. Gimzewski. A chemical sensor based on a micromechanical cantilever array for the identification of gases and vapors, *Applied Physics A* **66** (1998) 561-564

[33] M.K. Baller, H.P. Lang, J. Fritz, Ch. Gerber, J.K. Gimzewski, U. Drechsler, H. Tohuizen, M. Despont, P. Bettiger, F.M. Battiston, J.P. Ramseyer, P. Fornaro, E. Meyer, H.-J. Güntherodt. A cantilever array-based artificial nose, *Ultramicroscopy* **82** (2000) 1-9

[34] R. Berger, Ch. Gerber H.P. Lang, J.K. Gimzewski. Micromechanics: A toolbox for femtoscale science: "Towards a laboratory on a tip", *MicroElectronic Engineering* **35** (1997) 373-379

[35] www.spmtips.com

[36] www.atomicforce.de/Olympus_Cantilevers/olympus_cantilevers.html

[37] www.budgetsensors.com

[38] M. Calleja, J. Tamayo, A. Johansson, P. Rasmussen, L. Lechuga, A. Boisen. Polymeric cantilever arrays for biosensing applications, *Sensor Letters* **1** (2003) 20-24

[39] M. Nordström. Fabrication of cantilever chip with complementary micro channel sytem in SU-8 for biochemical detection, *MSc Thesis*, Technical University of Denmark & Lund University (2004)

[40] A. Johansson, M. Calleja, P.A. Rasmussen, A. Boisen. SU-8 cantilever sensor system with integrated readout, *Sensors and Actuators A* **123-124** (2005) 111-115

[41] A.W. McFarland, M.A. Poggi, L.A. Bottomley, J.S. Colton. Production and characterization of polymer microcantilevers, *Review of Scientific Instruments* **75**(8) (2004) 2756-2758

[42] X.R. Zhang, X. Xu. Development of a biosensor based on laser-fabricated polymer microcantilevers, *Applied Physics Letters* **85**(12) (2004) 2423-2425

[43] W.H. Song, A. Hierlemann, J. Lichtenberg. Dead-end injection molding of polymeric microcantilever arrays, *Proceedings of IEEE; 13th International Conference on Solid-State Sensors, Actuators and Microsystems (Transducers '05)* **2** (2005) 2040-2043

[44] G. Meyer, N.M. Amer. Novel optical approach to atomic force microscopy, *Applied Physics Letters* **53**(12) (1988) 1045-1047

[45] M. Yue, H. Lin, D.E. Dedrick, S. Satyanarayana, A. Majumdar, A.S. Bedekar, J.W. Jenkins, S. Sundaram. A 2-D microcantilever array for multiplexed biomolecular analysis, *Journal of Microelectromechanical systems* **13**(2) (2004) 290-299

[46] A. Boisen, J. Thaysen, H. Jensenius, O. Hansen. Environmental sensors based on micromachined cantilevers with integrated read-out, *Ultramicroscopy* **82** (2000) 11-16

[47] J. Thaysen, A.D. Yalçinkaya, P. Vettiger, A. Menon. Polymer-based stress sensor with integrated readout, *Journal of Physics D: Applied Physics* **35**(21) (2002) 2698-2703

[48] M.K. Baller, J. Fritz, Ch. Gerber, J. Gimzewski, H.P. Lang. Cantilever sensors and transducers, *Patent Application WO 01/33,226*

[49] www.thomsonderwent.com

[50] B.M. Evans, P.G. Datskos, S. Rajic. Integrated optical interrogation of micro-structures, *Patent Application WO 01/20617*

[51] A.T. Tran, D.W. Carr. Molecular detection using an optical waveguide fixed to a cantilever, *Patent Application US 2005/0018946*

[52] G. Nordin, J.C. Gonzalez. Optical waveguide microcantilever with differential output and associated methods of cantilever sensing, *Patent Application US 2005/0195407*

[53] K. Zinoviev, C. Dominguez, J.A. Plaza, V.J. Cadarso Busto, L.M. Lechuga. A novel optical waveguide microcantilever sensor for the detection of nanomechanical forces, *Journal of Lightwave Technology* **24**(5) (2006) 2132-2138

[54] T. Xu, R. Chang, M. Bachman, G.-P. Li. Optical polymer waveguide based cantilevers for chemical and biological sensors, *Proceeings of IEEE; Sensors* (2005)

[55] R. Marie, J. Thaysen, C.B.V. Christensen, A. Boisen. A cantilever-based sensor for thermal cycling in buffer solution, *Microelectronic Engineering* **67-68** (2003) 893-898

[56] E. Hecht. *Optics.* Addison-Wesley, San Francisco, 1998

[57] F. Ladouceur, J.D. Love. *Silica-based buried channel waveguides and devices.* Chapman & Hall, London, 1996

[58] B.E.A. Saleh, M.C. Teich. *Fundamentals of Photonics.* Wiley & Sons, New York, 1991

[59] www.thorlabs.com

[60] G.G. Stoney. The tension of metallic films deposited by electrolysis, *Proceedings of the Royal Society of London* **82**(553) (1909) 172-175

[61] P.G. Datskos, N.V. Lavrik, S. Rajic. Performance of uncooled microcantilever thermal detectors, *Review of Scientific Instruments* **75**(4) (2004) 1134-1148

[62] D. Nilsson, S. Balslev, A. Kristensen. A microfluidic dye laser fabricated by nanoimprint lithography in a highly transparent and chemically resistant cyclo-olefin copolymer (COC), *Journal of Micromechanics and Microengineering* **15** (2005) 296-300

[63] M. Heckele. Hot embossing - a flexible and successful replication technology for polymer MEMS, *Proceedings of SPIE; Microfluidics, BioMEMS and Medical Microsystems II* **5345** (2003) 108-117

[64] W. Michaeli, J. Forster. Production of polymer lenses using injection moulding, *Journal of Polymer Engineering* **26**(2-4) (2006) 133-146

[65] A.L. Bogdanov, S.S. Peredkov. Use of SU-8 photoresist for very high aspect ratio x-ray lithography, *Microelectronic Engineering* **53** (2000) 493-496

[66] B. Bilenberg, S. Jacobsen, M.S. Schmidt, L.H.D. Skjolding, P. Shi, P. Bøggild, J.O. Tegenfeldt, A. Kristensen. High resolution 100 kV electron beam lithography in SU-8, *Microelectronic Engineering* **83** (2006) 1609-1612

[67] M. Calleja, M. Nordström, D. Haefliger, A. Boisen, L.M. Lechuga, J. Tamayo. Direct real-time immunodetection of the human growth hormone with polymeric nanomechanical sensors, *Proceedings of Eurosensors XIX*, Barcelona, Spain, September 11-14 2005

[68] M. Calleja, L.G. Carrascosa, A. Tarín, J. Tamayo. Study of the adsorption of sulfur-derivatized single stranded DNA on gold by atomic force microscopy and the cantilever bending technique, *Sensor Letters* **4** (2006) 275-280

[69] S. Musa, A. Borreman, A.A.M. Kok, M.B.J. Diemeer, A. Driessen. Experimental study of bent multimode optical waveguides, *Applied Optics* **43**(30) (2004) 5705-5707

[70] J.M. Hagerhorst-Trewhella, J.D. Gelorme, B. Fan, A. Speth, D. Flagello, M.M. Oprysko. Polymeric optical waveguides, *Proceedings of SPIE; Integrated Optics and Optoelectronics* **1177** (1989) 379-386

[71] www.microresit.de

[72] S. Obi, M.T. Gale, A. Kuoni, N. De Rooij. Replication of optical MEMS structures in sol-gel materials, *Microelectronic Engineering* **73-74** (2004) 157-160

[73] R. Houbertz, G. Domann, C. Cronauer, A. Schmitt, H. Martin, J.-U. Park, L. Frölich, R. Buestrich, M. Popall, U. Streppel, P. Dannberg, C. Wächter, A. Brüer. Inorganic-organic hybrid materials for application in optical devices, *Thin Solid Films* **442** (2003) 194-200

[74] C. Rosher, R. Buestrich, P. Dannberg, O. Rösch, M. Popall. New inorganic-organic hybrid polymers for integrated optics, *Proceedings of the 1998 MRS Spring Symposium; Organic/Inorganic Hybrid Materials* **519** (1998) 239-244

[75] D. Schönfeld, O. Rösch, P. Dannberg, A. Bräuer, R. Müller-Fiedler, M. Popall, R. Buestrich. Enhanced performance of polymer waveguides by

replication and UV-patterning in ORMOCER, *Proceedings of SPIE; Precision Plastic Optics for Optical Storage, Displays, Imaging and Communications* **3135** (1997) 53-61

[76] K.B. Mogensen, J. El-Ali, A. Wolff, J.P. Kutter. Integration of polymer waveguides for optical detection in microfabricated chemical analysis systems, *Applied Optics* **42**(19) (2003) 4072-4079

[77] J.-S. Kim, J.-W. Kang, J.-J. Kim. Simple and low cost fabrication of thermally stable polymeric multimode waveguides using a UV-curable epoxy, *The Japan Society of Applied Phyiscs* **42** (2003) 1277-1279

[78] K.K. Tung, W.H. Wong, E.Y.B. Pun. Polymeric optical waveguides using direct ultraviolet photolithography process, *Applied Physics A* **80** (2005) 621-626

[79] R. Müller, P. Obreja, M. Kusko, D. Esinenco, C. Tibeica, G. Conache, L. Buia, D. Apostol, V. Damian, M. Mateescu, M. Diacuno, L. Moldovan. SU-8 used as optical waveguide in integrated optical microsensor for biological applications, *Proceedings of SPIE; Advanced Topics in Optoelectronics, Microelectronics and Nanotechnologies II* **5972** (2005) 59720Z1-6

[80] N. Pelletier, B. Bêche, E. Gaviot, L. Camberlein, N. Grossard, F. Polet, J. Zyss. Single-mode rib optical waveguides in SOG/SU-8 polymer and integrated Mach-Zehnder for designing thermal sensors, *IEEE Sensors Journal* **6**(3) (2006) 565-570

[81] J.M. Ruano-López, M. Aguirregabiria, M. Tijero, M.T. Arroyo, J. Garcia, J. Berganzo, I. Aranburu, F.J. Blanco, K. Mayora. A new SU-8 process to integrate buried waveguides and sealed microchannels for a Lab-on-a-Chip, *Sensors and Actuators B* **114** (2006) 542-551

[82] R. Ruhmann, G. Ahrens, A. Schuetz, J. Voskuhl, G. Gruetzner. Reduction of internal stress in a SU-8-like negative tone photoresist for MEMS applications by chemical modification, *Proceedings of SPIE; Advances in Resist Technology and Processing XVIII* **4345** (2001) 502-510

[83] N. LaBianca, J.D. Gelorme. Hight aspect ratio resist for thick film applications, *Proceedings of SPIE; Advances in Resist Technology and Processing XII* **2438** (1995) 846-852

[84] R. Feng, R.J. Farris. Influence of processing conditions on the thermal and mechanical properties of SU8 negative photoresist coatings, *Journal of Micromechanics and Microengineering* **13** (2003) 80-88

[85] T.A. Anhøj, A.M. Jørgensen, D.A. Zauner, J. Hübner. The effect of soft bake temperature on the polymerization of SU-8 photoresist, *Journal of Micromechanics and Microengineering* **16** (2006) 1819-1824

[86] M. Gaudet, J.-C. Camart, L. Buchaillot, S. Arscott. Varition of absorption coefficient and determination of critical dose of SU-8 at 365 nm, *Applied Physics Letters* **88** (2006) 024107

[87] B.H. Ong, X. Yuan, S. Tao, S.C. Tjin. Photothermally enabled lithography for refractive-index modulation in SU-8 photoresist, *Optics Letters* **31**(10) (2006) 1367-1369

[88] www.metricon.com

[89] M. Doi, *Introduction to Polymer Physics.* Clarendon Press, Oxford, 1996

[90] R. Syms, J. Cozens. *Optical guided waves and devices.* McGraw-Hill, London, 1992

[91] S.-K. Kim, K. Geary, W. Yuan, H.R. Fetterman, D.-G. Lee, C. Zhang, C. Wang, W.H. Steier, G.-C. Park, S.-J. Gang, I. Oh. Stress-induced polymer waveguides operating at both 1.31 and 1.55 μm wavelengths, *Electronics Letters* **40**(14) (2004)

[92] Simulations performed by Dan A. Zauner, MIC, DTU.

[93] J.M. Shaw, J.D. Gelorme, N.C. LaBianca, W.E. Conley, S.J. Holmes. Negative photoresists for optical lithography, *IBM Journal of Research and Development* **41**(1/2) (1997) 81-94

[94] B.G. Osborne, T. Fearn. *Near infrared spectroscopy in food analysis.* Longman Scientific & Technical, John Wiley & Sons, Harlow, 1986

[95] A.W. Snyder, J.D. Love. *Optical waveguide theory.* Kluwer Academic Publishers, London, 1983

[96] A. Johansson, G. Blagoi, A. Boisen. Polymeric cantilever-based biosensors with integrated readout, *Applied Physics Letters* **89** (2006) 173505

[97] S. Metz, S. Jiguet, A. Bertsch, Ph. Renaud. Polyimide and SU-8 microfluidic devices manufactured by heat-depolymerization sacrificial material technique, *Lab on a Chip* **4** (2004) 114-120

[98] D. Haefliger, A. Boisen. Three-dimensional microfabrication in negative resist using printed masks, *Journal of Micromechanics and Microengineering* **16** (2006) 951-957

[99] M. Agirregabiria, F.J. Blanco, J. Berganzo, M.T. Arroyo, A. Fullaondo, K. Mayora, J.M. Ruano-López. Fabrication of SU-8 multilayer microstructures based on successive CMOS compatible adhesive bonding and releasing steps, *Lab on a Chip* **5** (2005) 545-552

[100] www2.dupont.com/Kapton/en_US/index.html

[101] M.C. Cheng, A.P. Gadre, J.A. Garra, A.J. Nijdam, C. Luo, T.W. Schneider, R.C. White, J.R. Currie, M. Paranjape. Dry release of polymer structures with anti-sticking layer, *Journal of Vacuum Science Technology A* **22**(3) (2004) 837-841

[102] D. Haefliger, M. Nordström, P.A. Rasmussen, A. Boisen. Dry release of all-polymer structures, *Microelectronic Engineering* **78-79** (2005) 88-92

[103] S. Keller, D. Haefliger, A. Boisen. Optimized dry-release and passivation of thin SU-8 cantilevers, *Proceedings of the 32nd International Conference on Micro and Nano Engineering (MNE 2006)*, Barcelona, Spain, September 17-20 2006

[104] M. Calleja, J. Tamayo, M. Nordström, A. Boisen. Low-noise polymeric nanomechancial biosensors, *Applied Physics Letters* **88** (2006) 113901

[105] C. Kallesøe, T. Pedersen, C. Møller Pedersen. Cantilever based waveguide, *Desktop Project*, MEMS-2, Technical University of Denmark (2004)

[106] A. Johansson. SU-8 cantilever sensor with integrated readout, *PhD Thesis*, Technical University of Denmark (2006)

[107] www.rpi.edu/∼schubert/Education%20resources/Materials%20-%20refractive%20index%20and%20extinction%20coefficient.pdf

[108] M.-H. Wu, H. Cai, X. Xu, J.P.G. Urban, Z.-F. Cui, Z. Cui. A SU-8/PDMS hybrid microfluidic device with integrated optical fibers for online monitoring of lactate, *Biomedical Microdevices* **7**(4) (2005) 323-329

[109] B.Y. Shew, C.H. Kuo, Y.C. Huang, Y.H. Tsai. UV-LIGA interferometer biosensor based on the SU-8 optical waveguide, *Sensors and Actuators A* **120** (2005) 383-389

[110] A.S. Holland, A. Mitchell, V.S. Balkunje, M.W. Austin, M.K. Raghunathan. Fabrication of raised and inverted SU-8 polymer waveguides, *Proceedings of SPIE; Optoelectronic Devices and Integration* **5644** (2005) 353-366

[111] B. Bêche, N. Pelletier, E. Gaviot, J. Zyss. Single-mode TE_{00}-TM_{00} optical waveguides on SU-8 polymer, *Optics Communications* **230** (2004) 91-94

[112] M. Karppinen, J.-T. Mäkinen, K. Kataja, A. Tanskanen, T. Alajoki, T. Karioja, M. Immonen, J. Kivilahti. Embedded optical interconnect on printed wiring board, *Proceedings of SPIE; Micro-Opitcs, VCSELs and Photonic Interconnects* **5453** (2004) 150-164

[113] M. Immonen, J. Wu, J. Kivilahti. Fabrication of polymer optical waveguides with integrated micromirros for out-of-plane surface normal optical interconnects, *Proceedings of IEEE; 4th International Conference on Polymers and Adhesives in Microelectronics and Photonics* (2004) 206-210

[114] N.C. Barford. *Experimental measurements: precision, error and truth.* Addison-Wesly, London, 2nd edition, 1985

[115] G.M. Hale, M.R. Querry. Optical constants of water in the 200-nm to 200-µm wavelength region, *Applied Optics* **12**(3) (1973) 555-563

[116] D. Sarid. *Scanning force microscopy.* Oxford University Press, Oxford, 2nd edition, 1994

[117] J. Hossenlopp, L. Jiang, R. Cernosek, F. Josse. Characterisation of epoxy resin (SU-8) film using thickness-shear mode (TSM) resonator under various conditions, *Journal of Polymer Science B* **42** (2004) 2373-2384

[118] M. Calleja, M. Nordström, M. Álvarez, J. Tamayo, L.M. Lechuga, A. Boisen. Highly sensitive polymer-based cantilever-sensors for DNA detection, *Ultramicroscopy* **105** (2005) 215-222

[119] L. Dellmann, S. Roth, C. Beuret, G.-A. Racine, H. Lorentz, M. Despont, P. Renaud, P. Vettiger. Fabrication process of high aspect ratio elastic structures for piezoelectric motor applications, *Proceedings of IEEE; 9th International Conference on Solid-State Sensors, Actuators and Microsystems (Transducers '97)* **1** (1997) 641-644

[120] www.memsnet.org/material/siliconnitridesi3n4film/

[121] A. Johansson, O. Hansen, J. Hales, A. Boisen. Temperature effects in Au piezoresistors integrated in SU-8 cantilever chips, *Journal of Micromechanics and Microengineering* **16** (2006) 2564-2569

[122] D. Haefliger, O. Hansen, A. Boisen. Self-positioning of polymer membranes driven by thermomechanically induced plastic deformation, *Advanced Materials* **18** (2006) 238-241

[123] S. An, H.-S. Lee, S.-G. Lee, B.-H. O, H.-H. Kim, S.-G. Park, E.-H. Lee. Fabrication of a 45° microreflector ended polymer waveguide using one-step UV embossing technique, *Proceedings of SPIE; Optoelectronic Integrated Circuits VIII* **6124** (2006) 61241M

[124] M. Nordström, J. Hübner, A. Boisen. Sloped side walls in SU-8 structures with 'Step-and-Flash' processing, *Microelectronic Engineering* **83** (2006) 1269-1272

[125] S. Keller, D. Haefliger, A. Boisen. Optimized plasma-deposited fluorocarbon coating for dry release and passivation of thin SU-8 cantilevers, *Journal of Vacuum Science and Technology B*. Accepted for publication.

Appendix A

Facet inclinations

For the reflection mode read-out it is important to minimise the output signal in the RLM from light reflected off any other surface and interface than the cantilever front-end. The major issue is the back-reflected light when the light exits the input waveguide and travels across the air gap. Here, 4.5 % of the input light is back-reflected, which is of the same order as the light reflected off the cantilever front-end and therefore the largest contributor to noise in this read-out mode. By structuring the facet of the input waveguide at an angle one can avoid the back-reflected light being re-coupled into the input waveguide, whereas the light reflected off the cantilever front-end still will be. Figure A.1 shows the light paths for three different situations. Following Snell's law, light is guided by the waveguide when it hits the boundary between the core and the cladding at an angle greater than the critical angle, θ_c. In this situation the requirement translates as

$$\theta_r \leq \theta_p \text{ for waveguiding to occur}$$

where θ_r is the angle between the light path of the returning light inside the waveguide and the direction of propagation.

If the facet of the input waveguide is not inclined, the requirement above is fulfilled as the returning light is reflected at an angle of θ_p. This Appendix derives the requirement of the angle the facet shall be structured at if only the light reflected off the cantilever front-end shall be guided and not the light reflected at the input waveguide/air interface. The small angle approximation is assumed, i.e. sin $\theta \sim \theta$.

For clarity of presentation an exception from the the convention of angle representation is made and all angles are marked as positive in the clock-wise direction.

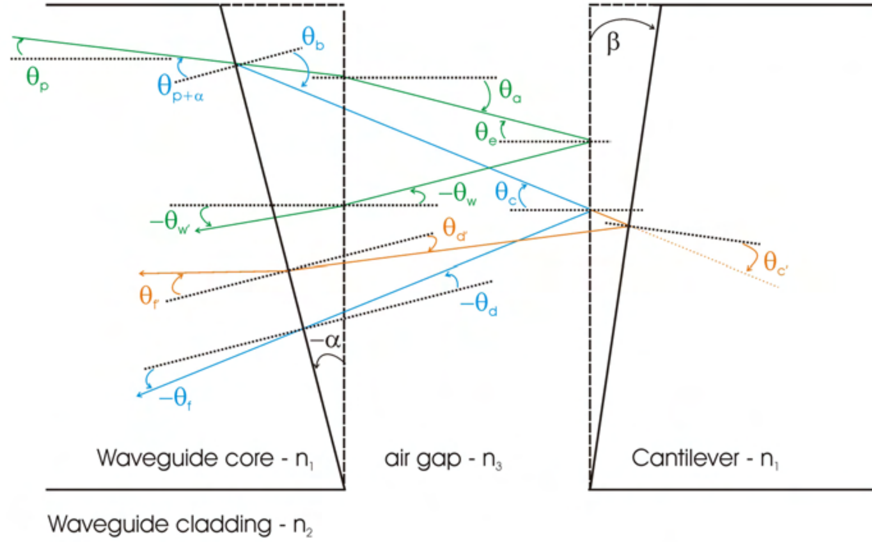

Figure A.1: Schematic drawing of the light paths in the three different situations; no inclination (*green*), when the cantilever front-end is inclined (*blue*) and when both facets are inclined *(orange)*. NB! The dotted orange line inside the cantilever does not represent the light rays coupling into the cantilever but it is simply an extension of the orange light path outside the cantilever.

One inclined facet (blue light path)

First, the situation where only the input waveguide is structured at an angle is considered. The light reflected at the waveguide/air interface will not be re-coupled into the waveguide since the angle of the back-reflected light, $\theta_p + \alpha$ is greater than θ_p. What remains to be ensured is that the light reflected off the cantilever *will be* guided.

Applying Snell's law at the waveguide/air interface gives

$$n_1 \sin\,(\theta_p + \alpha) = n_3 \sin\,\theta_b \qquad \therefore \qquad \theta_b \simeq \frac{n_1}{n_3}\,(\theta_p + \alpha)$$

It can also be seen that

$$\theta_c = \theta_b - \alpha \qquad \text{and} \qquad \theta_d = \theta_c - \alpha$$

which gives

$$\theta_d = \theta_b - 2\alpha$$

For the returning light at the input waveguide Snell's law is applied again, giving

$$n_3 \sin \theta_d = n_1 \sin \theta_f \qquad \therefore \qquad \theta_f \simeq \frac{n_3}{n_1}\, \theta_d$$

For propagation of the reflected light in the waveguide to occur

$$\theta_f + \alpha < \theta_p$$

Substituting for θ_f

$$\theta_p + \alpha - 2\alpha\, \frac{n_3}{n_1} + \alpha < \theta_p \qquad \text{i.e.} \qquad \theta_p + 2\alpha \left[1 - \frac{n_3}{n_1}\right] < \theta_p$$

which gives

$$\frac{n_3}{n_1} > 1$$

This is the requirement of the facet inclination if the reflected light shall be guided. However, $\mathrm{n}_1 = \mathrm{n}_{core}$ and $\mathrm{n}_3 = 1$ so it is not possible to obtain re-coupling of the reflected light when the waveguide facet is inclined.

Both facets inclined (orange light path)

Therefore, it is investigated if the back-reflected light can be coupled into the waveguide by structuring both the input waveguide and the cantilever facets at an angle.

The first part of the problem is the same as in the previous example

$$n_1 \sin\, (\theta_p + \alpha) = n_3 \sin \theta_b \qquad \therefore \qquad \theta_b \simeq \frac{n_1}{n_3}\, (\theta_p + \alpha)$$

It can also be seen that

$$\theta_{c'} = \theta_c - \beta = \theta_b - \alpha - \beta$$

and

$$\theta_{d'} = \theta_{c'} - \beta - \alpha = \theta_b - 2\,(\alpha + \beta)$$

From applying Snell's law when the reflected light returns to the waveguide this expression is obtained for the light entering the waveguide

$$n_3 \sin \theta_{d'} = n_1 \sin \theta_{f'} \qquad \therefore \qquad \theta_{f'} \simeq \frac{n_3}{n_1}\, \theta_{d'}$$

For propagation of the reflected light in the waveguide after returning

$$\theta_{f'} + \alpha < \theta_p$$

Substituting for $\theta_{f'}$

$$\theta_p + \alpha - 2\left(\frac{n_3}{n_1}\right) + \alpha < \theta_p$$

From which α can be related to β as

$$\alpha\left(1 - \frac{n_3}{n_1}\right) - \frac{n_3}{n_1}\,\beta < 0$$

giving

$$\alpha < \frac{n_3}{(n_1 - n_3)}\,\beta$$

This combination is physically possible. So, by structuring both the waveguide and the cantilever interface at an angle the noise in the detection method can be greatly reduced as the light reflected at the waveguide/air interface cannot re-couple back into the input waveguide whereas the light reflected off the cantilever front-end can.

Appendix B

System processing

Wafer A

1. ALIGNMENT MARKS
   - Track 1: AZ 5214E resist, pr 1_5
   - KS Aligner: 6 s expo @ ci2, hard contact. Mask: Alignment marks
   - 120 ° hotplate: 80 s reverse bake
   - KS Aligner: 40 s flood-exposure
   - Developer: NaOH:H_2O (1:5). 70 s under stirring. Rinse in H_2O for 3 min
   - Plasma Asher: 240 sccm O_2, 40 sccm N_2, 400 W, 4 min
   - Alcatel: 300 Å Al
   - Lift-off: Ultra sound in Acetone, 15 min. Rinse in H_2O for 3 min
2. RELEASE LAYER
   - ASE: Fluorocarbon deposition. 1 min 30 s, CF_4 = 120 sccm, p = 60 mTorr
3. WAVEGUIDE AND CANTILEVER LAYER
   - KS Spinner: SU-8 2005. 1st stage: 15 s @ 3 000 rpm and 400 rpm/s 2nd stage: 30 s @ 5 000 rpm and 600 rpm/s
   - Hotplate: Soft bake. 5 min @ 60°C and 10 min @ 90°C
   - KS Aligner: 30 s expo @ ci2, hard contact. Mask: Waveguide structures
   - Hotplate: PEB. 10 min @ 60°C and 10 min @ 90°C
   - Developer: PGMEA. 2 min in First and 2 min in Final, 1.5 rpm stirring. Rinse with Iso-propanol

4. TOP CLADDING
   - KS Spinner: mr-L 6050 XP in syringe. Use gyrset for spinner, t = 3 s, p = 42 psi. 1st stage: 15 s @ 3 000 rpm and 400 rpm/s 2nd stage: 30 s @ 4 000 rpm and 500 rpm/s
   - Hotplate: Soft bake. 10 min @ 60°C and 15 min @ 90°C
   - KS Aligner: 55 s expo @ ci2, hard contact. Mask: Chip mask v.2
   - Hotplate: PEB. 15 min @ 60°C and 20 min @ 90°C
   - Developer: PGMEA. 3 min, 1.5 rpm stirring. Rinse with Isopropanol

Wafer B

5. CLEAN WAFERS
   - Ultra sound: Triton X-100 for 20 min
   - Piranha: H_2SO_4 and H_2O_2 for 10 min @ 80 °C
   - 250 °C oven: over-night
6. Cr/Au MASK
   - Track 1: AZ 5214E resist, pr 1_5
   - KS Aligner: 6 s expo @ ci2, hard contact. Mask: Au mask for Pyrex
   - 120 ° hotplate: 80 s reverse bake
   - KS Aligner: 40 s flood-exposure
   - Developer: NaOH:H_2O (1:5). 70 s under stirring. Rinse in H_2O for 3 min
   - Plasma Asher: 240 sccm O_2, 40 sccm N_2, 400 W, 4 min
   - Alcatel: 100 Å Cr and 1 000 Å Au
   - Lift-off: Ultra sound in Acetone, 30 min. Rinse in H_2O for 3 min
7. BONDING LAYER
   - KS Spinner: SU-8 2005. 1st stage: 15 s @ 3 000 rpm and 400 rpm/s 2nd stage: 30 s @ 5 000 rpm and 600 rpm/s
   - Hotplate: Soft bake. 5 min @ 60°C and 10 min @ 90°C

Wafer C

8. RELEASE LAYER
   - ASE: Fluorocarbon deposition. 1 min 30 s, CF_4 = 120 sccm, p = 60 mTorr
9. LOWER CLADDING
   - KS Spinner: mr-L 6050 XP in syringe. Use gyrset for spinner, t = 3 s, p = 42 psi. 1st stage: 15 s @ 3 000 rpm and 400 rpm/s 2nd stage: 30 s @ 4 000 rpm and 500 rpm/s
   - Hotplate: Soft bake. 10 min @ 60°C and 15 min @ 90°C

Further process steps

10. 1st BOND
    - EVG-NIL Aligner: Align wafer A and B
    - EVG-NIL Bonder: 1 000 N, 90 °C, 30 min, cool down to room temperature
    - KS-Aligner: 30 s expo @ ci2, flood-exposure
    - Hotplate: PEB 10 min @ 60°C and 10 min @ 90°C
    - Scalpel: Separate wafers
    - Developer: PGMEA. 2 min in First and 2 min in Final, 1.5 rpm stirring. Rinse with Iso-propanol
11. 2nd BOND
    - EVG-NIL Bonder: Bond wafer B and C @ 100 N, 90 °C, 30 min, cool down to room temperature
    - KS Aligner: 55 s expo @ ci2, flood-exposure
    - Hotplate: PEB 15 min @ 60°C and 20 min @ 90°C
    - Scalpel: Separate wafers
    - Developer: PGMEA. 3 min, 1.5 rpm stirring. Rinse with Iso-propanol
12. RELEASE
    - Lift chips off Si wafer with tweezers

Appendix C

Gaussian mode profiles

The Gaussian wavefunction used to approximate the field distribution in the waveguides is expressed as

$$\phi(x) = \exp\left(-\frac{1}{2}\frac{(x-x_0)^2}{w_x^2}\right) \tag{C.1}$$

where x_0 is the position the function is centered at and w_x is the beam waist, figure 2.2.

The waveguides of this system are not symmetric but the width is different to the height. In some cases the refractive index step is also different. Therefore, the wavefunction is expressed as the product of two Gaussian functions with their respective beam waists.

$$\phi(X,Y) = \exp\left(-\frac{1}{2}\frac{X^2}{S_X^2}\right)\exp\left(-\frac{1}{2}\frac{Y^2}{S_Y^2}\right) \tag{C.2}$$

where X and Y are the normalised co-ordinates such that $X = x/\rho_x$ and $Y = y/\rho_y$ and S_X and S_Y are the normalised beam waists such that $S_X = w_x/\rho_x$ and $S_Y = w_y/\rho_y$, where ρ_x is the half width of the waveguide and ρ_y is the half height.

The normalised beam waists can be related to their respective V-parameter for each direction via two coupled transcendental equations

$$\frac{1}{S_X} = \frac{2V_x^2}{\sqrt{\pi}}\exp\left(-\frac{1}{S_X^2}\right)\mathrm{erf}\left(\frac{1}{S_Y}\right) \tag{C.3}$$

and

$$\frac{1}{S_Y} = \frac{2V_y^2}{\sqrt{\pi}}\exp\left(-\frac{1}{S_Y^2}\right)\mathrm{erf}\left(\frac{1}{S_X}\right) \tag{C.4}$$

where the V-parameter discussed in Chapter 2 is defined as

$$V_{x/y} = \frac{2\pi}{\lambda}\rho_{x/y}(n_{co}^2 - n_{cl}^2)^{1/2}$$

where λ is the wavelength, n_{co} and n_{cl} is the refractive index of the core and cladding materials respectively and $\rho_{x/y}$ is half the width/height of the waveguide structure.

Solving equation (C.3) and (C.4) with the expression for the V-parameter gives the values of the normalised beam waists for equation (C.2).

Before this equation can be applied for the mathematical calculations, the intensity distributions need to be normalised as

$$\int_{-\infty}^{\infty}\int_{-\infty}^{\infty} I(x,y) = 1 \tag{C.5}$$

where

$$I(x,y) = \phi^2(x,y)$$

giving

$$\psi(x,y) = \frac{\phi(x,y)}{\sqrt{\int_{-\infty}^{\infty}\int_{-\infty}^{\infty}\phi^2(x,y)\ dxdy}} \tag{C.6}$$

This is the definition of the normalised wavefunction used to calculate the size of the fundamental mode of the waveguides in Chapter 5.

Appendix D

Coupling efficiencies

Reflection mode

The coupling efficiency of the reflection mode, α_{ref} is found from computing the overlap integral of $\psi_2(x,y,l)$ & the cantilever front-end and $\psi_4(x,y,\ l,\ lb)$ & $\psi_1(x,y)$ at the cantilever/input waveguide interface

$$\alpha_{ref} = \alpha_{\psi_2/\mathrm{cant}} \times \alpha_{\psi_4/\psi_1}$$

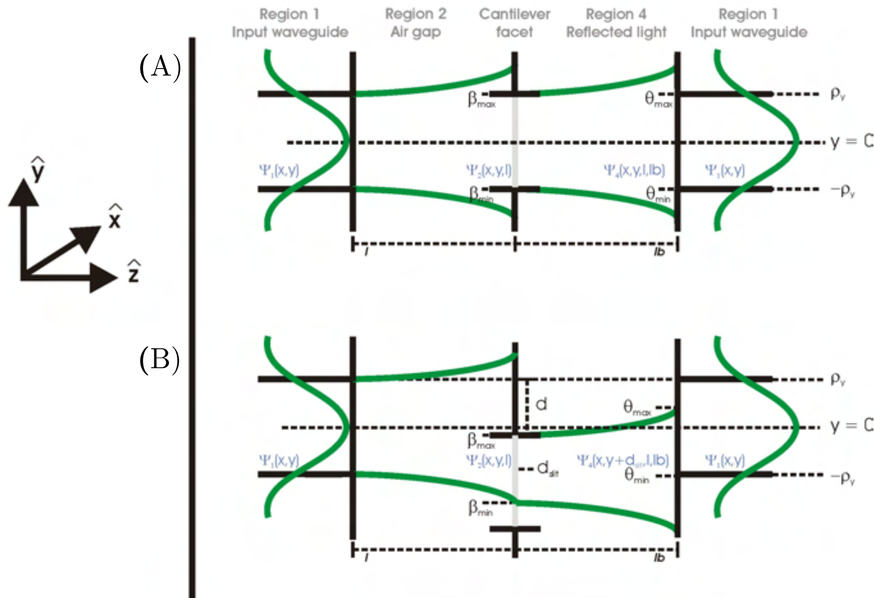

Figure D.1: In the reflection mode, the light travels across the air gap and reflects back into the input waveguide. Here, the cantilever is represented by a slit, letting light through. The different parameters used in the calculations are marked in the drawing.

Two integration limits, β_{min} and β_{max} are introduced at the cantilever front-end because this integral is either limited by the cantilever height or the zero position of the light intensity; $3 \times w_y 2(l)$. In fact, the intensity of the light *never* reaches zero but this limit is valid to use since it covers 99.76 % of the modal power.

$$\beta_{min} = \text{MAX}[\ -3 \times w_y 2(l);\ -\rho_y + d\ ]$$

$$\beta_{max} = \text{MIN}[\ 3 \times w_y 2(l);\ \rho_y + d\ ]$$

where $w_y 2(l)$ is the beam waist after a travelled distance (l), ρ_y is the half height of the cantilever and d is the cantilever deflection.

The back-reflected light is also modelled as a Gaussian wavefunction with its beam waist determined by the size of the illuminated slit. The position of the wavefunction is assumed as purely translative and directly related to the cantilever deflection. This is naturally not the true situation but it is a good approximation to use to be able to estimate the degree of coupling into the input waveguide of the back-reflected light. However, the assumption is only valid within the cantilever deflection range of ± 8.55 µm where the whole cantilever is illuminated. The break-down of the theory at larger cantilever deflections is caused by the effective diffraction of the light from the slit used to represent the cantilever. d_{slit} represents the center position of the back-reflected light and $w_y slit$ is the initial beam waist of the back-reflected light, i.e. w_0 when calculating the spread of the returning light. The two parameters are calculated as

$$d_{slit} = \frac{\beta_{max} + \beta_{min}}{2}$$

$$w_y slit = \frac{\beta_{max} - \beta_{min}}{2}$$

Furthermore, two new integration limits are introduced for the returning light at the input waveguide

$$\theta_{min} = \text{MAX}[-\rho_y;\ -3 \times w_y 4(l, lb) + d_{slit}]$$

$$\theta_{max} = \text{MIN}[\rho_y;\ 3 \times w_y 4(l, lb) + d_{slit}]$$

where l is the distance traveled *toward* the cantilever and lb is the distance traveld *backward*. For the situation where the light is coupled back into the input waveguide, $l = lb$.

These two integration limits serve the same purpose as β_{min} and β_{max}, to limit the integral either by the dimensions of the input waveguide or by the zero position of the light intensity distribution.

The full expression of α_{ref} can now be computed as

$$\alpha_{\psi_2/cant} = \frac{\int_{-\rho_x cant}^{\rho_x cant} \int_{\beta_{min}}^{\beta_{max}} \psi_2^2(x,y,l)\ dxdy}{\int_{-\infty}^{\infty} \int_{-\infty}^{\infty} \psi_1^2(x,y)\ dxdy} \tag{D.1}$$

where $\rho_x cant$ is the half width of the cantilever waveguide

and

$$\alpha_{\psi_4/\psi_1} = \frac{\int_{-\rho_x wgin}^{\rho_x wgin} \int_{\theta_{min}}^{\theta_{max}} \psi_4(x,y+d_{slit},l,lb)\psi_1(x,y)\ dxdy}{\int_{-\rho_x cant}^{\rho_x cant} \int_{\beta_{min}}^{\beta_{max}} \psi_2^2(x,y)\ dxdy} \tag{D.2}$$

where $\rho_x wgin$ is the half width of the input waveguide.

The numerator of (D.1) cancels with the denominator of (D.2) leaving

$$\alpha_{ref} = \frac{\int_{-\rho_x wgin}^{\rho_x wgin} \int_{\theta_{min}}^{\theta_{max}} \psi_4(x,y+d_{slit},l,lb)\psi_1(x,y)\ dxdy}{\int_{-\infty}^{\infty} \int_{-\infty}^{\infty} \psi_1^2(x,y)\ dxdy} \tag{D.3}$$

Transmission mode

The coupling efficiency of the transmission mode, α_{trans} is found from the overlap integrals of $\psi_2(x,y,l)$ & $\psi_3(x,y)$ at the air/cantilever interface and $\psi_3(x,y)$ & $\psi_5(x,y)$ at the cantilever/output waveguide interface

$$\alpha_{trans} = \alpha_{\psi_2/\psi_3} \times \alpha_{\psi_3/\psi_5}$$

In region 2, the mode develops according to equation (2.4) with an increasing beam waist across the gap. The overlap integral at the air/cantilever interface can be computed over infinity as the $\psi_3(x,y)$ mode is strictly confined inside the cantilever with zero intensity field outside, figure 5.3 and 5.4. However, it shall be noted that this integration is only valid within a cantilever deflection of ± 8.55 µm which is the maximum displacement for the cantilever to remain fully illuminated assuming the intensity of the light reaches zero at $3 \times w_y 2(l = 10\ \mu\text{m})$.

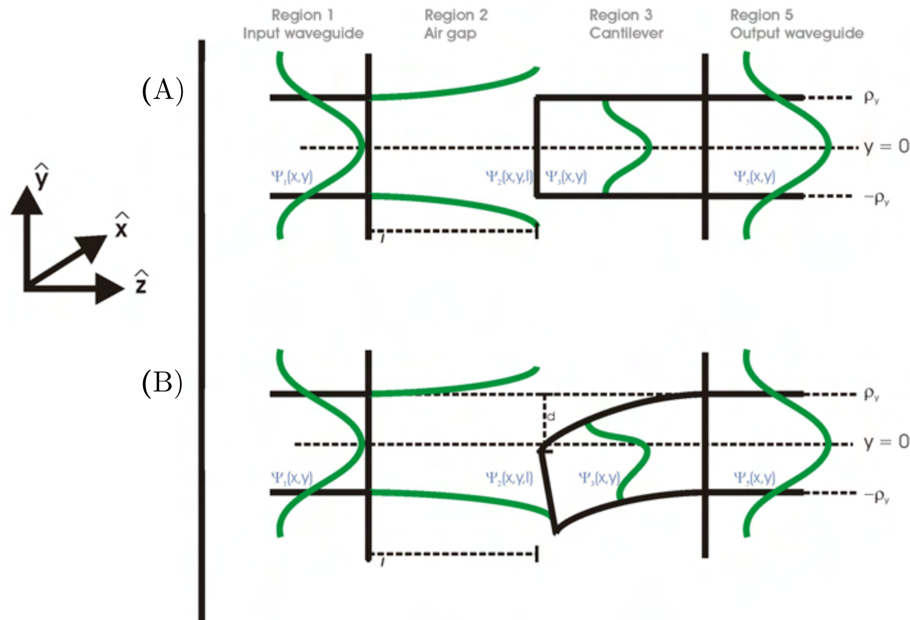

Figure D.2: Schematic drawing of the light path in the transmission mode. The light travels across the air gap, continues into the cantilever and exits the system on the opposite side. When the cantilever deflects less light is coupled into the cantilever.

In region 3 the light is assumed to follow the cantilever perfectly, even when the cantilever is bent. This means that no losses are introduced and that the intensity distribution is not altered but simply translated in the vertical direction. In mathematical terms it can be expressed as

$$\int_{-\rho_x cant}^{\rho_x cant} \int_{-\infty}^{\infty} \psi_3(x, y + d)\ dy = \int_{\rho_x cant}^{\rho_x cant} \int_{-\rho_y}^{\rho_y} \psi_3(x, y)\ dy$$

where $\rho_x cant$ and ρ_y are the half width and half height of the cantilever respectively and d is the cantilever displacement.

This assumption is valid since even a displacement of 5 μm of the 200 μm long cantilever results in a radius of curvature of $\sim$ 4 mm. This is far above the threshold value for introduction of significant bending losses, especially with the large index step between the SU-8 core and the surrounding air.

Now, the two parts of α_{trans} are expressed as

$$\alpha_{\psi_2/\psi_3} = \frac{\int_{-\infty}^{\infty} \int_{-\infty}^{\infty} \psi_2(x, y, l)\psi_3(x, y + d)\ dxdy}{\int_{-\infty}^{\infty} \int_{-\infty}^{\infty} \psi_1^2(x, y)\ dxdy} \tag{D.4}$$

and

$$\alpha_{\psi_3/\psi_5} = \frac{\int_{-\rho_x wgout}^{\rho_x wgout} \int_{-\rho_y}^{\rho_y} \psi_3(x, y)\psi_5(x, y)\ dxdy}{\int_{-\rho_x cant}^{\rho_x cant} \int_{-\infty}^{\infty} \psi_3^2(x, y + d)\ dxdy} \tag{D.5}$$

where $\rho_x wgout$ and $\rho_x cant$ are the half width of the output waveguide and the cantilever respectively.

The denominator of (D.5) can be replaced from the definition above to read

$$\alpha_{\psi_3/\psi_5} = \frac{\int_{-\rho_x wgout}^{\rho_x wgout} \int_{-\rho_y}^{\rho_y} \psi_3(x, y)\psi_5(x, y)\ dxdy}{\int_{-\rho_x cant}^{\rho_x cant} \int_{-\rho_y}^{\rho_y} \psi_3^2(x, y)\ dxdy} \tag{D.6}$$

Finally, the whole expression of α_{trans} is

$$\alpha_{trans} = \frac{\int_{-\infty}^{\infty} \int_{-\infty}^{\infty} \psi_2(x, y, l)\psi_3(x, y + d)\ dxdy}{\int_{-\infty}^{\infty} \int_{-\infty}^{\infty} \psi_1^2(x, y)\ dxdy} \times \\ \times \frac{\int_{-\rho_x wgout}^{\rho_x wgout} \int_{-\rho_y}^{\rho_y} \psi_3(x, y)\psi_5(x, y)\ dxdy}{\int_{-\rho_x cant}^{\rho_x cant} \int_{-\rho_y}^{\rho_y} \psi_3^2(x, y)\ dxdy} \tag{D.7}$$

Appendix E

Cantilever processing

1. RELEASE LAYER
   - ASE: Fluorocarbon deposition. 1 min 30 s, CF_4 = 120 sccm, p = 60 mTorr
2. CANTILEVER LAYER
   - KS Spinner: SU-8 2005. 1st stage: 15 s @ 3 000 rpm and 400 rpm/s 2nd stage: 30 s @ 5 000 rpm and 600 rpm/s
   - Hotplate: Soft bake. 5 min @ 60°C and 10 min @ 90°C
   - KS Aligner: 30 s expo @ ci2, hard contact. Mask: Cantilever structures
   - Hotplate: PEB. 10 min @ 60°C and 10 min @ 90°C
   - Developer: PGMEA. 2 min in First and 2 min in Final, 1.5 rpm stirring. Rinse with Iso-propanol
3. SUPPORT LAYER
   - KS Spinner: SU-8 2075 in syringe. Use gyrset for spinner, t = 3 s, p = 42 psi. 1st stage: 15 s @ 500 rpm and 100 rpm/s 2nd stage: 30 s @ 1 000 rpm and 200 rpm/s
   - Hotplate: Soft bake. 15 min @ 60°C and 30 min @ 90°C
   - KS Spinner: SU-8 2075 in syringe. Use gyrset for spinner, t = 3 s, p = 42 psi. 1st stage: 15 s @ 500 rpm and 100 rpm/s 2nd stage: 30 s @ 1 000 rpm and 200 rpm/s
   - Hotplate: Soft bake. 15 min @ 60°C and 30 min @ 90°C
   - KS Aligner: 300 s expo @ ci2, soft contact. Multiple exposure: 6 × 50 s with 40 s intervals. Mask: Cantilever chips
   - Hotplate: PEB. 20 min @ 60°C and 45 min @ 90°C

- Developer: PGMEA. 20 min in First and 5 min in Final. Rinse with Iso-propanol

4. RELEASE

- Lift chips off Si wafer with tweezers

Appendix F

List of publications

Articles in Reviewed Journals

1. M. Nordström, M. Calleja, J. Hübner, A. Boisen. Novel fabrication technique for free-hanging homogeneous polymeric cantilever waveguides, *Accepted for publication in Journal of Micromechanics and Microengineering*

2. M. Nordström, M. Calleja, J. Hübner, A. Boisen. Integrated optical readout for miniaturisation of cantilever-based sensor systems, *Applied Physics Letters* **91** (2007) 103512

3. M. Nordström, D.A. Zauner, A. Boisen, J. Hübner. Single-mode waveguides with SU-8 polymer core and cladding for MOEMS applications, *Journal of Lightwave Technology* **25** (2007) 1284-1289

4. M. Nordström, J. Hübner, A. Boisen. Sloped side walls in SU-8 structures with 'Step-and-Flash' processing, *Microelectronic Engineering* **83** (2006) 1269-1272

5. M. Calleja, J. Tamayo, M. Nordström, A. Boisen. Low noise polymeric nanomechanical biosensor, *Applied Physics Letters* **88** (2006) 113901

6. R. Marie, S. Schmid, A. Johansson, L. Ejsing, M. Nordström, D. Haefliger, C.B.V. Christensen, A. Boisen, M. Dufva. Immobilisation of DNA to polymerized SU-8, *Biosensors & Bioelectronics* **21** (2006) 1327-1332

7. M. Nordström, A. Johansson, E. Sánchez-Noguerón, B. Clausen, M. Calleja, A. Boisen. Investigation of the bond strength between the photo-sensitive polymer SU-8 and Au, *Microelectronic Engineering* **78-79** (2005) 152-157

8. D. Haefliger, M. Nordström, P.A. Rasmussen, A. Boisen. Dry release of all-polymer structures, *Microelectronic Engineering* **78-79** (2005) 88-92

9. M. Nordström, M. Calleja, A. Boisen. Polymeric micro-channel-based functionalisation system for micro-cantilevers, *Ultramicroscopy* **105** (2005) 281-286

10. M. Calleja, M. Nordström, M. Álvarez, J. Tamayo, L.M. Lechuga, A. Boisen. Highly sensitive polymer-based cantilever-sensors for DNA detection, *Ultramicroscopy* **105** (2005) 215-222

11. M. Nordström, R. Marie, M. Calleja, A. Boisen. Rendering SU-8 hydrophilic to facilitate use in micro channel fabrication, *Journal of Micromechanics and Microengineering* **14** (2004) 1614-1617

International Conference Proceedings

1. M. Nordstrm̈, D.A. Zauner, M. Calleja, J. Hübner, A. Boisen. Cantilever-based sensor with integrated optical read-out using single-mode waveguides, *11th International Conference on Miniaturised Systems for Chemistry and Life Sciences (μTAS 2007)*, Paris, France, October 7-11 2007, pp. 497-499

2. M. Nordstrm̈, D.A. Zauner, M. Calleja, J. Hübner, A. Boisen. Integrated optical read-out for polymeric micro cantilevers, *2nd International workshop on Nanomechanical sensors*, Montral, Canada, May 27-30 2007 (*oral*)

3. M. Nordström, J. Hübner, A. Boisen. Novel fabrication technique for free-hanging polymeric structures, *32nd International Conference on Micro and Nano Engineering (MNE 2006)*, Barcelona, Spain, September 17-20 2006, pp. 373-374

4. M. Nordström, M. Calleja, A. Boisen. Characterisation of SU-8 as a platform for cantilever sensors, *1st International Workshop on Nanomechanical Sensors*, Copenhagen, Denmark, May 8-12 2006, pp. 76-77

5. M. Calleja, M. Nordström, A. Boisen, J. Tamayo. Low-noise polymeric nanomechanical biosensors, *1st International Workshop on Nanomechanical Sensors*, Copenhagen, Denmark, May 8-12 2006, pp. 29-30 (*oral*)

6. K. Sidler, M. Nordström, A. Boisen. Fabrication and characterisation of AFM probes in SU-8 using a dry release method, *2nd International Workshop on Nanomechanical Sensors*, Copenhagen, Denmark, May 8-12 2006, pp. 50-51

7. M. Nordström, D.A. Zauner, A. Boisen, J. Hübner. Monolithic single-mode SU-8 waveguides for integrated optics, *Proceedings of SPIE, Vol. 611; Microfluidics, BioMEMS and Medical Microsystems IV*, San José, CA, USA, January 23-25 2006, pp. 43-45 (*oral*)

8. M. Nordström, J. Hübner, A. Boisen. Sloped side walls in SU-8 structures with 'Step-and-Flash', *31st International Conference on Micro and Nano Engineering (MNE 2005)*, Vienna, Austria, September 19-22 2005 (*oral*)

9. M. Calleja, M. Nordström, D. Haefliger, A. Boisen, L.M. Lechuga, J. Tamayo. Direct real-time immunodetection of the human growth hormone with polymeric nanomechanical sensors, *Eurosensors XIX*, Barcelona, Spain, September 11-14 2005 (*oral*)

10. M. Calleja, M. Nordström, M. Álvarez, L.M. Lechuga, A. Boisen, J. Tamayo. Highly sensitive polymer-based cantilever sensors for DNA detection, *Material Research Society Spring Meeting 2005*, San Francisco, CA, USA, March 29-31 2005, pp. 680 (*oral*)

11. M. Nordström, M. Calleja, A. Boisen. Polymeric micro cantilevers with complementary micro channel system as analysis set-up, *1st Workshop on Nanomechanical Sensors*, Madrid, Spain, November 15-16 2004, pp. 18 (*oral*)

12. D. Haefliger, M. Nordström, P.A. Rasmussen, A. Boisen. Novel fabrication techniques for polymeric nanomechanical sensors, *1st Workshop on Nanomechanical Sensors*, Madrid, Spain, November 15-16 2004, pp. 29 (*oral*)

13. M. Calleja, M. Nordström, M. Álvarez, A. Boisen, J. Tamayo. Highly sensitive polymer-based cantilever-sensors for DNA detection, *1st Workshop on Nanomechanical Sensors*, Madrid, Spain, November 15-16 2004, pp. 36

14. M. Calleja, M. Álvarez, M. Nordström, A. Boisen, L.M. Lechuga, J. Tamayo. Polymeric cantilever arrays for biosensing applications, *Ibersensors IV*, Puebla, Mexico, October 27-29 2004, pp. 109

15. M. Nordström, M. Calleja, A. Boisen. Polymeric micro channel system for easy sensitisation of micro cantilevers, *8th International Conference on Miniaturised Systems for Chemistry and Life Sciences (µTAS 2004)*, Malmö, Sweden, September 26-30 2004, pp. 55-57

16. M. Nordström, R. Marie, M. Calleja, A. Boisen. A wet chemical treatment for specific change of the contact angle of SU-8, *8th International Conference on Miniaturised Systems for Chemistry and Life Sciences (µTAS 2004)*, Malmö, Sweden, September 26-30 2004, pp. 91-93

17. M. Nordström, A. Johansson, E. Sánchez-Noguerón, B. Clausen, M. Calleja, A. Boisen. Investigation of the bond strength between the photo-sensitive polymer SU-8 and Au, *30th International Conference on Micro and Nano Engineering (MNE 2004)*, Rotterdam, The Netherlands, September 19-22 2004, pp. 214-215

18. D. Haefliger, M. Nordström, P.A. Ramussen, A. Boisen. Dry release of all-polymer structures, *30th International Conference on Micro and Nano Engineering (MNE 2004)*, Rotterdam, The Netherlands, September 19-22 2004, pp. 88-89 (*oral*)

19. M. Nordström, M. Calleja, A. Boisen. Polymeric micro cantilevers with complementary micro channel system for biochemical analysis, *6th International Conference on Scanning Probe Microscopy, Sensors and Nanostructures (SPM 2004)*, Beijing, China, May 23-27 2004, pp. 141

20. M. Álvarez, M. Calleja, J.A. Plaza, K. Zinoviev, M. Nordström, A. Boisen, C. Dominguew, L.M. Lechuga, J. Tamayo. Fabrication and characterisation of high sensitive microcantilever for biosensor application, *6th International Conference on Scanning Probe Microscopy, Sensors and Nanostructures (SPM 2004)*, Beijing, China, May 23-27 2004, pp. 315

21. M. Calleja, J. Tamayo, M. Nordström, A. Johansson, P.A. Rasmussen, L.M. Lechuga, A. Boisen. Polymeric cantilever arrays for biosensing applications, *Materials Reseach Society Spring Meeting*, San Francisco, CA, USA,
April 12-16 2004, pp. 450 (*oral*)

National Conference Proceedings

1. D. Haefliger, M. Nordström, A. Johansson, P.A. Rasmussen, A. Boisen. Polymeric microchip technology, *BioTech Forum Science Conference - interdisciplinary and cross border world-class research*, Copenhagen, Denmark, October 5-7 2004

2. D. Haefliger, M. Nordström, B.P. Cahill, A. Stemmer, A. Boisen. Simple tools for plastic microdevice fabrication, *Danish Physical Society Annual Meeting*, Nyborg, Denmark, May 27-28 2004 (*oral*)

3. M. Nordström, M. Calleja, A. Boisen. Polymeric micro channel system as a complement to micro cantilevers, *Danish Physical Society Annual Meeting*, Nyborg, Denmark, May 27-28 2004 (*oral*)

Patent Applications

1. M. Nordström, A. Boisen, J. Hübner. Integrated optical readout for cantilever sensors, European Patent Application 40173 EP 01 (2006)

2. M. Nordström, M. Calleja, A. Boisen. Microfluidic sample delivery system, PCT Patent Application WO 2005-099901-A1 (2005)

3. M. Nordström, M. Calleja, A. Boisen. Polymer-based cantilever array with optical read-out, US Patent Application US 2006/0075803 A1 (2004)